

# Hybrid Electromagnetic Models for the Purpose of Detection and Identification of Visually Obscured Targets

by

**Mojtaba Dehmollaian**

A dissertation submitted in partial fulfillment  
of the requirements for the degree of  
Doctorate of Philosophy  
(Electrical Engineering)  
in The University of Michigan  
2007

Doctoral Committee:

Professor Kamal Sarabandi, Chair  
Professor Jeffrey A. Fessler  
Professor Eric Michielssen  
Professor Fawwaz T. Ulaby

To my parents.

## ACKNOWLEDGEMENTS

I would like to express my deep appreciation to my past teachers and mentors who helped me along this long journey without whom creation of this dissertation could not have been possible.

I would like to sincerely thank professor Kamal Sarabandi for his many supports. He gave me the opportunity to continue my graduate study at the Radiation Laboratory and continuously supported and encouraged me during the course of research. His excellence in teaching had a great impact on my progress in research. I would like to deeply thank my dissertation committee members professor Jeffrey A. Fessler, professor Eric Michielssen, and professor Fawwaz T. Ulaby who honored me by accepting to serve in my dissertation committee.

I would like to greatly appreciate all members of the Radiation Laboratory faculty. Especially, I would like to thank Dr. Hossein Mosallaei for his true helps and supports. He provided significant support in the development of the second chapter of this thesis. He left the University of Michigan to accept a teaching position at Northeastern University. Also, many thanks goes to Dr. Adib Nashashibi for his great help and invaluable advice related to my experimental work. My sincere appreciation is given to Dr. Leland Pierce for his many helps in solving my computer programming problems.

I would like to thank all the staff members of the Radiation Laboratory especially Mrs. Susan Charnley who kindly accepted to review and edit many chapters of the thesis even after she left the Radiation Laboratory to work for the department of Mechanical Engineering.

I would like to sincerely thank all of my colleagues and friends at the Radiation Laboratory for their invaluable friendship and helpful conversations. Especially, I would like to thank Mr. Alireza Tabatabaenejad and Dr. Reza Azadegan for their friendship and

comradery.

I would like to thank my parents for their sacrifices they have made for my progress in education. Without their constant love this could not have been possible.

# TABLE OF CONTENTS

<b>DEDICATION</b>		ii
<b>ACKNOWLEDGEMENTS</b>		iii
<b>LIST OF FIGURES</b>		viii
<b>LIST OF TABLES</b>		xiv
<b>CHAPTERS</b>		
1	Introduction	1
1.1	Background	1
1.2	Motivation and Objectives	4
1.2.1	Electromagnetic Scattering from Foliage Camouflaged Targets	5
1.2.2	Through-Wall Imaging: Forward and Inverse Model	8
1.3	Dissertation overview	10
2	Hybrid FDTD and Single Scattering Theory for Simulation of Scattering from Hard Targets Camouflaged under Forest Canopy	12
2.1	Introduction	13
2.2	Theory	15
2.2.1	Coherent Forest Model	15
2.2.2	Computation of Local Scattered Field Using FDTD	19
2.2.3	Computation of Backscattered Field	19
2.3	Numerical Simulations of Foliage Camouflaged Targets	27
2.4	Conclusions	29
3	Electromagnetic Scattering from Foliage Camouflaged Complex Targets	35
3.1	Introduction	36
3.2	Electromagnetic Scattering from Foliage	38
3.3	Computation of Induced Surface Current	40
3.3.1	Model Validation	50
3.4	Computation of Hard Target-Foliage Interaction	53
3.5	Simulation of Hard Targets Embedded in Foliage	55
3.6	Conclusion	62

4	Analysis of Optimum Polarization for Discrimination of Foliage Camouflaged Hard Targets Using Genetic Algorithms . . . . .	63
4.1	Introduction . . . . .	63
4.2	Theory . . . . .	65
4.2.1	Problem Formulation . . . . .	67
4.2.2	Genetic Algorithm Realization . . . . .	70
4.3	Simulation Results . . . . .	71
4.4	Conclusion . . . . .	73
5	Refocusing through Building Walls, Using Synthetic Aperture Radar . . . . .	77
5.1	Introduction . . . . .	78
5.2	Numerical Simulations . . . . .	80
5.2.1	Image Construction . . . . .	80
5.2.2	Refocusing approach and sensitivity analysis . . . . .	84
5.2.3	Application of refocusing method in practice . . . . .	87
5.3	Experimental Study . . . . .	88
5.3.1	Calibration . . . . .	89
5.3.2	Measurement of the relative dielectric constant of the concrete wall . . . . .	90
5.3.3	Refocusing . . . . .	92
5.3.4	Discussion on the modeling and future application of the refocusing method . . . . .	99
5.4	Conclusions . . . . .	99
6	Hybrid FDTD and Ray-Optics Approximation for Simulation of Through-Wall Microwave Imaging . . . . .	103
6.1	Introduction . . . . .	103
6.2	Theoretical Model . . . . .	104
6.3	Simulation Results . . . . .	107
6.4	Experimental Results . . . . .	108
7	An Approximate Solution of Scattering from Reinforced Concrete Walls Using An Analytic 1-D Periodic Green's Function . . . . .	110
7.1	Introduction . . . . .	111
7.2	Formulation . . . . .	113
7.2.1	Computation of induced currents on metallic rods . . . . .	115
7.2.2	1-D periodic Green's function for the case where sources are inside a dielectric slab . . . . .	116
7.2.3	Computation of incident fields inside the dielectric slab . . . . .	118
7.2.4	Computation of transmission and reflection coefficients . . . . .	119
7.3	Scattering from crossed rebar walls . . . . .	120
7.4	Numerical Simulations . . . . .	124
7.5	Conclusions . . . . .	127
8	Conclusions and Recommendations for Future Work . . . . .	133

8.1	Summary . . . . .	133
8.2	Contributions . . . . .	134
8.2.1	Development of a comprehensive physics-based model for computation of scattering from complex targets camouflaged inside forest canopies . . . . .	134
8.2.2	Polarization Discrimination for Improving Foliage-Camouflaged Target Detection . . . . .	135
8.2.3	Phenomenological Study of Through-Wall Imaging, Forward and Inverse Models . . . . .	135
8.2.4	Development of An Approximate Solution of Scattering from Reinforced Concrete Walls Using An Analytic 1-D Periodic Green's Function . . . . .	136
8.3	Future Work . . . . .	137
8.3.1	Future researches on the EM scattering from foliage camouflaged targets . . . . .	137
8.3.2	Future researches on the through-wall imaging . . . . .	138
<b>APPENDIX . . . . .</b>		<b>140</b>
<b>BIBLIOGRAPHY . . . . .</b>		<b>143</b>

## LIST OF FIGURES

<b>Figure</b>		
2.1	Extinction profile of pine tree stand with density of $0.05 \text{ trees}/m^2$ for incidence elevation angle of $30^\circ$ . . . . .	18
2.2	Geometry of the problem. Surface $\mathbf{S}$ is containing an object above the ground plane. . . . .	22
2.3	Comparison of backscattering RCS from a dihedral corner reflector in free space, calculated by direct FDTD, hybrid method, and physical optics + PTD approximation for an H-polarized incident plane wave propagating along $\theta_i = 30^\circ$ and $\phi_i = 180^\circ$ . (a) Frequency domain. (b) Time domain. . . . .	26
2.4	(a) Geometry of the scattering problem when the effect of ground plane exists. (b) Comparison of backscattering RCS from a dihedral corner reflector, above a dielectric ground plane with $\epsilon_r = 5.62 + i 0.94$ , calculated by the hybrid method, and physical optics + PTD approximation for an H-polarized incident plane wave propagating along $\theta_i = 30^\circ$ and $\phi_i = 180^\circ$ . . . . .	27
2.5	Comparison of backscattering RCS from a dihedral corner reflector (each panel is $3m \times 3m$ ), placed 0.5 m above a dielectric ground plane with $\epsilon_r = 5.62 + i 0.94$ , calculated by the hybrid method, inside and outside of the forest for standard polarization configurations of incident plane wave propagating along $\theta_i = 30^\circ$ and $\phi_i = 180^\circ$ . (a) $\sigma_{hh}/\lambda^2$ (b) $\text{Angle}(S_{hh})$ (c) $\sigma_{vv}/\lambda^2$ (d) $\text{Angle}(S_{vv})$ . . . . .	31
2.6	(a) FDTD model of the hard target with fine resolution mesh ( resolution $\approx 1 \text{ cm}$ ), (b) course FDTD mesh (resolution = 10 cm), used for VHF simulation, and (c) the FDTD box located inside a forest, including eight pine trees. . . . .	32
2.7	Comparison of backscattering RCS from the metallic vehicle, above a dielectric ground plane with $\epsilon_r = 5.62 + i 0.94$ , calculated by the hybrid method, inside and outside of the forest for standard polarization configurations of incident plane wave propagating along $\theta_i = 30^\circ$ and $\phi_i = 180^\circ$ . (a) $\sigma_{hh}/\lambda^2$ (b) $\text{Angle}(S_{hh})$ (c) $\sigma_{vv}/\lambda^2$ (d) $\text{Angle}(S_{vv})$ (e) $\sigma_{hv}/\lambda^2$ (f) $\text{Angle}(S_{hv})$ . . . . .	33
2.8	Comparison of backscattering RCS from a target, target and forest, and forest alone, for horizontal and vertical polarizations of incident waves propagating along $\theta_i = 30^\circ$ and $\phi_i = 180^\circ$ . (a) Dihedral $\sigma_{hh}/\lambda^2$ (b) Dihedral $\sigma_{vv}/\lambda^2$ (c) Vehicle $\sigma_{hh}/\lambda^2$ (d) Vehicle $\sigma_{vv}/\lambda^2$ . . . . .	34

3.1	Comparison between CDF of the simulated and measured one-way foliage attenuation for (a) horizontal and (b) vertical polarizations. . . . .	40
3.2	Geometry of a smooth convex object and shadowed areas for direct and reflected waves for two different heights of the object above the ground plane. .	41
3.3	(a) Geometry of a simple metallic target. (b) Comparison of backscattering RCS calculated by exact EFIE method, the proposed hybrid GOPOPO method, and a first-order PO approximation (GOPO) for an H-polarized incident plane wave. . . . .	47
3.4	(a) Structure and approximate dimensions of a simplified tank, used for simulation at $f = 2 \text{ GHz}$ . (b) The electric current distribution over the hull of the tank with the turret removed and (c) the current distribution over the entire structure for an H-polarized incident wave in the direction of $\theta_i = 30^\circ$ and $\phi_i = 180^\circ$ . . . . .	49
3.5	(a) A scaled model for a surrogate tank, used for backscatter measurements, over the frequency range of 93 – 94 GHz. (b) Styrofoam target mount over a turntable for backscatter measurement. Here $\hat{n}$ is the normal to the plate and $\delta\theta$ and $\delta\phi$ denote target orientation errors. . . . .	51
3.6	(a) Comparison of the backscattering RCS values between the measured and simulation results for (a) a rectangular PEC plate ( $20.3 \text{ cm} \times 9.5 \text{ cm}$ ) and (b) the scaled tank, at $\phi_i = 180^\circ$ and different elevation incident angles of $\theta_i$ , and for vertically polarized incident field. . . . .	52
3.7	Calculated RCS of a $3\lambda \times 3\lambda$ metallic plate, over a lossy half space embedded inside a pine forest canopy as a function of elevation and azimuth angles (a) $\sigma_{hh}$ and (c) $\sigma_{vv}$ at $2 \text{ GHz}$ . Also shown the backscatter from the plate with and without foliage at $\phi_i = 180^\circ$ and for different elevation angles. <b>I</b> -bar on the mean value shows the fluctuation range of the backscattering cross section for 10 Monte Carlo simulations, (b) $\sigma_{hh}$ and (d) $\sigma_{vv}$ . . . . .	58
3.8	Calculated backscattering coefficient of the pine stand as a function of elevation and azimuth angles of $\theta_i$ and $\phi_i$ . (a) $\sigma_{hh}^o$ and (c) $\sigma_{vv}^o$ . Also shown the backscattering coefficient at $\phi_i = 180^\circ$ and for different elevation angles. <b>I</b> -bar on the mean value shows the fluctuation range of the backscattering coefficient for 10 Monte Carlo simulations. (b) $\sigma_{hh}^o$ and (d) $\sigma_{vv}^o$ . . . . .	59
3.9	Backscattered RCS of the metallic structure shown in Fig. 3.3, with dimensions of $AB = 8\lambda$ , $BC = 4\lambda$ , $CD = GH = 2.5\lambda$ and $DE = EF = 3\lambda$ , and a length of $5\lambda$ along the $\hat{y}$ direction, placed above a lossy dielectric ground at frequency of 2 GHz, as a function of the incident angle $\theta_i$ , for $\phi_i = 180^\circ$ , inside and outside the forest. The density of pine trees is $0.05 \text{ trees}/\text{m}^2$ . (a) $\sigma_{hh}$ and (b) $\sigma_{vv}$ . Direct backscatter from the forest is not shown in these figures.	60
3.10	Backscatter RCS of the metallic tank shown in Fig.3.4(a) at frequency of 2 GHz, as a function of the incident angle $\theta_i$ , for $\phi_i = 180^\circ$ with and without the effect of forest. (a) $\sigma_{hh}$ and (b) $\sigma_{vv}$ . . . . .	61

4.1	The metallic object used as a target embedded inside the forest. Frequency of operation is 2 GHz. For TE polarization of incident field, $\phi = 180^\circ$ , and different elevation angles $\theta$ the backscattered RCS from such an object is reported in [76]. . . . .	66
4.2	Polarization angles (a) $\psi$ and (b) $\chi$ for transmit and receive waves, obtained by different seeds, in optimization of $Max\{N[\frac{\sigma_t}{\sigma_c} > L]\}$ , performed for L = -8dB. . . . .	74
4.3	(a) Solution regions for tilt angle of transmit and receive polarizations. (b) Structure of a typical pine stand generated in simulation. . . . .	74
4.4	The convergence performance of GA in optimization of (4.10) for (a) L = -13 dB, (b) -8 dB and (c) -3 dB. Histogram of signal-to-clutter ratio, using 100 realizations of forest around the hard target for (d) L = -13 dB, (e) -8 dB and (f) -3 dB. . . . .	75
4.5	Normalized co-polarized backscatter polarization response of the target embedded in foliage and the clutter for an incident plane wave propagating along $\theta_i = 35^\circ$ , and $\phi_i = 180^\circ$ , using average covariance matrix of 100 realizations. co-polarization of (a) the target in presence of the foliage and (b) the clutter alone. . . . .	76
4.6	Optimum polarization angles of transmit and receive waves, obtained by different seeds, in optimization of $Max\{\frac{\langle\sigma_t\rangle}{\langle\sigma_c\rangle}\}$ (a) $\psi$ and (b) $\chi$ . . . . .	76
5.1	Target imaging/detection by using a moving transceiver antenna . . . . .	81
5.2	Images of the point target behind the brick wall, (a) standard SAR image and (b) refocused image with full compensation, $C = T^{-2}$ . . . . .	84
5.3	(a) Point spread functions along the range and (b) along the cross-range. Solid line (-) is for the target image when there is no wall, dashed line(- -) is for the target image behind the wall when $C = T^{-2}$ , dash-dotted line (-·-) is for that when $C = e^{-2i\angle T}$ , and dotted line (· ·) is for the target image behind the wall when no compensation is performed, $C = 1$ . . . . .	85
5.4	Squared errors of the point target image. The images are compensated for (a) the magnitude and phase ( $C = T^{-2}$ ) and (b) only phase ( $C = e^{-2i\angle T}$ ) of the transmissivity. The SE's are provided as functions of real parts of permittivity $\epsilon'_{rp}$ , assuming the imaginary part is 0.3 and for different wall thicknesses $d_p$ . . . . .	86
5.5	Squared error of the point target image as a function of $\epsilon'_{rp}$ and target position $x_s$ computed for wall thickness of 30 cm. The target image is compensated for the phase of transmissivity ( $C = e^{-2i\angle T}$ ). . . . .	88
5.6	(a) Side view and (b) schematic of the measurement setup. . . . .	89
5.7	(a) The relative dielectric constant of concrete blocks as a function of frequency and (b) transmissivity through the concrete wall at normal incident angle. . . . .	90
5.8	(a) The trihedral corner reflector, used as a target behind the wall and (b) its normalized image using the standard SAR imaging. . . . .	93
5.9	(a) The normalized image of the trihedral when there is no wall and (b) the normalized SAR image of the trihedral behind the wall, when the image is compensated for the effect of the wall. . . . .	93

5.10	(a) Cuts of target images along the range and (b) along the cross-range. Solid line (-) is for the target image when there is no wall, dashed line (- -) is for the target behind the wall when the pattern is compensated, and the dotted line (··) is for the target behind the wall, imaged by standard SAR imaging.	94
5.11	Squared error of the trihedral image using the experimental data. The $SE$ 's are provided as functions of real part of permittivity $\epsilon'_{rp}$ assuming a fixed imaginary part of 0.7 and for different wall thickness values ( $d_p$ ). The image of the trihedral is compensated for the phase of the transmissivity (i.e. $C = e^{-2i\angle T}$ ).	94
5.12	(a) The experimental image of the trihedral behind wall, using total received signal. (b) Compensated image using $C = e^{-2i\angle T}$ . (c) First total received signal is subtracted from analytically computed reflected fields. Next compensated image using $C = e^{-2i\angle T}$ is calculated.	96
5.13	(a) Two corner reflectors behind the wall and (b) their normalized image using the standard SAR imaging.	100
5.14	(a) Two trihedral corner reflectors when there is no wall in place, and their images when the wall is built: (b) compensated image using both magnitude and phase, and (c) compensated image employing only the phase of transmissivity.	101
5.15	(a) Cuts of images along the range and (b) along the cross-range. Solid line (-) is for the two trihedrals image when there is no wall, dashed line (- -) is for the targets behind the wall when the pattern is compensated by $C = T^{-2}$ , and the dotted line (··) is for the targets behind the wall, computed by standard SAR imaging.	102
5.16	(a) Image of two trihedral corner reflectors. Multiplication of two images: one is performed over frequency band of 1-3 GHz, and the other computed for frequency band of 2.95-3 GHz. (b) An image is performed using the entire frequency band (1-3 GHz) and multiplied by itself. The cuts along the cross-range of this image and that of the figure (a) at the range of -0.705 m are compared. All the images are compensated by $C = T^{-2}$ .	102
6.1	Emanating fields from transmitter antenna is considered as a set of rays incident to the wall. One ray is considered for each composing block, assuming the incident field is locally plane wave for that block. (a) top view (b) side view.	105
6.2	Comparison of (a) total propagated field through a solid wall between GO and proposed PO method using analytical formulations, and (b) scattered field from a solid wall using proposed PO method with FDTD and with analytical formulations.	106
6.3	(a) Each composing block is considered as a quarter of an actual cinder block. (b) Image of a point target located at $x = -3$ m behind a cinder block wall.	108
6.4	A cinder block.	109
6.5	(a) Image of the sphere behind the cinder block wall. (b) Image of the sphere compensated for the phase of measured transmissivity.	109
7.1	(a) Geometry of a vertical rebar concrete wall. (b) Cross section of a metallic rod.	115

7.2	Geometry of a crossed-rebar concrete wall. . . . .	122
7.3	Relative average powers of Bragg modes, scattered from the crossed rebar concrete wall, due to a TE polarized incident field at oblique ( $\theta=150$ , $\phi=30$ ) and normal incident angles, computed with an FDTD numerical method for different metal thicknesses. (a) Relative average power carried by all Bragg modes except zeroth order mode (i.e. $\langle P_t - P_{00} \rangle / \langle P_t \rangle$ ) and (b) relative average power carried by modes for which $n \neq 0$ and $m \neq 0$ (i.e. $\langle \sum_{n \neq 0} \sum_{m \neq 0} P_{nm} \rangle / \langle P_t \rangle$ ). . . . .	122
7.4	(a) Magnitude of co-polarized reflection coefficients, and (b) transmission coefficients of a vertical rebar in free space at normal incidence ( metal thickness = 1.2 cm). Polarization of incident field is horizontal/TE (i.e. parallel to the vertical rebar). . . . .	125
7.5	(a) Magnitude of co-polarized reflection coefficient and (b) transmission coefficient of the vertical rebar concrete wall of case A at normal incidence for horizontal polarization of incident field (wall thickness = 20.4 cm, metal thickness = 1.2 cm). . . . .	127
7.6	(a) Phase of co-polarized reflection coefficient and (b) transmission coefficient of the vertical rebar concrete wall of case A at normal incidence for horizontal polarization of incident field. . . . .	128
7.7	Co-polarized (a) reflected and (b) transmitted Bragg modes of the vertical rebar concrete wall of case A at normal incidence due to a horizontal (TE) polarization of incident field. . . . .	128
7.8	(a) Magnitude of co-polarized reflection coefficient and (b) transmission coefficient of the vertical rebar concrete wall of case B at normal incidence angle for horizontal polarization of incident field (wall thickness = 20.4 cm, metal thickness = 2.4 cm). . . . .	129
7.9	(a) Phase of co-polarized reflection coefficient and (b) transmission coefficient of the vertical rebar concrete wall of case B at normal incidence angle for horizontal polarization of incident field. . . . .	129
7.10	(a) Magnitude of co-polarized reflection coefficient, and (b) transmission coefficient of the vertical rebar concrete wall of case B at oblique incidence angle ( $\theta=150$ , $\phi=30$ ) for horizontal polarization of incident field. . . . .	130
7.11	(a) Phase of co-polarized reflection coefficient and (b) transmission coefficient of the vertical rebar concrete wall of case B at oblique incidence angle ( $\theta=150$ , $\phi=30$ ) for horizontal polarization of incident field. . . . .	130
7.12	(a) Magnitude of co-polarized reflection coefficient and (b) transmission coefficient of the crossed rebar concrete wall at oblique incidence angle ( $\theta=150$ , $\phi=30$ ) for horizontal (TE) polarization of incident field. . . . .	131
7.13	(a) Phase of reflection coefficient and (b) transmission coefficient of the crossed rebar concrete wall at oblique incidence angle ( $\theta=150$ , $\phi=30$ ) for horizontal (TE) polarization of incident field. . . . .	131

- 7.14 (a) Magnitude of co-polarized reflected and (b) transmitted Bragg mode scattered fields from a lossless vertical rebar concrete wall with metal thickness = 2.4 cm at normal incidence for horizontal (TE) polarization of incident field.  
(c) Power carried by the zeroth order mode is compared with the total power. 132

## LIST OF TABLES

### Table

3.1	Run time required for each realization of the forest and each incidence angle.	62
4.1	(a) The optimum polarization states, derived by genetic algorithm using 20 different seeds for initial population sets of 200 chromosomes for maximization of target to clutter backscattering RCS ratio. (b) Minimum target to clutter backscattering RCS ratio for H- and V- polarizations. . . . .	73
4.2	The optimum polarization states, derived by genetic algorithm using 100 different seeds for initial population sets of 200 chromosomes for optimization (4.10). . . . .	75

# CHAPTER 1

## Introduction

### 1.1 Background

Detection and classification of visually obscured targets has received a great amount of attention for many years. Such obscured targets can be targets embedded inside forests, objects behind walls, and buried land mines or under ground structures [1]-[5]. Such thrust research areas are among very challenging remote sensing problems which require a combination of different sensors and modalities, ranging from electromagnetics to acoustics, along with forward and inverse models and signal processing techniques to provide practical solutions. Having accurate solutions to such problems would make both civilian and law enforcement/military applications possible.

The basic ideas of detection and identification of objects are based on the phenomenology of wave propagation and scattering. Electromagnetic (EM) and acoustic waves can propagate through a random medium, be scattered or reflected back from objects and received by sensors. Since different objects usually have different scattering and reflection properties they can be detected and identified by sensors. Two examples of such sensors are human eyes and ears. Human eyes act as receiving sensors of visible light (i.e., EM waves) and human ears act as receiving sensors of sound (i.e., acoustic waves).

EM wave interaction with objects is manifested through many phenomena such as reflection, refraction, and scattering which have been originally introduced for visible light. The optical spectrum (i.e., visible light) is a portion of the EM spectrum that human eyes

can respond to. Other frequency bands, either higher or lower than visible light, reveal many properties that can not be explored at optical frequencies. Techniques and sensors for exploitation of the EM spectrum outside the visible region have been investigated and numerous applications have been identified. In the area of remote sensing much attention has been given to the lower frequency portion of the spectrum known as radio waves (30 Hz-300 GHz). This is mainly because, unlike visible light, radio wave propagation is unhampered by atmospheric effects such as clouds, dust, rain, snow, etc. This has suggested the use of radio waves for detection of obscured targets. One of the important tools that employs EM waves for this purpose is the Radio Detection and Ranging (radar) system.

Radar systems were implemented during World War II, for the first time. Using microwave frequencies, targets in dark and rainy weather were detected and ranged. Since that time, radar systems have been used for a variety of different applications such as air traffic control, astronomy, earth observation, etc. Basically, in radar systems the range resolution is provided by the frequency bandwidth. Depending on the wave penetration through materials and required resolution, different frequency bands are proposed for different applications. For example, VHF-band (50-330 MHz) is used for ground penetration, UHF-band (300-1000 MHz) is employed for ground penetration and foliage penetration, L-band (1-2 GHz) is used for long range air traffic control and surveillance, and S-band (2-4 GHz) is employed for terminal air traffic control and long range weather monitoring. Higher frequency bands are used in those applications that demand high resolution images. For example, at the highest portion of the radio spectrum, millimeter waves (40-300 GHz), radar systems provide very high-resolution images. They are very compact in size and can be used as visual sensors for example in experimental autonomous vehicles.

Many excellent ideas have been applied to radar systems to enhance their capabilities for detection and classification of targets [6], [7]. One of the most frequently used techniques is radar polarimetry [8], which relies on exploiting the polarization properties of targets. Since targets with different geometrical and physical properties generate different polarizations of the scattered field, their polarization signatures are different. This points to the fact that the analysis of the target's polarization response (i.e., radar polarimetry) can be exploited for discrimination of targets that can not be solely identified based on their radar cross

section (RCS) or position in the radar scene. In most applications the radar backscattering is composed of scattering from both the target and the clutter viewed by the radar. In such scenarios, radar polarimetry can also play an important role for discriminating the target from the background clutter. The literature concerning radar polarimetry is vast but a useful review article [9] has summarized target decomposition theorems in radar polarimetry .

Another advanced tool is the synthetic aperture radar (SAR) technique. SARs can provide two dimensional images of a scene with high resolution. The image is formed by a moving phase-coherent radar along a known track. One dimension, perpendicular to the radar track is called range, the line-of-sight distance from the radar to the target, and the other dimension is called cross-range, which is along the track. Like other radars, the resolution along the range is inversely proportional to the frequency bandwidth. For a real aperture radar, cross-range resolution is achieved by the antenna beamwidth. For instance, in optical systems (such as telescopes, human eye, etc) large apertures (i.e., mirrors and lenses) provide fine resolution images. However, since a SAR works at lower frequency bands, its required antenna becomes extremely large, not suitable for practical applications. To overcome the problem, a synthetic aperture is made by moving the radar system. The data collected along the radar track (i.e., synthetic aperture) is processed as if it was received by a large real-aperture antenna. In this system, the cross-range resolution is inversely proportional to the synthetic aperture length. Signal processing and applications of the SAR system can be found in [10] and [11], respectively.

Other advances that have contributed to the realization of highly sensitive radar systems include the progress made in microwave devices and components, the developments of millimeter wave sources, and the design of ultra-wideband and directive antennas such as reflector impulse radiating antennas and parabolic reflector antennas. These developments have extended the capability of radar systems for precise detection and characterization of physical and geometrical parameters of the targets.

## 1.2 Motivation and Objectives

While detection of targets in free space has been extensively investigated, detection of obscured targets, especially using EM wave that involves target and environment interactions, remains an emergent field that requires thorough and accurate investigation. In most practical problems of radar detection and identification of targets, the target is within a complex environment. This environment can be deterministic or random. In either case numerous scatters that comprise the environment interact with the target and can drastically modify the target inherent radar signature.

Consider a scenario where the target is placed inside a random medium (e.g., a tank under trees) and the radar system is outside of the medium. The radiated field from radar transmitting antenna, once it reaches the random medium, undergoes different phenomena such as attenuation, change of polarization, and scattering, before it arrives at the target location. The same types of variations occur when the scattered waves emanated from the target try to reach the receiving antenna. In addition to the attenuated wave, the target is illuminated by the scattered field from its surrounding scatterers. Likewise, the scattered field from the target illuminates the surrounding scatterers and creates secondary scattered field. This complex target and environment wave interaction makes target detection and identification a very difficult problem. Similar events can occur in cases where a target is inside semi-deterministic manmade environments such as building structures.

Because of the number and variety of factors impacting detection of obscured targets, comprehensive EM models are needed to understand the underlying behavior of the scattered fields from these targets. Such models should provide fully polarimetric signatures, both magnitude and phase of the scattered fields, and the statistics of fields for many different realizations of the clutter, different incidence angles, and observation points. Having such models, will guide researchers and engineers to develop new system concepts and algorithms that can eventually lead to practical methods for complex target detection and identification [12]-[14].

In this dissertation, two such important problems are investigated, one pertains to scattering from foliage-camouflaged targets, and the other deals with scattering from targets

behind walls. The first challenge for developing such models is the construction of realistic/physical model of the environment (clutter). Next is the development of accurate models for computation of propagation through and scattering by the clutter. The final challenge is the development of efficient computation methods for calculating the scattering from the hidden targets accounting for the impact of clutter on the target and vice versa. Having the forward models for computation of scattering from embedded targets, different techniques for improving the capability of radars in detection and identification of the embedded targets are investigated.

For detection of foliage-camouflaged targets, the applicability of radar polarimetry is examined. Polarimetric backscatter responses of a compound target inside a forest and the forest alone are analyzed to check whether there is a set of polarizations that can maximize the probability of obtaining the highest signal to clutter ratio. Many random realization of a pine stand forest around the same target are generated and the backscatter responses are used in an optimization problem to find the optimum set of polarizations. This problem is solved using genetic algorithms. On the other hand, for detection of targets behind walls the applicability of the SAR technique is inspected. In order to understand the effect of different walls on the target image both simulation and measurement data is gathered and refocusing techniques are presented to compensate for the effect of the walls and resume the target resolution. In the following subsections specific issues related to the construction of EM models for the two aforementioned problems are given.

### **1.2.1 Electromagnetic Scattering from Foliage Camouflaged Targets**

Detection and identification of hard targets camouflaged inside vegetation canopies are among the most challenging problems in remote sensing. This problem has both civilian and military applications such as search and detection of crashed airplanes and finding archaeological sites. To accomplish this task, first a comprehensive EM model is needed to characterize the scattered fields from camouflaged targets and to explore features in the scattered field that may help detection.

The literature contains many articles that have focused on the nature of the scattering from and propagation through forested environments [15]-[19]. However, the number of articles in the open literature related to the computation of scattering from targets inside the forest is small. Most studies related to foliage-camouflaged targets are of experimental nature [20], [21]. Experimental and empirical approaches for phenomenological studies are oftentimes rather limiting. This is due to the lack of a comprehensive data set and the accompanying ground truth. Few modeling efforts make use of exact numerical simulations such as FDTD technique for the evaluation of scattering from objects inside random media [22], [23]. The application of brute-force numerical methods is limited to VHF frequencies and lower. At microwave frequencies the overall dimensions of a tree are much larger than a wavelength, and therefore, computation of the scattered field from a number of trees and their interaction with the target becomes computationally intractable.

The objective of this thesis is to propose an accurate EM model for computation of scattering from foliage-camouflaged targets at microwave frequencies that accounts for first order near-field foliage and hard target interactions. This model is constructed from a number of analytic EM tools assembled in a unique fashion for fast and accurate computation of scattered fields, using well-known EM theorems. To simplify the problem, the scattering domain is broken into two parts. The first part of the problem is related to the computation of field propagation through and scattering from foliage. The second part of the problem pertains to the characterization of scattering from the target illuminated by the attenuated incident field and the scattered field from all nearby foliage particles. The connection between these two scattering domains is accomplished using the reciprocity theorem [24],[25].

The forest scattering model is based on the coherent scattering model developed previously [18], [19]. In this model, EM wave propagation through a forest canopy is treated by realistic models for trees, such as fractal-based models (Lindenmayer systems), and field computation is carried out using coherent scattering theories. In such a model the scattering from each tree component, when illuminated by the mean field, is calculated and the total scattering is expressed as the coherent summation of all the scattering contributions. The mean field, formulated by the aid of Foldy's approximation, accounts for the phase change as well as extinction due to the scattering and absorption by the tree particles [26].

On the other hand, the target model is based on either FDTD exact numerical analysis or high frequency asymptotic technique, iterative physical optics (IPO) approximation [27]-[30]. For ultra high frequency (UHF) band, scattering from the target is computed using FDTD technique [32]. At higher frequencies, computation of scattered fields from electrically large targets inside a forested environment constituting of multitudes of scatterers using exact numerical computation is intractable. Therefore, for these frequency bands (e.g. L-band), the IPO technique is used [31]. PO approach is widely used to estimate the scattering from large objects. This method is valid in directions near specular off of the scatterers. For the problem of scattering from the target inside a forest, there are multitudes of sources around the target. Therefore, with a very high probability there exists at least one specular reflection. This improves the accuracy of the approximation significantly. By iterating the PO computation, all the double-bounce scattering mechanisms are correctly accounted for. Furthermore, in the computation of PO currents, a shadowing rule is applied to correctly recognize the lit and shadow boundaries and improve the convergence of the iterative method.

The IPO numerical results of backscattering from different targets are either validated with exact numerical computations such as Method of Moment (MoM) using electric field integral equation (EFIE) or experimental data. The experimental data is achieved by using the University of Michigan fully polarimetric millimeter radar system, operating over the frequency range of 93-94 GHz, and a scaled model target. With this model, accurate measurements are performed in a fast and cost effective manner.

Having the hybrid target-foliage model, developed for investigating the scattering behavior of metallic hard targets embedded inside a forest canopy, at high frequencies many realizations of foliage around a hard target are run to obtain the statistical variations of foliage and target response in a Monte Carlo simulation. The fully polarimetric backscattering results of the target at 2 GHz are collected and a polarization synthesis optimization method for improving signal to clutter is presented, by applying genetic algorithms (GAs). It is shown that independent of forest realizations (tree arrangement around the target) there exists a set of polarizations that enhances signal to clutter ratio.

### 1.2.2 Through-Wall Imaging: Forward and Inverse Model

The other problem of interest is imaging of building interior and detection of targets behind building walls. This problem has applications in earthquake rescue operations, search and rescue police operations, etc. Challenges due to imaging of targets behind walls are two-fold. First, modeling of propagation through and scattering from different walls and building structures are needed. Next, having reliable EM models for computation of transmissivity through and reflectivity from various walls, imaging techniques such as SAR and beam-forming techniques are required to detect and identify hidden targets [33], [34].

From EM point of view, walls are categorized into two groups, 1) homogenous walls such as poured concrete, brick and adobe walls, and 2) inhomogeneous walls such as reinforced concrete walls, cinder block walls and drywalls. Walls in the first group are modeled by dielectric slabs. This model can predict the transmission and reflection coefficient properties of the walls with reasonable accuracy [35]. The ray-tracing technique has been used to compute the propagation through building structures composed of such walls [36], [37]. For the second group, accurate modelings are needed where inhomogeneities of such walls are accounted for. The periodic arrangements of these walls are used to provide correct models. Exact numerical techniques are employed to capture the EM properties of the walls [38], [39]. Bragg modes are excited as a result of interaction of EM waves with such periodic structures at frequencies where the periodicity is larger than half a wavelength.

The applicability of exact numerical methods are however limited by the relative size and complexity of the computational domain, available computer memory, and the computational efficiency. Therefore, for analyzing complex problems such as building structures composed of inhomogeneous and/or homogeneous walls the computational domains may be broken into parts, and numerical and analytical techniques are applied on each part of the problem. These hybrid methods have been introduced to reduce computation time and extend applicability of the simulation tools. For example, for simulation of buildings composed of both homogenous and inhomogeneous walls hybrid techniques based on finite difference time domain (FDTD) and ray-tracing techniques have been proposed in [40], [41].

The objective of this thesis is to understand the phenomenology of through-wall target

imaging. This includes first the study of transmissivity and reflectivity through different walls and second SAR imaging of hidden targets employing ultra-wideband signals and operating over a wide incidence angles. In this regard, analytical, numerical and experimental studies are accomplished for characterizing transmission through and reflection from different walls. For homogeneous walls the Fresnel reflection and transmission coefficients are used to address transmissivity and reflectivity of the walls. On the other hand, for inhomogeneous walls more accurate representations are given. For estimation of the propagation through cinder block walls, a hybrid FDTD and ray-optics approximation is provided [42] which is useful in efficient computation of transmissivity through walls whose extents are very much larger than the operating frequency wavelength. For reinforced concrete walls including vertical rebar and crossed-rebar concrete walls analytical formulas under the thin wire approximation are proposed [43]. The formulations are based on derivation of one-dimensional periodic Green's function where sources are inside a dielectric slab. For different wall parameters and incident angles analytical results are validated with exact FDTD simulation results. Using the approximate analytical formulations, fast and accurate scattering computations for plane wave incidences with arbitrary angles of incidence and polarizations are made possible.

Having these models, the problem of imaging through building structures can be investigated. In this thesis the application of SAR technique in imaging of targets behind single layer homogeneous walls are addressed through simulations and measurements [44]. Observations show that the attenuation through poured concrete walls is relatively high and therefore low microwave frequency bands (e.g. UHF band) is used to make EM waves penetrate through such walls. A scenario where the transceiver antenna is moving along the scan line and is away from the wall, possibly in the near-field region of the wall is considered and the effects of walls on the target images are addressed. It is shown that using usual SAR imaging technique the cross-range resolution is significantly degraded. Therefore, new algorithms are provided to enhance the cross-range resolutions and ability of radars in detection of close targets. To validate the simulation results, various experiments have been conducted. Point targets such as trihedral corner reflectors and spheres are placed behind poured concrete walls and it is shown that the effect of the walls on the target images can be effectively removed having the phase of transmissivity through the walls.

### 1.3 Dissertation overview

This dissertation consists of 8 chapters. Three early chapters are devoted to computation of EM scattering from foliage camouflaged targets, and the later chapters discuss through-wall imaging, which consist forward and inverse models.

Chapter 2 describes the foliage model, composed of introduction to fractal generation of trees, single scattering theory, distorted Born approximation, and Foldy's approximation. In this chapter, a hybrid FDTD and single scattering model for computation of scattering from complex targets such as civilian vehicles inside foliage is introduced and numerical simulation results at VHF frequency band are provided .

Chapter 3 proposes an EM scattering model for computation of scattering from foliage camouflaged complex targets at higher microwave frequencies as low as the L-band. This chapter examines the applicability of IPO approximation on computation of scattering from complex targets. The IPO approach is applied on a metallic tank that occupies a volume as big as  $86\lambda \times 33\lambda \times 20\lambda$ , and the RCS is provided for different incidence angles. The simulation results are validated with experiment data. For the experiment, the University of Michigan fully polarimetric millimeter radar system, operating over the frequency range of 93-94 GHz, in a stepped-frequency mode, is used to measure the backscattering from a scaled model tank. A scaling factor of  $s = 46.75$  is used to compare the measurements at 93.5 GHz with the simulation results at 2 GHz.

In Chapter 4, an optimization problem is solved, using the comprehensive foliage-target model developed in Chapter 3. In this problem a compound metallic target is considered inside a pine stand forest. For many realizations of forest around the target, statistical behavior of backscattered signals are studied. Basically, the received signal at the radar position is expressed as a summation of target and the clutter (i.e. foliage) responses. Sets of polarization configurations for transmitted and received waves are found such that the ratio of target RCS to clutter's RCS is maximized. This problem is solved by applying GAs.

The next two chapters provide modeling, simulation, and experiments of through-wall microwave imaging. Chapter 5 introduces refocusing through building walls, using SAR technique. This chapter consists of simulated and experimental results of imaging of point

targets behind homogenous walls such as poured concrete walls, using low microwave frequency bands (i.e. UHF band). The effect of the walls on the target images has been investigated and refocusing approaches have been proposed to compensate for the effects. Using these approaches detection of close targets with high resolutions is possible. Furthermore, a dual-frequency synthetic method is presented that can improve the cross-range resolution of the refocused images.

Chapter 6 addresses a hybrid FDTD ray optics model for computation of scattering from targets behind inhomogeneous walls such as cinder block walls. Wave interaction with such periodic structures excite Floquet modes at frequencies where the periodicity is larger than half a wavelength. These types of walls can significantly defocus a point target image and create multiple image points.

Chapter 7 introduces approximate analytical methods for computation of scattering from reinforced concrete walls. The formulation is based on derivation of the Green's function of a one-dimensional periodic structure inside a dielectric slab. The metal thickness is assumed small compared to the wavelength. The solution for two-dimensional periodic crossed-rebar concrete walls is also cast in terms of the one-dimensional periodic Green's function obtained for vertical rebar walls. The Bragg mode scattered fields of the reinforced walls are computed for different wall parameters and incidence angles for an operation frequency range of 0.5-2.0 GHz and validated by FDTD simulation results. Finally, Chapter 8 provides conclusions and future propositions.

## CHAPTER 2

# Hybrid FDTD and Single Scattering Theory for Simulation of Scattering from Hard Targets Camouflaged under Forest Canopy

A hybrid target-foilage model is developed to investigate the scattering behavior of hard targets embedded inside a forest canopy. The proposed model is composed of two existing electromagnetic scattering models, one for foliage and the other for the hard targets that are coupled in a computationally efficient manner. The connection between these two models, that accounts for the interaction between the foliage scatterers and the target, is accomplished through the application of Huygens' principle. Wave penetration through the forest canopy and near-field and far-field scattering from its constituents is calculated using a coherent single scattering theory which makes use of realistic tree structures. Defining a Huygens' surface enclosing the hard target and calculating the illuminating field (the scattered fields from the nearby vegetation scatterers and reduced incident field), the interaction between the foliage and the hard target is accounted for. Computing the scattered field from target on the Huygens' surface and using reciprocity theorem target-foilage interaction is captured very efficiently. Calculation of scattering from a hard target is carried out using a Finite Difference Time Domain (FDTD) technique. For a typical vehicle dimensions, the required time and memory for the FDTD computation and exact field calculation inside the foliage limits the simulation frequency to upper VHF band.

## 2.1 Introduction

Detection and identification of hard targets inside vegetation canopies have long been a challenging problem in the area of Remote Sensing. Development of theoretical and numerical models for this problem has a wide range of both civilian and military applications. The ability of electromagnetic waves to penetrate through foliage at low frequencies has made synthetic aperture radars (SARs) operating at VHF band, ideal tools for detection of targets in foliage [52], [53]. However, the scattering effect of the tree constituents can distort the signal phase front, reducing the SAR resolution and changing the target signature. In this regard a comprehensive phenomenological study is needed to accurately investigate the electromagnetic (EM) interaction of the foliage and an arbitrary hard target and vice versa. The literature concerning modeling the propagation through and scattering from forest canopies are many [54]-[15]. However the problem of accurate modeling of scattering from hard targets embedded inside tree canopies remains an unsolved problem [56],[57]. The difficulties associated with developing such model are three-fold, one is the accurate computation of the field inside a forest, the second is characterization of the scattered field from the target illuminated by the field inside the forest, and the third is the computation of the scattered field interaction with the foliage, and the total scattered field outside the forest at the observation point.

Considering the size of tree structures, the aspect ratio of the dimension of its constituent particles, the variability in dielectric constant of scatterers, and the relatively large number of trees around a target, brute force computational methods are not suitable for this problem. In addition applicability of exact numerical methods is limited to very low frequencies where scattering from leaves and branches can be totally ignored. However vegetation canopies can be viewed as a sparse random medium, having a volume fraction typically less than 1%. For such media multiple scattering among constituent scatterers are of secondary importance and can be ignored. In this case EM scattering from vegetation canopies can be simplified in terms of problems of scattering from individual dielectric cylinders and thin dielectric disks, modeling branches and leaves, arranged in a semi-deterministic fashion. The formulations for calculating the scattering and attenuation caused by vegetation particles have been derived

analytically, using high- and low-frequency techniques [54], [55]. The effect of ground plane is also accounted for, through the application of image theory maintaining only the saddle point contribution. For precise prediction of the field behavior inside the canopy, structure of the trees is preserved in the forest model. This is done using a fractal-based model (known as Lindenmayer systems), that can generate very complex tree structures with a finite number of structural and botanical parameters. Monte Carlo coherent single scattering model, which makes use of fractal-generated trees, has been proposed in [18] and [19] to estimate the scattering from and propagation through the forest canopy. In this model the coherent summation of all scattering contributions, including those from the ground plane, is computed to find the total field at a given point within the forest canopy. This total field is used as the excitation source for the hard target.

For the problem of EM scattering from an isolated target of arbitrary shape a number of approximation and numerical approaches may be used. In VHF frequency band (20-200 MHz), high frequency approximation techniques are not usually applicable for typical ground vehicles, where the wavelength is comparable to the vehicle dimensions. Therefore, exact numerical approaches such as MoM or FDTD are appropriate to treat the scattering problem. In past, FDTD technique has been widely used for simulation of scattering for a wide range of scattering problems [25]-[22]. To get the benefit of FDTD accurate analysis for complex targets and yet to account for scattering interaction with nearby vegetation in a computationally tractable manner, we use a hybridization of FDTD with the coherent single scattering model for the forest.

The main contribution of this chapter is in construction of a foliage-target model that is computationally tractable and can provide accurate results. This model accounts for scattering from foliage, hard target, and near-field interaction of foliage and the hard target. In what follows, first we derive a general formulation for backscattering from a target above the ground plane and embedded in foliage, illuminated by a plane wave of arbitrary polarization. This formulation makes use of the forest model for computation of the near-field scattering from the trees over a Huygens' surface enclosing the target and a full-wave FDTD formulation for computation of scattered field from the target on the same Huygens' surface. Reciprocity is used to compute the radiated field from the Huygens' surface at the observa-

tion point [25], [23]. The model is validated using an iterative physical optics (IPO) [27]-[30] in conjunction with physical theory of diffraction (PTD) solution applied to a dihedral corner reflector in free space and above the dielectric half space. Having the hybrid model (FDTD + Huygens' surface approach + reciprocity) validated, the model is then used to simulate the polarimetric radar response of a metallic vehicle under foliage.

## 2.2 Theory

In this section the basic formulation of the proposed hybrid time and frequency domain method for studying accurate radar backscatter response of foliage-camouflaged targets is presented. The overall model is composed of three basic components: 1) a frequency domain forest model, 2) FDTD model for the hard target, and 3) an algorithm that interfaces the forest and target models and allows for computation of target-foliage scattering interaction in an efficient manner.

### 2.2.1 Coherent Forest Model

For developing an electromagnetic scattering method for detection and identification of hard targets embedded inside vegetation canopies a comprehensive physics-based model is needed. Such model must be able to preserve the phase of the backscatter so that SAR, interferometric SAR, and polarimetric SAR simulations are possible. In single scattering theory, field computation is carried out coherently, to preserve the phase of the scattered fields. Such a model is implemented in [18] where the scattering from each tree component, when illuminated by the mean field, is calculated and the total scattering is expressed as the coherent summation of all the scattering contributions. This model is capable of accurate estimation of polarimetric radar response from forested environments. In the following we review the basic concept and mathematical formulations used in this model [15], [59].

It has been demonstrated that tree structures have significant effects on the radar backscatter response of the tree canopy as well as propagation behavior of the signal going through the forest [45]. Implementation of Lindenmayer system (L-system), using fractal theory has shown to be an effective approach for including the tree structures in the electromagnetic

scattering model [60]-[62]. Basically in L-system, the structures of the trees are generated through a rewriting process [63], using a finite number of botanical and geometrical parameters. In this model, tree constituent components such as branches and leaves are represented by dielectric cylinders and thin dielectric disks, respectively and arranged in a semi-deterministic fashion. Then, the single scattering theory based on distorted Born approximation is used, where for every scatterer inside the forest illuminated by the mean-field, the scattered field is computed at the observation point and the total scattered field is expressed as a coherent sum of all scattering contributions. Therefore, the total scattered field  $\bar{E}^s$  can be mathematically expressed as

$$\bar{E}^s = \frac{e^{ikr}}{r} \sum_{n=1}^N e^{i\phi_n} S_n \cdot \bar{E}_n^i \quad (2.1)$$

where  $N$  is the total number of scatterers,  $S_n$  is the scattering matrix of the  $n$ th scatterer, and  $\phi_n$  is a path delay phase given by  $\phi_n = (\hat{k}_i - \hat{k}_s) \cdot \bar{r}_n$ . Here  $\bar{r}_n$  is a vector denoting the location of the  $n$ th scatterer, and  $\hat{k}_i$  and  $\hat{k}_s$  are the propagation unit vectors along the direction of incident and scattered fields, respectively. The scattering from tree constituent components  $S_n$  is calculated in the presence of a dielectric half space representing the ground plane. Using geometric optics approximation, scattering from each scatterer can be decomposed into four components: 1) direct  $S_n^t$ , 2) ground-scatterer  $S_n^{tg}$ , 3) scatterer-ground  $S_n^{gt}$ , and 4) ground-scatterer-ground  $S_n^{gtg}$ . Therefore the scattering matrix  $S_n$  can be written as

$$S_n = S_n^t + S_n^{gt} + S_n^{tg} + S_n^{gtg} \quad (2.2)$$

The model presented in [18], makes use of far-field expressions for scattering matrices used in (2.2). This model is used to compute the backscattered field from the foliage alone in the far-field region. A more advanced model was developed in [19], where the observation point can be placed inside the forest, possibly in the near field of some scatterers. Scattering formulations for individual scatterers were modified to achieve a uniform scattering solution for scatterers valid from near-field to far-field regions. For the computation of scattered field at a point inside the forest, distorted Born approximation is invoked [15]. That is

each scatterer is assumed to be inside an effective homogeneous medium and illuminated by a mean field, composed of two components, 1) direct and 2) reflected from the ground. Therefore in (2.1),  $\bar{E}_n^i$  is the mean field calculated at each scatterer location and similarly, in the calculation of the scattering matrix in (2.2) the presence of such equivalent medium is considered.

Calculation of the mean field is carried out using Foldy's approximation [15]. According to Foldy's approximation, inside a uniform random medium the coherent part of the field (mean field)  $\bar{E}$ , has the following variation with respect to the distance  $s$  along the propagation direction  $\hat{k}$

$$\frac{d\bar{E}}{ds} = iK \cdot \bar{E} \quad (2.3)$$

where

$$K = \begin{bmatrix} k_0 + M_{vv} & M_{vh} \\ M_{hv} & k_0 + M_{hh} \end{bmatrix} \quad (2.4)$$

and

$$M_{pq} = \frac{2\pi n_0}{k_0} \langle S_{pq}^0(\hat{k}, \hat{k}) \rangle \quad (2.5)$$

In (2.5),  $n_0$  is the volume density of the scatterers,  $k_0$  is the propagation constant in free space, and  $\langle S_{pq}^0(\hat{k}, \hat{k}) \rangle$  is the ensemble average of the forward scattering matrix, where  $p$  and  $q$  can be  $v$  or  $h$  for vertical or horizontal polarizations, respectively. Solution for (2.3), is given by  $\bar{E} = e^{ik_0s} T(s, \hat{k}) \cdot \bar{E}^0$ , where  $\bar{E}^0$  is the field at  $s = 0$ . Matrix  $T$  is called the transmissivity matrix, and is given by

$$T = \begin{bmatrix} e^{iM_{vv}s} & e^{iM_{vh}s} \\ e^{iM_{hv}s} & e^{iM_{hh}s} \end{bmatrix} \quad (2.6)$$

It is noted that the imaginary part of  $M_{pq}$ , called extinction coefficient, accounts for the extinction of the mean field propagating inside the random medium. This is due to the scattering and absorption caused by random particles. To account for variability in particle shape and distribution along the vertical extent of the forest stand, the random medium (forest stand) is divided into  $M$  homogeneous strata with different effective dielectric con-

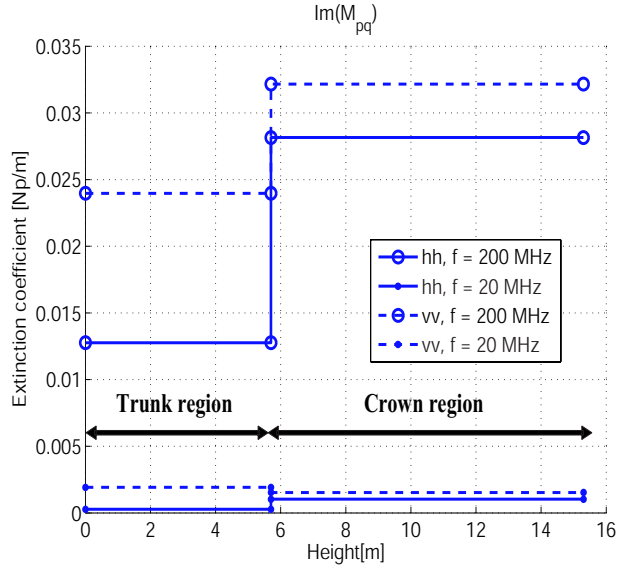


Figure 2.1: Extinction profile of pine tree stand with density of  $0.05 \text{ trees}/m^2$  for incidence elevation angle of  $30^\circ$ .

stants. Based on Foldy's approximation (2.5), the propagation constant of each layer is proportional to the ensemble average of the forward scattering matrix elements of scatterers inside that layer [15]. It is noted that the boundaries between the layers are diffuse where no reflection or refraction take place. For determining the number of layers  $M$ , the code starts with a moderate number of layers. Then the extinction of each layer is calculated. If the discontinuity of extinction between any two layers is bigger than a pre-defined threshold, then the forest stand is divided into finer layers.

Figure 2.2.1 shows the simulated extinction profile of a pine stand with a tree number density of  $0.05 \text{ trees}/m^2$  versus height at two different frequencies and polarizations. As shown, we observe higher attenuation coefficient for higher frequency than that of lower frequency due to the scattering and absorption losses of vegetation particles. According to Rayleigh scattering, at low frequencies the scattering matrix  $S_{pq}^0(\hat{k}, \hat{k})$  is proportional to  $k_0^2$  [64]. Therefore, according to (2.5) the extinction coefficient is proportional to  $k_0$ . As shown in Fig. 2.2.1, it is expected that extinction at 200 MHz be about 10 times higher than that at 20 MHz. In addition vertical polarization of incident field has higher extinction coefficient than horizontal polarization because of the specific arrangement of scatterers in

the tree structure. Due to higher volume density of scatterers, the crown region shows higher extinction coefficient than trunk region except for very low frequencies where vertical polarization experiences slightly more attenuation in trunk region compared to the crown region.

### **2.2.2 Computation of Local Scattered Field Using FDTD**

FDTD technique is a very versatile full wave numerical approach appropriate for targets of arbitrary geometry and material properties and for characterization of scattered field over a wide range of frequencies [65], [66]. Although FDTD formulation is very general, for a very large computation domain such as the foliage camouflaged target, the computation time and the required memory become prohibitively large [23]. Another level of difficulty in the brute force application of FDTD is the aspect ratio of the dimensions of scatterers such as broad leaves and needles. Because of these difficulties the computational domain is limited to the target itself excluding the surrounding foliage. In order to calculate the scattered field from target using FDTD, the computational domain is divided into the total-field and scattered-field regions separated by a virtual interface enclosing the target. This interface serves as a connecting boundary over which the difference between the total field and scattered field (incident field) is imposed [65]-[67]. The target structure is located inside the total field region surrounded by the virtual rectangular box. Using the forest model, the field on the FDTD box is computed and considered as the incident field for the target. Using FDTD scheme, scattered field by the target itself is calculated at the same grid points on the box, and then using a scheme based on reciprocity theorem the backscattered field at the radar position is computed.

### **2.2.3 Computation of Backscattered Field**

The backscatter field from a target inside the forest canopy is composed of two main components. The first component is the direct scattering from the target simply attenuated by the foliage above, and second component contains the scattered field interaction between the foliage and the target as well as the target and the foliage. In order to calculate the

backscattered field from a target inside the forest canopy without the computation of scattering interaction of target radiated field and the surrounding foliage, the reciprocity theorem can be used. The application of reciprocity for computation of first order scattering interaction between two objects have been demonstrated in past [68]. This method in conjunction with a Huygens' surface is used here to account for interaction of a random media with a complex hard target. According to the reaction theorem, for two sets of sources and fields, denoted by 1 and 2, we have [69],

$$\int_{V_2} (\bar{E}_1 \cdot \bar{J}_2 - \bar{H}_1 \cdot \bar{M}_2) d\mathbf{r} = \int_{V_1} (\bar{E}_2 \cdot \bar{J}_1 - \bar{H}_2 \cdot \bar{M}_1) d\mathbf{r} \quad (2.7)$$

where  $\bar{E}$  and  $\bar{H}$  are electric and magnetic fields, and  $\bar{J}$  and  $\bar{M}$  are the electric and magnetic current sources, respectively.  $\bar{E}_1$  and  $\bar{H}_1$  are fields generated by  $\bar{J}_1$  and  $\bar{M}_1$  at the location of the second sources  $\bar{J}_2$  and  $\bar{M}_2$  and similarly  $\bar{E}_2$  and  $\bar{H}_2$  are produced by  $\bar{J}_2$  and  $\bar{M}_2$  at  $\bar{J}_1$  and  $\bar{M}_1$  location. For problem at hand we consider elementary current sources  $\bar{J}_1$  and  $\bar{M}_1$  at the radar location and induced currents on target as the secondary sources. Consider an elementary current source  $\bar{J}_1$  at the radar position  $\bar{r}_R$ , oriented along a polarization unit vector  $-\hat{p}$  given by

$$\bar{J}_1 = \frac{4\pi}{ik_o Z_o} \frac{r_R}{e^{ik_o r_R}} \delta(\bar{r} - \bar{r}_R) (-\hat{p}) \quad (2.8)$$

Here  $k_o$  and  $Z_o$  are the propagation constant and characteristic impedance of the free space, respectively and we assume  $\bar{M}_1 = 0$ . This source produces  $\hat{p}$ - polarized field at the far-field region. The unit vector  $\hat{p}$  can be chosen  $\hat{h}_i$  or  $\hat{v}_i$  for horizontal or vertical polarization respectively. These unit vectors in a global coordinate system are defined by

$$\begin{aligned} \hat{h}_i &= \frac{\hat{k}_i \times \hat{z}}{|\hat{k}_i \times \hat{z}|} \\ \hat{v}_i &= \hat{h}_i \times \hat{k}_i \end{aligned} \quad (2.9)$$

where  $\hat{k}_i$  is the unit vector along the propagation direction of the incident field. Substituting (2.8) in (2.7), we have

$$\overline{E}_2 \cdot (-\hat{p}) = \frac{ik_o Z_o}{4\pi} \frac{e^{ik_o r_R}}{r_R} \int_{V_2} (\overline{E}_1 \cdot \overline{J}_2 - \overline{H}_1 \cdot \overline{M}_2) d\mathbf{r} \quad (2.10)$$

Hence once the incident field and the induced currents on a target are known the backscattered field can be computed from (2.10). Using (2.10), each component of the scattering matrix can be computed from

$$\mathbf{S}_{pq} = \pm \frac{ik_o Z_o}{4\pi} \int_{V_2} (\overline{E}_{1p} \cdot \overline{J}_{2q} - \overline{H}_{1p} \cdot \overline{M}_{2q}) d\mathbf{r} \quad (2.11)$$

where  $p$  and  $q$  represent the  $h$  or  $v$  polarizations. The first and second subscripts of scattering elements denote the receive and transmit polarizations, respectively. Since for backscatter direction  $\hat{k}_s = -\hat{k}_i$ , we have  $\hat{h}_s = -\hat{h}_i$  and  $\hat{v}_s = \hat{v}_i$ , the minus sign in (4.1) is chosen when the receive polarization is vertical. Finally, the Radar Cross Section (RCS) of the target is calculated from,

$$\sigma_{pq}^s = 4\pi |\mathbf{S}_{pq}|^2 \quad (2.12)$$

In (2.7), the electric and magnetic currents  $\overline{J}_2$  and  $\overline{M}_2$ , are generally any equivalent electric and magnetic currents that can be directly computed on the target surface or on a hypothetical surface enclosing the target. These equivalent currents can produce the same scattered field as these produced by the physical induced currents. Using Huygens' principle, the tangential surface fields over a general closed surface that contains only the target (and not the foliage) are sufficient to generate the equivalent currents. Figure 2.2.3 shows a fictitious rectangular box with surface  $\mathbf{S}$  around the target. Denoting the scattered field outside  $\mathbf{S}$  by  $\overline{E}_2$  and  $\overline{H}_2$ , then according to Huygens' principle we have,

$$\begin{aligned} \overline{E}_2(\vec{r}') = \int_{\mathbf{S}} [ik_o Z_o (\hat{n} \times \overline{H}_2(\vec{r})) \cdot \overline{\overline{G}}(\vec{r}, \vec{r}') + \\ (\hat{n} \times \overline{E}_2) \cdot \nabla \times \overline{\overline{G}}(\vec{r}, \vec{r}')] ds \end{aligned} \quad (2.13)$$

where  $\overline{\overline{G}}(\vec{r}, \vec{r}')$ , is the Dyadic Green's function for the media, and  $\hat{n}$  is the normal unit vector

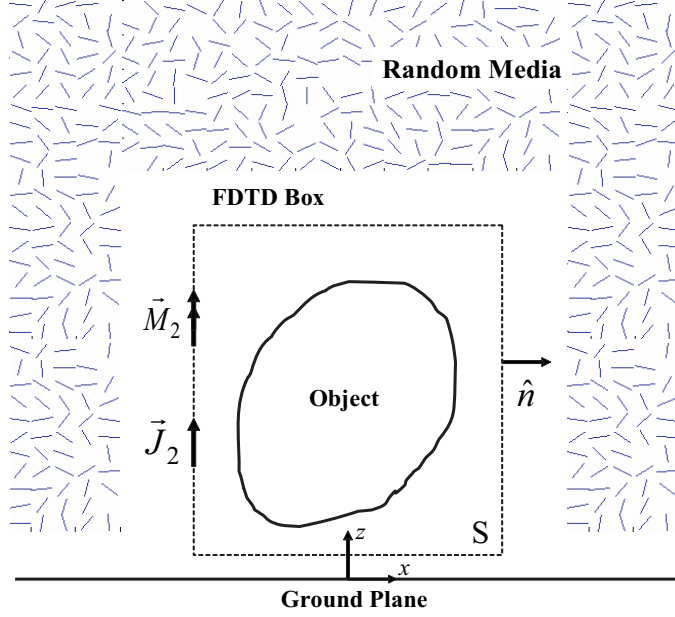


Figure 2.2: Geometry of the problem. Surface  $\mathbf{S}$  is containing an object above the ground plane.

pointing outward. Note that for complex random media such as a forest canopy the exact computation of the Green's function is not possible and therefore computation of scattered field in the presence of the random media in a direct manner is not possible. The quantities  $(\hat{n} \times \overline{H}_2)$  and  $(-\hat{n} \times \overline{E}_2)$  can be interpreted as the equivalent electric and magnetic surface current densities respectively. That is

$$\begin{aligned}\overline{J}_2(\vec{r}) &= \hat{n} \times \overline{H}_2(\vec{r}) \\ \overline{M}_2(\vec{r}) &= -\hat{n} \times \overline{E}_2(\vec{r})\end{aligned}\tag{2.14}$$

Substituting (2.14) in (4.1), it can be shown that

$$\mathbf{S}_{pq} = \pm \frac{ik_o Z_o}{4\pi} \int_{\mathbf{S}} [\overline{H}_{2q} \times \overline{E}_{1p} + \overline{E}_{2q} \times \overline{H}_{1p}] \cdot \hat{n} ds\tag{2.15}$$

For our problem, the incident fields on the target  $\overline{E}_1$  and  $\overline{H}_1$  are composed of the superposition of scattered fields from all tree constituents such as branches, trunks, and leaves, and the direct field attenuated by the foliage (mean field). Each of these field components can

be decomposed into a direct and a reflected field from the ground plane. For a  $\hat{p}$ - polarized incident plane wave

$$\begin{aligned}\bar{E}_{1p} &= (\bar{E}_d + \bar{E}_r)_{mean} + \sum_{Scatterers} (\bar{E}_d + \bar{E}_r) \\ \bar{H}_{1p} &= (\bar{H}_d + \bar{H}_r)_{mean} + \sum_{Scatterers} (\bar{H}_d + \bar{H}_r)\end{aligned}\quad (2.16)$$

where the subscripts  $d$  and  $r$  stand for the direct and reflected fields, respectively.  $\bar{E}_2$  and  $\bar{H}_2$ , on the surface  $\mathbf{S}$ , are computed using FDTD technique, described in the previous section. Since the fields computed by the forest model are in frequency domain and the input to the FDTD code must be in time domain a frequency to time domain transformation is needed. Depending on the desired frequency range of simulation the complex total field quantities from  $f_{start}$  to  $f_{stop}$  are computed over the FDTD box at  $N$  discrete frequency points. The choice of  $N$  (increments in frequency) depends on the size of the FDTD box or equivalently the alias-free time domain period. Once the frequency domain fields are computed the time domain representations are calculated by

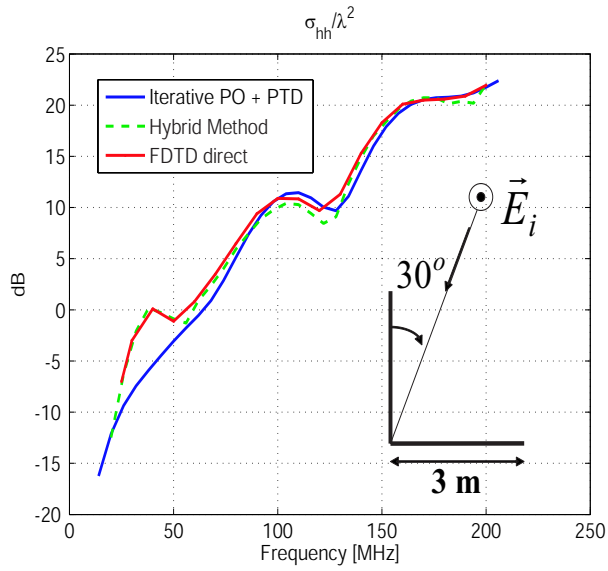
$$\begin{aligned}\bar{\varepsilon}_1(t) &= 2 \text{Real}\left\{ \int_{f_{start}}^{f_{stop}} \bar{E}_{1q} e^{-i2\pi ft} df \right\} \\ \bar{\zeta}_1(t) &= 2 \text{Real}\left\{ \int_{f_{start}}^{f_{stop}} \bar{H}_{1q} e^{-i2\pi ft} df \right\}\end{aligned}\quad (2.17)$$

To alleviate the effects of abrupt frequency truncations which results in high time domain side lobes, a Gaussian weighting function can be introduced in (2.17). The output of FDTD simulation for tangential fields is in time domain and the fields quantities required in (2.15) are in frequency domain. Denoting the time domain response of the scattered fields computed by FDTD simulation by  $\bar{\varepsilon}_2(t)$  and  $\bar{\zeta}_2(t)$ , the scattered fields in frequency domain are obtained from

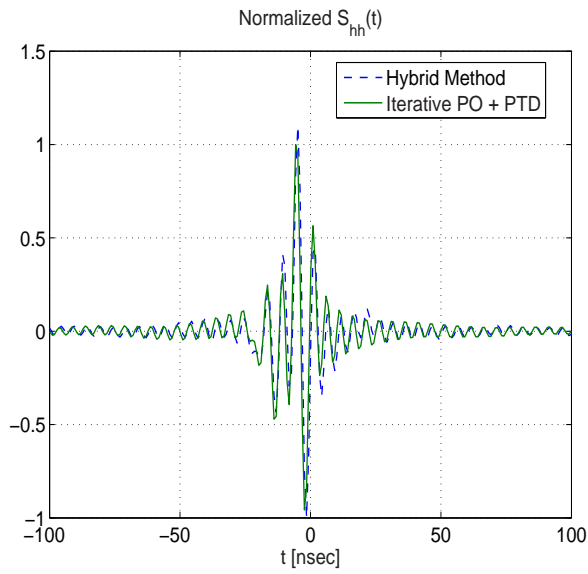
$$\begin{aligned}\bar{E}_{2q} &= \int_{-\infty}^{+\infty} \bar{\varepsilon}_2(t) e^{+i2\pi ft} dt \\ \bar{H}_{2q} &= \int_{-\infty}^{+\infty} \bar{\zeta}_2(t) e^{+i2\pi ft} dt\end{aligned}\quad (2.18)$$

Expressions of (2.16) and (2.18), are used in (2.15) for calculation of the backscattered field. It should be noted that with this technique only the first-order scattering interaction is taken into account. To demonstrate the validity of the proposed hybrid frequency domain and time domain method a  $3m \times 3m$ , metallic dihedral corner reflector in free space is considered. A plane wave illumination is assumed and simulation is desired over a frequency range of 14 – 206 MHz. Since the target is inside an FDTD box with size of  $3.96m \times 3.96m \times 3.96m$ , maximum frequency increment  $\Delta f = 43.74$  MHz is required to have alias-free time domain response. For this simulation we used  $\Delta f = 6$  MHz (N=33). The cell size in FDTD code is set to 12 cm which is smaller than  $\lambda/10$  at the highest simulation frequency. Due to the size of the FDTD box and cell size, time span of about 212 nsec with time step of 0.83 nsec is considered in FDTD to provide an accurate solution. For the hybrid time and frequency domain approach first the incident field quantities are computed as a function of frequency over the FDTD box and then the process described above was followed. Figure 5.9 shows the backscatter RCS of the dihedral, using direct FDTD, the hybrid approach, and a totally independent approach using iterative physical optics approximation and PTD [27]-[30]. Figure 5.9(a) shows the RCS as a function of frequency for an H-polarized incident plane wave, propagating along  $\theta_i = 30^\circ$  and  $\phi_i = 180^\circ$ . Figure 5.9(b) shows the same result in time domain. Since the FDTD box is centered above the origin, non-zero backscattered signal is also observed for negative times. As shown an excellent agreement exists between direct FDTD and the hybrid approach. The small discrepancies are due to the effect of the discretizations in time, space, and frequency domains. Also there is a very good agreement between the iterative PO+PTD and the numerical results at high frequencies ( $f > 50$  MHz) where the high frequency approximation method is expected to work. A difficulty may arise due to the presence of the ground plane. The total incident field on the target is the superposition of the incident field and its reflection on the ground plane. In situations where the target is sufficiently above the ground plane the superposition of the incident field and reflected field can be used as the total incident field on the target. However in cases where the target is sitting on the ground, the target shadows the ground and no reflected fields from the shadowed region are generated. In this model, the effect of shadowing is accounted for, in an approximate manner by placing a perfectly absorbing layer on the ground over the

shadowed area, as shown in Fig.2.4(a). Figure 2.4(b) shows a comparison of backscattering RCS from a dihedral corner reflector, above a dielectric ground plane with  $\epsilon_r = 5.62 + i 0.94$ , calculated once using the proposed hybrid method then using PO + PTD approximation for an H-polarized incident plane wave propagating along  $\theta_i = 30^\circ$  and  $\phi_i = 180^\circ$ . A very good agreement is shown at high frequencies ( $f > 60$  MHz) where the iterative PO + PTD is expected to work properly.

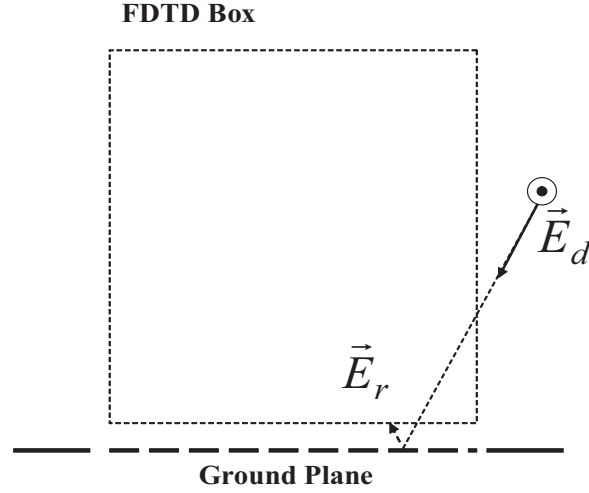


(a)

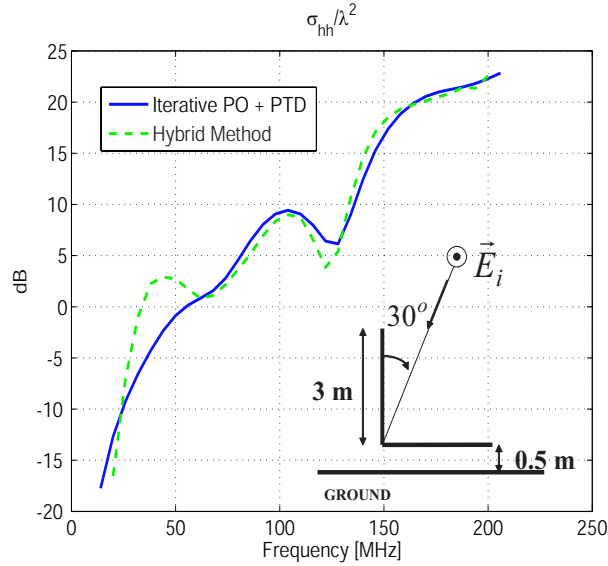


(b)

Figure 2.3: Comparison of backscattering RCS from a dihedral corner reflector in free space, calculated by direct FDTD, hybrid method, and physical optics + PTM approximation for an H-polarized incident plane wave propagating along  $\theta_i = 30^\circ$  and  $\phi_i = 180^\circ$ . (a) Frequency domain. (b) Time domain.



(a)



(b)

Figure 2.4: (a) Geometry of the scattering problem when the effect of ground plane exists. (b) Comparison of backscattering RCS from a dihedral corner reflector, above a dielectric ground plane with  $\epsilon_r = 5.62 + i 0.94$ , calculated by the hybrid method, and physical optics + PTD approximation for an H-polarized incident plane wave propagating along  $\theta_i = 30^\circ$  and  $\phi_i = 180^\circ$ .

## 2.3 Numerical Simulations of Foliage Camouflaged Targets

To study the importance of foliage in modifying the RCS values of foliage camouflaged targets, simulation of backscatter responses of metallic targets in a pine forest stand is

examined. First we consider the metallic dihedral corner reflector, used in the previous simulations (each panel is  $3m \times 3m$ ). For this simulation the dihedral is placed  $0.5m$  above a lossy ground plane, having a relative permittivity of  $\epsilon_r = 5.62 + i 0.94$ . It is assumed that the target is surrounded by 8 nearby trees (see Fig.2.6(c)). These trees are generated by the statistical L-system having maximum height of  $15.3 m$ , crown radius of  $3 m$ , crown height of  $9.6 m$ , trunk radius of  $10.9 cm$ , and more than 5000 branches per tree. Since the target in the forest can be fit within a volume with a maximum linear dimension of about  $22.65m$ , the maximum frequency increment  $\Delta f$  must be less than  $13.25$  MHz to have alias-free time domain response. For this example the following parameters were chosen,  $\Delta f = 6$  MHz, cell size =  $12 cm$ , time span =  $212 nsec$ , time step =  $0.83 nsec$ . To make the code faster and at the same time observe accurate results, only scattering effects of branches which have radii more than  $0.01\lambda$  have been calculated. Other scatterers contribute only to the signal attenuation.

Figures 2.5(a)-(d) show the backscattered RCS response of the dihedral as a function of frequency once with and once without foliage, for basic radar polarization configurations. The backscatter responses of the target embedded in foliage shown in these figures do not include the forest backscatter itself. As shown, at lower frequencies the effect of forest on modifying the backscattered response of the target is negligible. However for higher frequencies the effect of forest is observed in reducing and distorting the RCS pattern. At frequencies below  $70$  MHz the foliage scattering interaction contribution is much smaller than the dihedral scattering by itself and thus in this case the polarimetric target signature does not change. For the same arrangement of the trees a simulation is carried out for a complex metallic vehicle (see Fig. 2.6(a)) inside the FDTD box with dimensions of  $5m \times 5m \times 5m$  (see Fig. 2.6(c)), placed inside the forest. For this simulation we used  $\Delta f = 6$  MHz ( $N=33$ ) and the cell size of  $10 cm$ . This surface of the FDTD box is composed of  $62,424$  pixels for which the forest fields must be calculated. Due to the size of the FDTD box and cell size, a time span of about  $176 nsec$  with a time step of  $0.69 nsec$  is required for the FDTD technique to provide accurate results. Figure 6.3(a)-(f) compare the frequency response of the backscatter from the target for standard polarization configurations, once with and once without foliage. As before the response of the target includes the foliage interaction (foliage

target and target foliage). The computation time for this simulation is estimated about 3 days, using two AMD Athlon processors, with 2 GHz CPU and 1 GB RAM. The scattering computation results provided here are run by PC for one realization of pine stand forest, including 8 pine trees. In fact using parallel computers more number of realizations of forest can be simulated.

Practically, the radar received signal is the coherent summation of the target and the forest backscatter responses. The dihedral and the vehicle in previous simulations are used as targets inside the forest. Figure (2.8) compares total backscattering from the target and the forest, the forest alone and the target, for horizontal and vertical polarizations of incident fields. Scattering from all 8 pine trees are included in the forest response. As shown the backscatter response of the camouflaged target is significantly distorted by the forest. It is observed that from frequencies above 60 MHz, the signature of the target response is changing which makes target detection very difficult. Target discrimination approaches, such as polarization signature and polarization optimization study are needed for identifying the target in a strong clutter environment.

## 2.4 Conclusions

At very low frequencies, scattering from the forest itself may be rather small, and the effect of forest on scattering behavior from the hard target can be carried out by applying a simple attenuation on RCS, and increase on propagation phase constant. However, at high frequencies the forest distorts the incident wave phase-front, as well as its polarization significantly. To show this, a hybrid foliage-target model is developed. The hybrid model is composed of two scattering models, the foliage model and the full-wave hard target scattering model. The foliage scattering model uses the single scattering theory applied to realistic looking tree structures generated by a fractal model known as Lindenmayer systems. The target scattering is computed by FDTD. The connection between these two models, that accounts for the interaction between the foliage scatterers and the target is carried out through the application of reciprocity theorem. This model has ability to characterize the scattering from camouflaged complex targets inside the forest canopy, accurately. Simulations of

scattering from hard targets embedded inside a forest canopy, in VHF frequency band (20-200 MHz), was carried out using proposed hybrid model. Based on simulation results, it is observed that the signature response of a camouflaged vehicle with typical dimensions of  $4m \times 2m \times 1.5m$  inside a pine forest with density of about  $0.05 \text{ trees}/m^2$  is significantly changed for frequencies above 60 MHz. Clearly, the electric size of the target as well as forest parameters, such as density of the trees, determine this frequency.

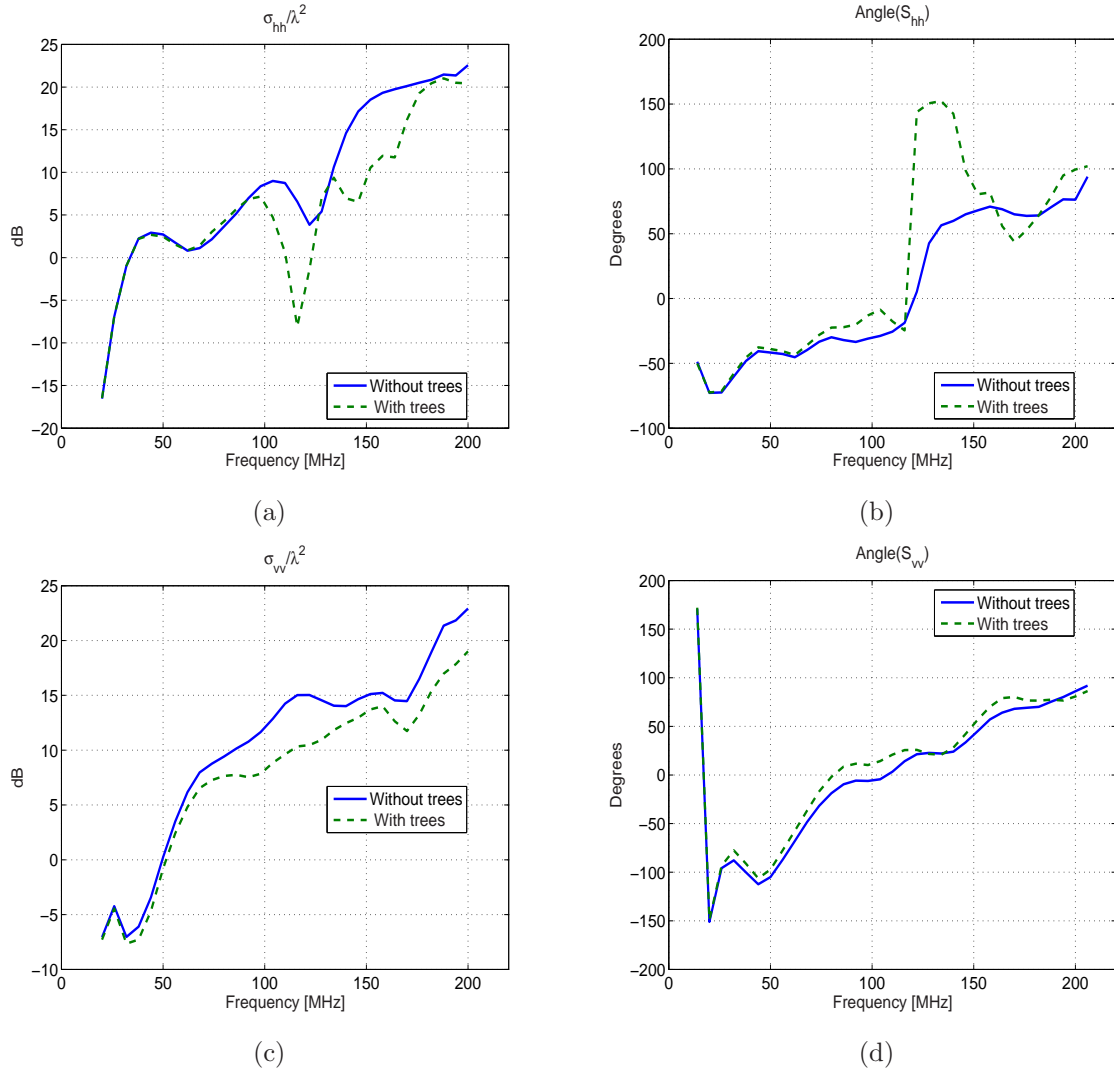


Figure 2.5: Comparison of backscattering RCS from a dihedral corner reflector (each panel is  $3m \times 3m$ ), placed 0.5 m above a dielectric ground plane with  $\epsilon_r = 5.62 + i 0.94$ , calculated by the hybrid method, inside and outside of the forest for standard polarization configurations of incident plane wave propagating along  $\theta_i = 30^\circ$  and  $\phi_i = 180^\circ$ . (a)  $\sigma_{hh}/\lambda^2$  (b) Angle( $S_{hh}$ ) (c)  $\sigma_{vv}/\lambda^2$  (d) Angle( $S_{vv}$ ).

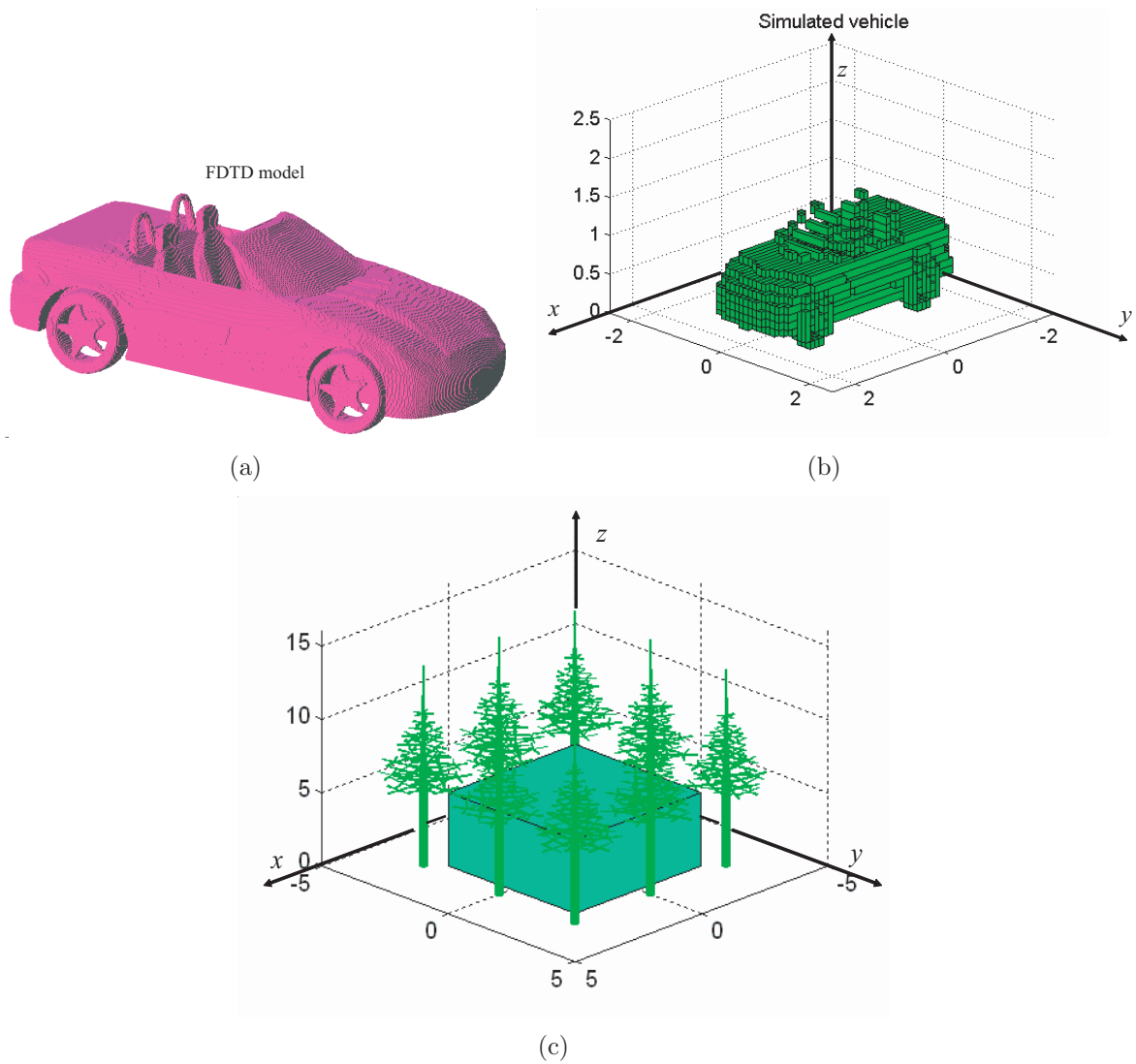


Figure 2.6: (a) FDTD model of the hard target with fine resolution mesh ( resolution  $\approx 1$  cm ), (b) course FDTD mesh (resolution = 10 cm), used for VHF simulation, and (c) the FDTD box located inside a forest, including eight pine trees.

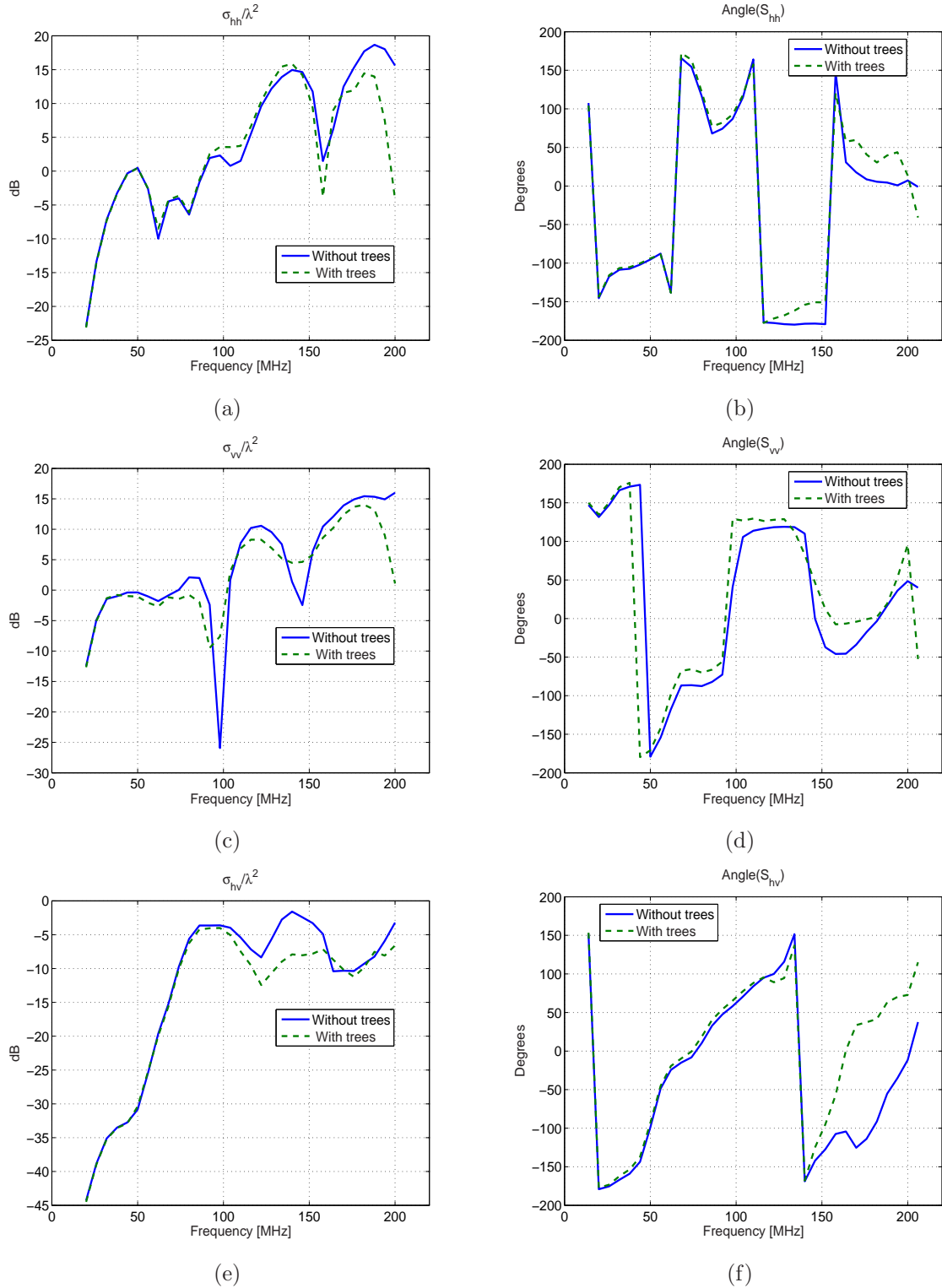


Figure 2.7: Comparison of backscattering RCS from the metallic vehicle, above a dielectric ground plane with  $\epsilon_r = 5.62 + i 0.94$ , calculated by the hybrid method, inside and outside of the forest for standard polarization configurations of incident plane wave propagating along  $\theta_i = 30^\circ$  and  $\phi_i = 180^\circ$ . (a)  $\sigma_{hh}/\lambda^2$  (b) Angle( $S_{hh}$ ) (c)  $\sigma_{vv}/\lambda^2$  (d) Angle( $S_{vv}$ ) (e)  $\sigma_{hv}/\lambda^2$  (f) Angle( $S_{hv}$ ).

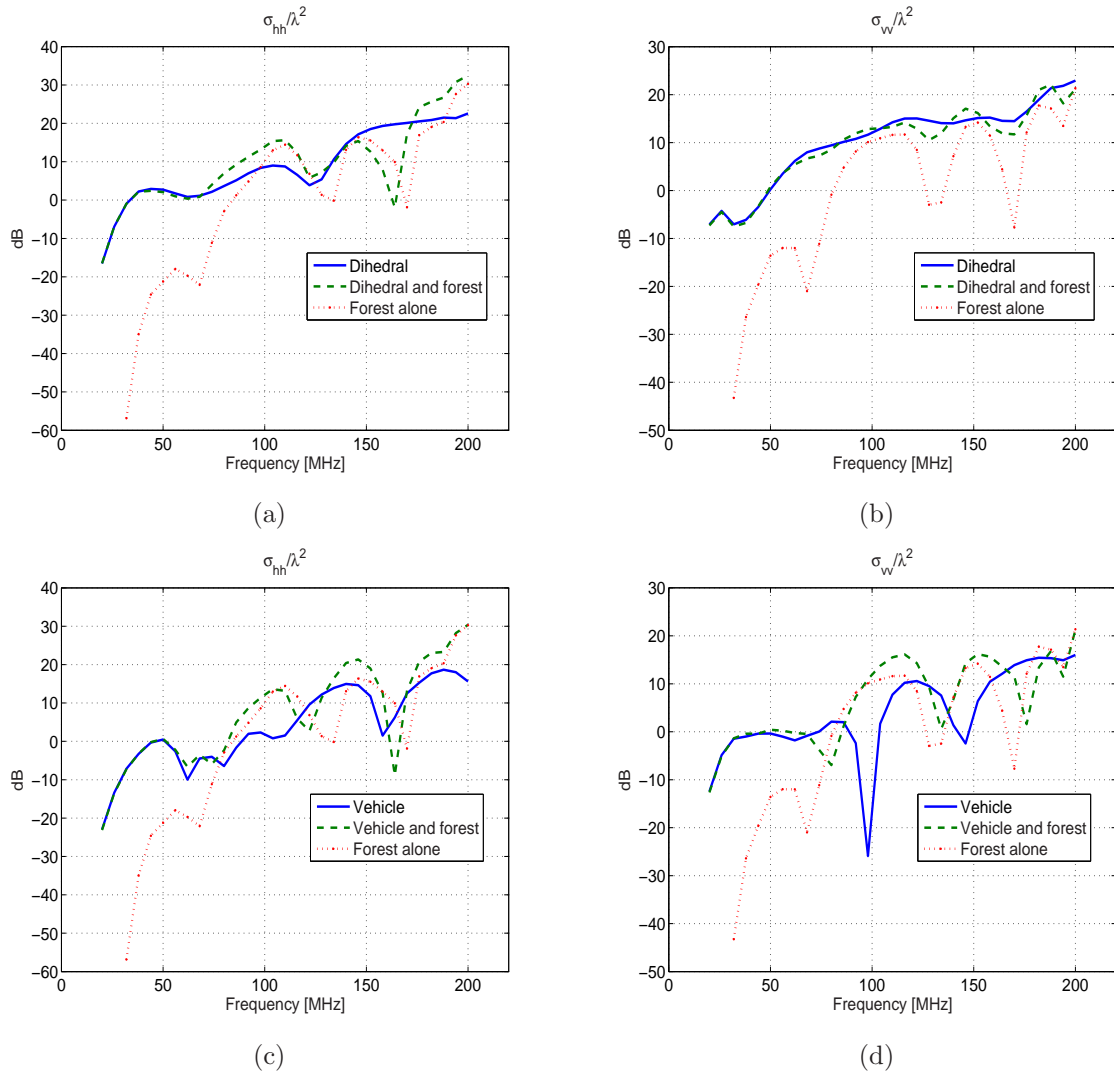


Figure 2.8: Comparison of backscattering RCS from a target, target and forest, and forest alone, for horizontal and vertical polarizations of incident waves propagating along  $\theta_i = 30^\circ$  and  $\phi_i = 180^\circ$ . (a) Dihedral  $\sigma_{hh}/\lambda^2$  (b) Dihedral  $\sigma_{vv}/\lambda^2$  (c) Vehicle  $\sigma_{hh}/\lambda^2$  (d) Vehicle  $\sigma_{vv}/\lambda^2$ .

## CHAPTER 3

# Electromagnetic Scattering from Foliage Camouflaged Complex Targets

In the previous chapter a hybrid target-foliage model is developed to investigate the scattering behavior of hard targets embedded inside a forest canopy at VHF frequency band. In this chapter, a hybrid target-foliage model, based on existing electromagnetic techniques, is developed to investigate the scattering behavior of hard targets embedded inside a forest canopy at higher frequencies (i.e. L-band). The proposed model is composed of two basic scattering models, one for foliage and the other for the hard targets. The connection between these two models, that accounts for the interaction between the foliage scatterers and the target and vice versa, is accomplished through the application of the reciprocity theorem. Wave penetration through the forest canopy and near-field and far-field scattering from the canopy's constituents is calculated using a coherent discrete scattering model which makes use of realistic tree structures. Calculation of scattering from a hard target illuminated by the reduced incident field and the scattered field of nearby vegetation is carried out using an iterative Physical Optics (PO) method formulated for fast computation of foliage target interaction. To reduce the number of iterations, Geometric Optics (GO) approximation is initially used for determining the shadowed areas over the hard target when illuminated by individual foliage scatterers. Also, using a scaled measurement system at millimeter-wave frequency, the accuracy of the iterative PO model is demonstrated, employing a complex target that occupies a volume as big as  $86\lambda \times 33\lambda \times 20\lambda$ .

## 3.1 Introduction

Detection and identification of hard targets camouflaged inside vegetation canopies, are among the most challenging problems in Remote Sensing [70], [71]. Recent advanced capabilities of SAR/INSAR sensors such as multi-frequency, multi-baseline, and multi-polarization features have made a wide range of both civilian and military applications possible. Civilian applications include search and detection of archaeological sites, crashed airplanes in forested environments, and foliage attenuation measurements using trihedrals placed under forest canopies. Military and law enforcement applications include detection and identification of foliage camouflaged vehicles and facilities. To develop effective detection and identification methods for such purposes, the phenomenology of electromagnetic wave interaction with foliage and hard targets embedded in forest canopies must be thoroughly understood. Basically a complete sensitivity study of backscattered fields to different parameters such as different realizations of the forest, different incidence angles, polarizations, and frequencies of the incident field will allow for investigation of applicability of novel detection and identification algorithms, as reported in [12]-[14].

Electromagnetic (EM) scattering from targets inside foliage may be studied using three basic approaches: 1) analytical, 2) exact numerical and 3) experimental/empirical. At very low frequencies, scattering from the forest itself may be rather small and scattering behavior from the hard target is not much different from that of the target without the forest. In this case, the foliage can simply be modeled as layered homogeneous dielectric media with different effective dielectric constants. EM scattering in stratified media can be analytically solved, and as a consequence, closed-form expressions for low-frequency scattering from foliage can simply be obtained.

At microwave frequencies, on the other hand, scattering and attenuation from foliage is rather significant, and its effects on total backscatter and foliage covered target backscatter must be carefully accounted for. For the problem at hand, modeling the forest by randomly distributed particles and solving the problem of scattering from obscured targets inside random media is not sufficiently accurate. It has been observed that backscattering from and attenuation through the forest is significantly affected by the tree structures [45], [18].

Next, exact numerical simulations such as finite difference time domain (FDTD) technique have been suggested for evaluation of scattering from objects inside random media [22] and scattering from forest [23]. The application of brute-force numerical methods is, however, limited to VHF frequencies and lower [23]. At microwave frequencies overall dimensions of a tree are much larger than a wavelength, and therefore, computation of the scattered field from a number of trees and their interaction with the target becomes computationally intractable.

Finally, scattering from targets inside forest can be studied experimentally, using radar systems. Experimental and empirical approaches for phenomenological studies are oftentimes rather limiting, due to the lack of comprehensive data sets and the accompanying ground truth. Such methods are, however, very useful for proof of concept and demonstrations [20]-[21].

In this chapter we propose an accurate EM model for scattering from foliage-camouflaged targets at microwave frequencies that accounts for first order near-field foliage and hard target interactions. This model is constructed from a number of analytic electromagnetic tools assembled in a unique fashion for fast and accurate computation of scattered fields, using well-known electromagnetic theorems. To simplify the problem, the scattering domain is broken into two parts. The first part of the problem is related to the computation of field propagation through and scattering from foliage. The second part of the problem pertains to the characterization of scattering from the target illuminated by the attenuated incident field and the scattered field from all nearby foliage particles. The forest scattering model is based on the coherent scattering model developed previously [18], [19], and the target model is based on high frequency techniques. The connection between these two scattering domains is accomplished using the reciprocity theorem [24],[25]. To avoid brute-force time consuming foliage-target scattering interaction by myriads of vegetation particles around the target, an efficient iterative physical optics approach is implemented [27]-[30]. The main contribution of this chapter is in construction of a comprehensive foliage target model that is computationally tractable. This model accounts for scattering from foliage, hard target, and near-field interaction of foliage and the hard target.

This chapter is organized as follows: An EM scattering model used for estimation of scattering from and propagation through foliage is addressed in Section 3.2. In Section 3.3, a hybrid GO and iterative PO formulation is presented that provides the induced surface current on a hard target excited by the incident wave and scattered fields from all nearby foliage scatterers. In section 3.4, a general formulation based on the reaction theorem is used, which allows for simple calculation of the backscattered field, including first order target foliage interaction. Finally simulation results of camouflaged hard targets are presented in Section 3.5.

## 3.2 Electromagnetic Scattering from Foliage

EM wave scattering from foliage has been investigated intensely through different models [15], [16], and Michigan Microwave Canopy Scattering Model (MIMICS) [17]. For the problem at hand a coherent model capable of maintaining the phase is needed. An accurate model, based on coherent scattering theory has been proposed recently [18], [19]. In this model the vegetation canopy is composed of individual dielectric cylinders and thin dielectric disks, representing tree trunks, branches and leaves respectively, arranged in a semi-deterministic fashion. The simplification is justifiable for tenuous random media composed of lossy scatterers. The single scattering forest model also includes the interaction of the scatterers with the ground plane, which is modeled by a half space dielectric layer. This interaction is accounted for through the application of image theory maintaining only the saddle point contribution. The formulations for calculating the scattering and attenuation caused by vegetation particles are derived analytically using high- and low-frequency techniques [54], [55]. For precise prediction of field behavior inside the canopy, the structure of the trees must be preserved in the forest model. This is done using a fractal-based model (known as Lindenmayer systems), that can generate very complex tree structures with a finite number of structural and botanical parameters.

Field computation must be carried out coherently, to preserve the phase of the scattered fields. Such a model is implemented in [18], where scattering from each tree component, when illuminated by the mean field, is calculated and the total scattering is expressed as

the coherent summation of all the scattering contributions. The mean field is computed using Foldy's approximation, which accounts for the phase change as well as extinction due to the scattering and absorption of the tree particles. The model presented in [18] is valid for scenarios where the observation point is outside in the far-field region of the trees. This model is used to compute the backscattered field from the foliage alone. Recently, a more advanced model was developed [19], in which the observation point can be placed inside the forest, possibly in the near field of some scatterers. Scattering formulations for individual scatterers were modified to achieve a uniform scattering solution for scatterers valid from near-field to far-field regions.

The advantages of this model are: 1) absolute phase response of the field is preserved, 2) the coherent scattering mechanisms are accounted for, 3) tree architecture, which is very important for accurate estimation of field on the target, are taken into account, and 4) near-field scattering from tree constituents have been captured using uniform formulations, valid from near-field to far-field regions. The coherent summation of all scattering contributions, including the reflected waves from the ground plane, is computed to find the total field at a given point within the forest canopy. The total field inside the forest, composed of attenuated incident field, its reflection from the ground, and the near-field and far-field scattering from the forest components, is used as the excitation source for the hard target.

In an experiment study reported in [75], an estimate for the mean value of the one-way foliage attenuation based on 26 sets of measurement is provided which can be used for foliage model validation. Here, we compare the simulated and the measured cumulative distribution functions (CDF) for vertically and horizontally polarized waves. The parameters of the pine tree stand described in [75] are used to generate its fractal model. The tree stand parameters are as follows: tree height is 14 m, crown thickness is 3.9 m, the average diameter at breast height (dbh) is 19.8 cm, the stand tree number density is  $0.23 \text{ trees}/\text{m}^2$  and the tree trunk-main branch angle varies between 40 to 50 degrees.

An observation point is placed at 0.5 m above the ground plane. For 200 Monte Carlo simulations of a sample forest stand consisting of 15 pine trees, randomly located around the observation point, the electric fields along the vertical and horizontal directions are computed. According to the experiment an angle of incidence equal to 40 degrees and

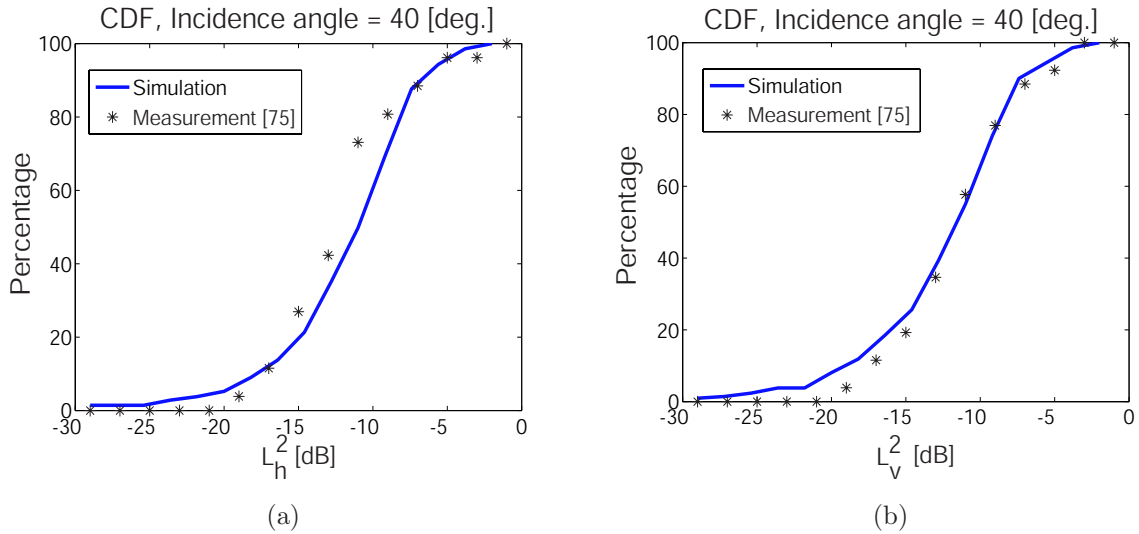


Figure 3.1: Comparison between CDF of the simulated and measured one-way foliage attenuation for (a) horizontal and (b) vertical polarizations.

illumination at 1.6 GHz is chosen. In this simulation the reflected field from the ground has been excluded in order to be consistent with the measurement where the backscatter from a trihedral is used for the computation of two-way attenuation.

Fig. 3.1(a) and (b) compares the simulated and measured data where good agreement is shown. Here  $L_h^2$  and  $L_v^2$  are the horizontal and vertical one-way foliage attenuation respectively. The estimated mean values of the one-way attenuation factors reported in [75] are 9.31 dB for horizontal polarization and 9.16 dB for vertical polarization. These values computed by the simulation are about 9 dB for horizontal polarization and 9.4 dB for vertical polarization. The simulated values are within the precision of the measured data,  $\pm 0.3$  dB [75].

### 3.3 Computation of Induced Surface Current

At very low frequencies, the scattering effect of the forest is rather small, and scattering behavior from the target is not much different from that of the target without the forest. As mentioned earlier, at high frequencies the forest attenuates and distorts the incident wave phase front significantly. The computation of the scattered field from hard targets can

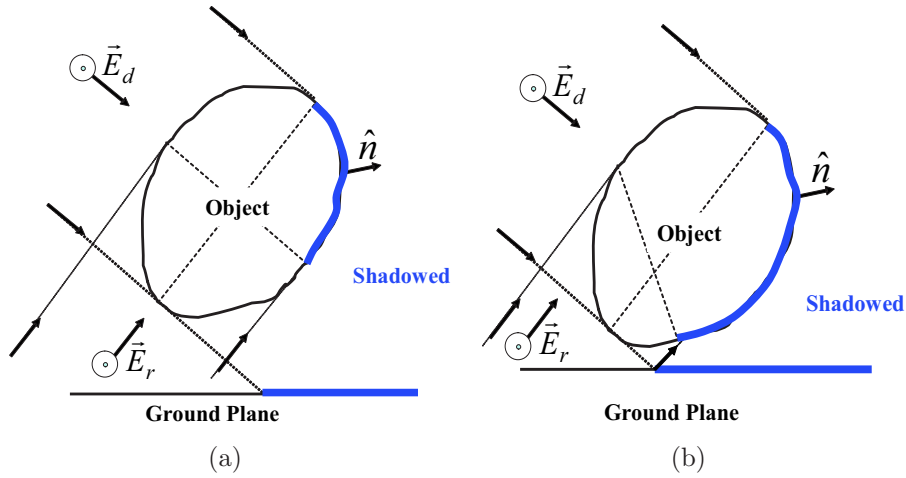


Figure 3.2: Geometry of a smooth convex object and shadowed areas for direct and reflected waves for two different heights of the object above the ground plane.

be pursued in two different ways: 1) exact numerical methods, and 2) approximate analytic approaches [27]-[29]. Although exact numerical techniques can provide very accurate results, their utility is rather limited at high frequencies due to exorbitant computer memory and run times. This is especially true for the problem at hand where the number of sources illuminating the target can be as high as  $10^5$  or more.

Approximate analytic approaches, in turn, can be categorized into two methods: 1) geometric theory of diffraction (GTD), based on ray tracing and computation of diffraction at discontinuities, and 2) physical optics, based on approximating the surface or volumetric currents on the scatterer. Noting that the number of scatterers around the target is very large, ray tracing and GTD are not computationally tractable. This difficulty is exasperated when the interaction of the scattered field from the hard target and nearby forest scatterers are needed as well. On the other hand, having tangential components of the incident fields over the target is sufficient to compute the PO currents. The PO approximation is known to produce valid scattered fields in directions near specular reflections off of scatterers, which tend to dominate other scattering mechanisms. For the problem at hand, we are dealing with a scattering scenario with multitudes of sources around the target. Therefore, for any scattering direction with a very high probability there exists at least one specular reflection. This significantly improves the accuracy of the PO approximation.

A challenging step in establishing the PO currents on a hard target is the determination of the lit and shadowed points on complex target geometries. Again ray tracing from each scatterer to the points on the target to determine whether they are lit or shadowed is a time consuming task. To circumvent this difficulty an iterative PO approach is considered, which can automatically account for shadowing effects. The iterative PO technique, has been shown to be a very efficient high frequency approach for capturing dominant near-field multiple scattering effects (excluding edge effects) from electrically large targets [27]-[74].

In order to calculate the induced surface current on a metallic target embedded in a highly scattering environment, a hybrid method based on PO approximation is used. In this approach, first the forest scattering model is used to find the electric and magnetic fields over the surface of the target. The magnetic field is then employed to calculate the induced surface current using Kirchhoff approximation. This approximation produces accurate results where the local radius of curvature at any point on the surface of the target is large compared to the wavelength. This approximation does not handle diffraction from the edges properly. Due to the existence of many scatterers around the target, the total scattered field from the target will be primarily dominated by the specular scattering contributions. Noting that contributions from edge diffraction are significantly lower than scattering along specular directions.

To treat a complex object with PO approximation, the object is first decomposed into many small flat elementary patches, which have a simple geometry such as a rectangle or triangle. Then, using tangent plane approximation, the current on the lit region of the scatterer is approximated by [69],

$$\bar{J} \approx 2\hat{n} \times \bar{H} = \frac{-2i}{k_o Z_o} \hat{n} \times (\nabla \times \bar{E}) \quad (3.1)$$

where  $\bar{E}$  and  $\bar{H}$  are the incident electric and magnetic fields on the object, respectively and  $\hat{n}$  is the local normal unit vector as shown in Fig. 3.2. One difficulty encountered in determining the PO current of the target is identification of lit and shadowed facets. Another issue with the shadowing is the absence of the reflected rays from the ground because of the hard target itself. As shown in Fig. 3.2 (a) and (b), the shadowed area on the target is

a function of the target height above the ground. In what follows, procedures for dealing efficiently with the shadowing problem are introduced.

### Simple Convex Object

Determination of lit and shadowed regions for convex objects is rather simple. Denoting the incidence direction from any scatterer in the forest to a point on the hard target or the direct incident wave by  $\hat{k}_d$ , the point is considered lit, if  $\hat{n} \cdot \hat{k}_d < 0$ , and shadowed, if  $\hat{n} \cdot \hat{k}_d > 0$ , as shown in Fig. 3.2. Here  $\hat{n}$  denotes the outward normal unit vector of the target surface. Due to the presence of the ground plane for every incident wave on the target, a reflected ray from the ground plane also exists. Denoting the direction of the reflected ray corresponding to  $\hat{k}_d$ , by  $\hat{k}_r = \hat{k}_d - 2(\hat{z} \cdot \hat{k}_d)\hat{z}$ , the lit and shadowed points can also be easily identified for the reflected rays. Generally the blockage of the reflected rays by the target can be considered by ray tracing. To simplify this step, it is noted that for most practical problems, the target is sitting on the ground plane, and hence, the area directly underneath the target cannot produce reflected waves. This is important, since the total field on the target is composed of two mean-fields (direct and reflected) plus four scattering terms from each scatterer. In situations where the ground reflection point happens to be just under the target, its contribution to the total field must be excluded. This is accomplished by placing a perfectly absorbing layer on the ground over the area where the target sits [76].

### Complex Hard Target

As shown in the previous section, for simple convex objects, a Geometrical Optics (GO) approach can be used to find the lit and shadowed areas on the object, and PO can be used to find the surface electric current. This method henceforth will be referred to as the GOPO approach. However, this approach is not computationally efficient for targets with complex geometries, particularly when we consider the large number of illuminating sources around the target. For example, in a brute force approach for a target with  $N_f$  discretized facets, the computation time for determining the lit or shadowed facets is proportional to  $N_f^2$  for a single direction of incidence. Considering  $N_s$  scatterers around the target, the total computation time is proportional to  $2 N_s N_f^2$ . The factor 2 here accounts for the fact

that there exists an image for every scatterer in the ground plane. In addition, the GOPO accuracy for calculation of the radar cross section (RCS) may not be sufficient when near-field multiple bounces on the target itself are significant and/or typical dimensions of the scatterer become comparable with the wavelength [77]. For example, adjacent perpendicular facets on the target can form a dihedral, which can produce significant backscatter. Such contributions are not captured by a first-order PO approximation. A glance at the geometry of a typical target, shown in Fig.3.4(a), reveals the existence of such facets on the target.

To demonstrate this point, two simple objects such as two perfectly conducting boxes are considered (see Fig. 3.3). The induced surface current density on each point of the object can be calculated from the Magnetic Field Integral Equation (MFIE) [77]:

$$\bar{J} = 2\hat{n} \times \bar{H}_i + 2\hat{n} \times L[\bar{J}] \quad (3.2)$$

where the operator  $L[.]$  is,

$$L[\bar{J}] = \int_{surface} (\bar{r} - \bar{r}') \times \bar{J}(r') \left( ik_0 - \frac{1}{|\bar{r} - \bar{r}'|} \right) \frac{e^{ik_0|\bar{r} - \bar{r}'|}}{4\pi|\bar{r} - \bar{r}'|^2} d\bar{r}' \quad (3.3)$$

Near-field interaction of the surface currents on a target is responsible for certain scattering phenomena such as double-bounce scattering, in dihedral, or triple-bounce scattering in corner-reflector. In fact, shadowing phenomenon can also be attributed to near-field interaction of surface currents. The current on the lit region produces a scattered field in the forward direction that is almost equal and out of phase with the incident wave. Hence, the sum of the scattered field and incident field over the shadowed region almost cancel each other, giving rise to a very small field there. The non-zero but small field in shadowed areas can be attributed to diffracted fields from the edges, and shadow boundary [78]. This suggests that keeping track of multiple scattering can take care of shadowing problems automatically. In addition, effects of multiple scattering can be readily accounted for by an iterative PO approach.

Iterative PO has been used in the past to better estimate induced surface currents near shadow boundaries for convex objects [27], [28] or account for near-field multiple scattering for concave objects [29]-[73], and [77]. Here we use this approach to find shadow areas and

capture higher order near-field scattering from complex targets embedded inside the foliage.

The starting point for the iterative PO solution is the MFIE given by (3.3). To the first order approximation we have  $\bar{J}^{(1)} = 2\hat{n} \times \bar{H}_i$ , which is the PO current. However, this approximation does not formally recognize the lit and shadowed areas. Instead of identifying the exact boundaries of the lit and shadowed areas over a complex target, a simple condition is used to find the primary shadowed areas first, and through a PO iteration all shadowed areas are determined automatically. This procedure expedites the convergence of the iterative PO algorithm [73]. When calculating the field on the target for every source point, a primary shadowing condition given by  $\hat{k} \cdot \hat{n} < 0$  is examined. Here  $\hat{k}$  is a unit vector from the source to the point on the surface. Of course, for complex objects, there are shadowed points (in concave regions) where  $\hat{k} \cdot \hat{n} < 0$ , but correct shadowing is achieved through iteration of the PO currents. Carrying on the iteration process, the same approach is taken for capturing the effect of higher order currents. That is, in computation of (3.3), only the contribution of the points where,

$$(\bar{r} - \bar{r}') \cdot \hat{n} < 0 \quad (3.4)$$

is considered. In fact equation (3.4), referred to as the shadowing rule, has been used in iterative PO approximations to find for example scattering from cavity structures [73]. Therefore, the second order PO current given by

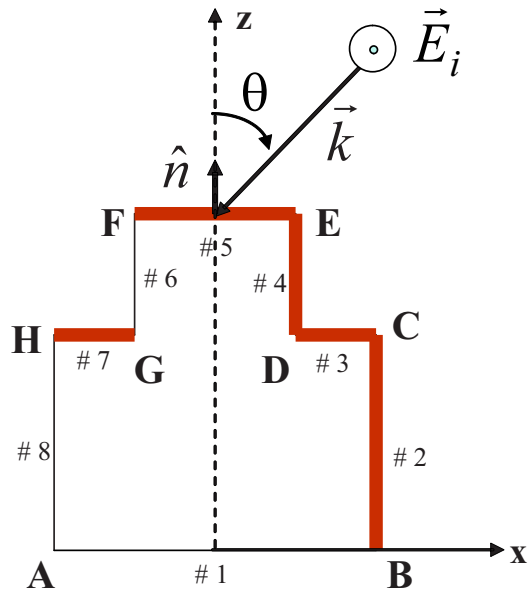
$$J^{(2)} = 2\hat{n} \times L[J^{(1)}] \quad (3.5)$$

will not only provide the double-bounce scattering over the lit region but also remove the first order currents erroneously put over concave shadowed areas. Higher order currents can also be obtained in a similar manner, i.e.  $J^{(m)} = 2\hat{n} \times L[J^{(m-1)}]$ . For most practical applications iteration up to the second order is sufficient. This second order PO approach will be referred to as Hybrid GOPOPO method.

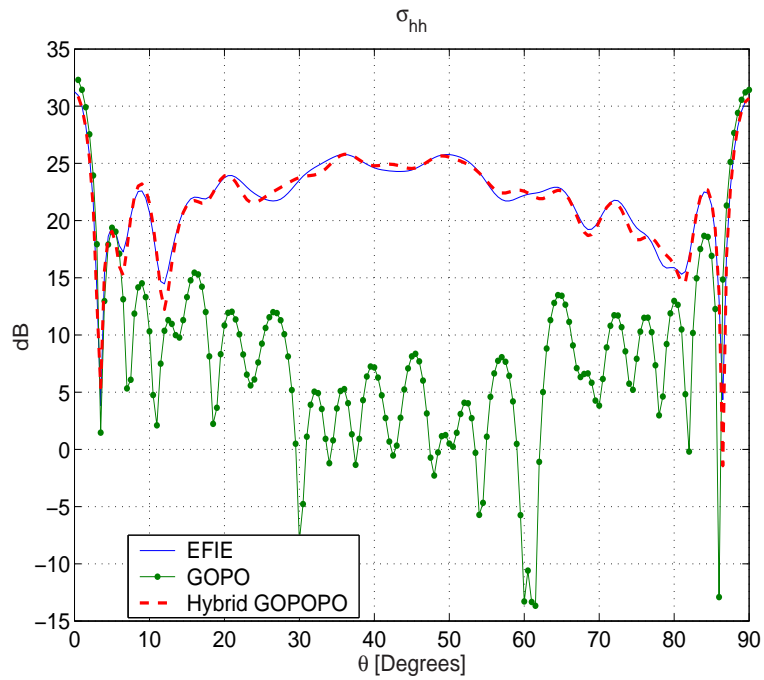
The iterative GOPOPO method in [77] proposes a ray tracing approach (GO approximation) at its first step (first bounce), to determine the illuminated parts of each panel of a trihedral corner reflector. This is because the incident field is a plane wave (the target is in the far-field of the source). This approach improves computation time as well as accuracy

of the results, because it does not go through numerical computation of MFIE integral at the first step. However as mentioned before, due to the large number of sources around the desired target, determination of the illuminated areas for each source is not practically tractable.

To demonstrate this algorithm and its accuracy, let us consider the scatterer shown in Fig. 3.3(a). For a plane wave incidence, on facets # 2, # 3, # 4, # 5, and # 7 for which  $\hat{n} \cdot \hat{k} < 0$ , the first order PO currents are placed initially. This is despite the fact that facet # 7 is partially or totally shadowed by facet # 5. The iterative PO, should capture the double-bounce scattering mechanisms between facets # 4 and # 3, and correctly predict the shadowing of # 7 by facet # 5. To verify the proposed hybrid GOPOPO method, the backscatter of a PEC body shown in Fig. 3.3 (a), with dimensions  $AB = 8\lambda$ ,  $BC = 4\lambda$ ,  $CD = GH = 2.5\lambda$  and  $DE = EF = 3\lambda$ , and a length of  $10\lambda$  along the  $\hat{y}$  direction, at frequency of 2 GHz is compared with the backscatter RCS obtained from a method of moments (MoM), using an electric field integral equation (EFIE) formulation. The comparison is demonstrated in Fig. 3.3 (b), for a TE polarized wave where very good agreement is shown. The discrepancies can be associated with the sharp edges of the object.



(a)



(b)

Figure 3.3: (a) Geometry of a simple metallic target. (b) Comparison of backscattering RCS calculated by exact EFIE method, the proposed hybrid GOPOPO method, and a first-order PO approximation (GOPO) for an H-polarized incident plane wave.

This method was also applied to a complex object such as a surrogate tank whose geometry is shown in Fig. 3.4(a). The target is first discretized into a triangular mesh whose sides are smaller than  $\lambda/2$ . For 2 GHz simulation, such a process renders 325,300 triangular facets on the target. The electric current distributions over the entire tank and over the hull are shown in Figs. 3.4 (b), and (c) for a horizontally polarized plane-wave illumination, propagating along  $\theta_i = 30^\circ$  and  $\phi_i = 180^\circ$ . The shadowed area on the top of the hull is generated by the turret roof and the gun, which is successfully predicted by the Hybrid GOPOPO method.

It should be noted that there are advantages and disadvantages associated with iterative PO approach. The advantages of the method are 1) in comparison with full-wave analysis approaches such as MoM, there is no need to store or invert a very large matrix, and 2) since it is based on high frequency approximations much sparse discretization is needed [30], and 3) depending on the structure of the target, the shadowing rule (3.4) can significantly reduce the number of required computations ( $\propto N_f^2$ ). For example, for the structure shown in Fig.3.3(a), where only the double bounce scattering is dominant in the backscatter direction, the computation time is proportional to  $0.11N_f^2$ , where  $N_f = 10,182$ . The main disadvantage of the iterative approach is that it may have a poor convergence, depending on the structure (the number of important reflections) and observation angles. Basically, for hard targets which have relatively deep concave parts, such as cavity structures, iterations may proceed to a large number and for grazing angles to the aperture of the concave section it may not even provide accurate results [30], [73]. However for the type of structures at hand, noting that the target is being illuminated by myriads of nearby scatterers it is expected that the iterative PO will provide satisfactory results.

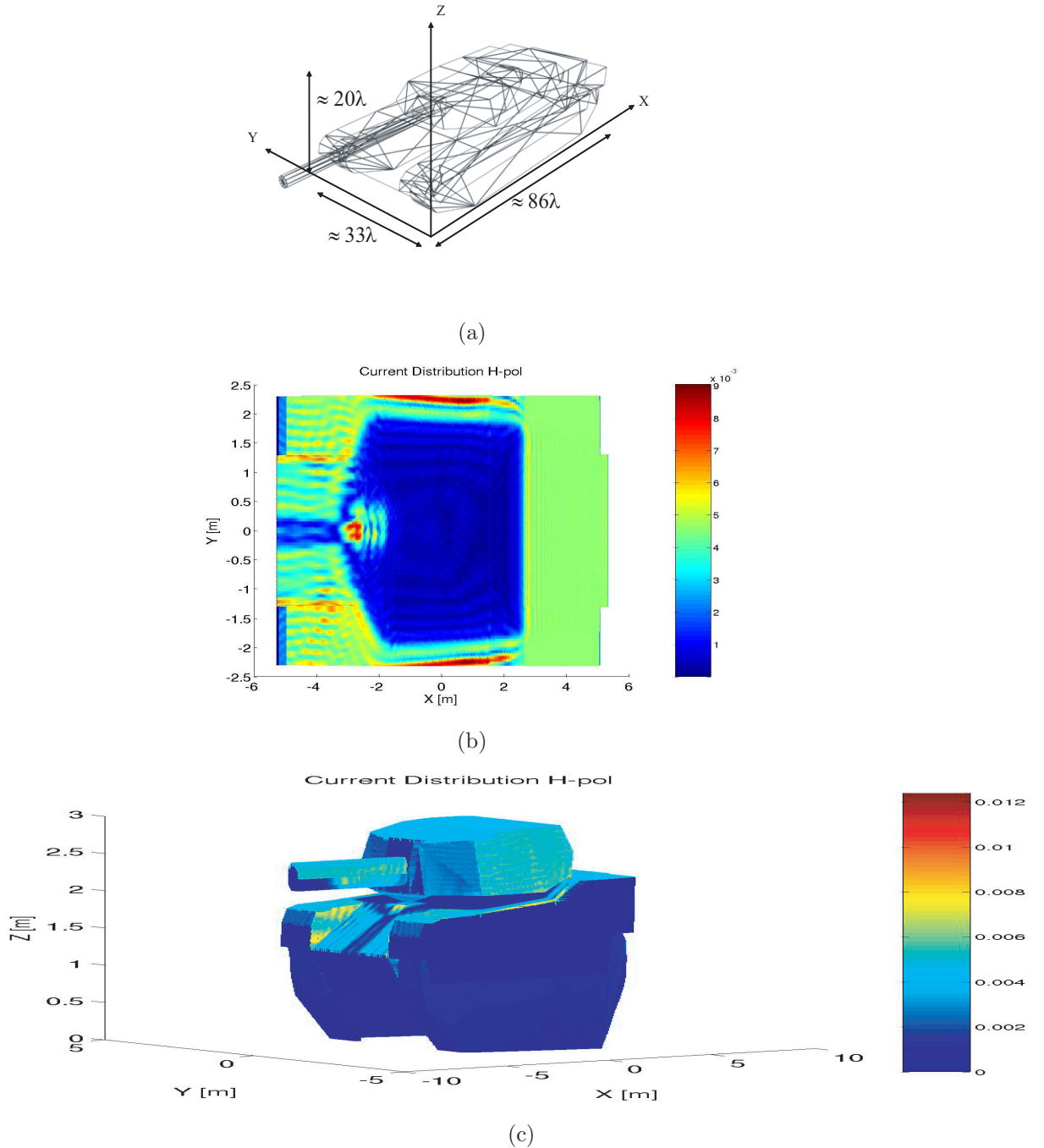


Figure 3.4: (a) Structure and approximate dimensions of a simplified tank, used for simulation at  $f = 2 \text{ GHz}$ . (b) The electric current distribution over the hull of the tank with the turret removed and (c) the current distribution over the entire structure for an H-polarized incident wave in the direction of  $\theta_i = 30^\circ$  and  $\phi_i = 180^\circ$ .

### 3.3.1 Model Validation

In order to validate the simulated backscattering RCS of the tank, a scaled backscatter measurement at W-band frequencies is carried out. In this experiment, the University of Michigan's fully polarimetric W-band radar system, operating over the frequency range of  $93 - 94 \text{ GHz}$ , in a stepped-frequency mode, is used. A scaling factor of  $s = 93.5/2 = 46.75$  is used to compare the measurements at  $93.5 \text{ GHz}$  with the simulation results at  $2 \text{ GHz}$ . A precise three dimensional printer is used to make the scaled tank model with an accuracy of a small fraction of a millimeter. The 3-D printer uses plaster as the building material, hence, metallic tapes are used to cover the structure. The fabricated prototype tank is shown in Fig. 3.5 (a). The radar, used for measurement, is a coherent-on-receive system [79]. The receiver branch of the radar system has a dual polarized antenna capable of measuring simultaneously the magnitudes and phases of both the vertical and horizontal polarizations of the scattered field. The transmitter is a single port antenna that can transmit any arbitrary polarization. System distortion parameters can be measured using two calibration targets [79], namely, a calibration sphere and any depolarizing target, such as a  $45^\circ$  tilted cylinder. Knowing the distortion parameters, the scattering matrix from any unknown target can be accurately measured.

In order to verify the accuracy of the measurements, the RCS of a flat plate with dimension  $20.3 \text{ cm} \times 9.5 \text{ cm}$  is measured. In these measurements an elaborate set up for target and radar alignment is needed. Basically, the RCS of the targets which are composed of electrically large flat plates are very sensitive to the azimuth and elevation orientation angle errors ( $\delta\theta$  and  $\delta\phi$ , shown in Fig. 3.5 (b)). Figure 3.6 (a) presents the comparison between the measured and simulated backscatter from the flat plate where good agreement is shown. In addition, experiments have been repeated to ensure the repeatability of the measurements.

Fig. 3.6 (b) shows a comparison between the measured and the simulated backscattered RCS of the tank, using the proposed iterative PO approach, for a vertical polarized incident wave at  $\phi_i = 180^\circ$  and different values of  $\theta_i$ . As shown, the iterative PO very closely follows the trend of the measured RCS. The discrepancies in the measured and simulated RCS values are typical of very large targets (in this case  $86\lambda \times 33\lambda \times 20\lambda$ ). Sources of the errors

include: 1) target alignment with respect to the radar coordinate system (there are 3 degrees of freedom), 2) fabrication errors caused by shrinkage and warpage, and 3) errors caused by placement of metallic tapes and the seams. The effect of discretization is also examined by reducing the pixel area by a factor of 2.25, and no difference in the simulated results were noticed. The backscattered field from the tank target shown in Fig. 3.6(b) is provided for 90 elevation angles and 3 iterations per angle and computed using 16 AMD Athlon processors with 2 GHz CPU and 1 GB RAM. The approximate time for each iteration is about 18 hours.

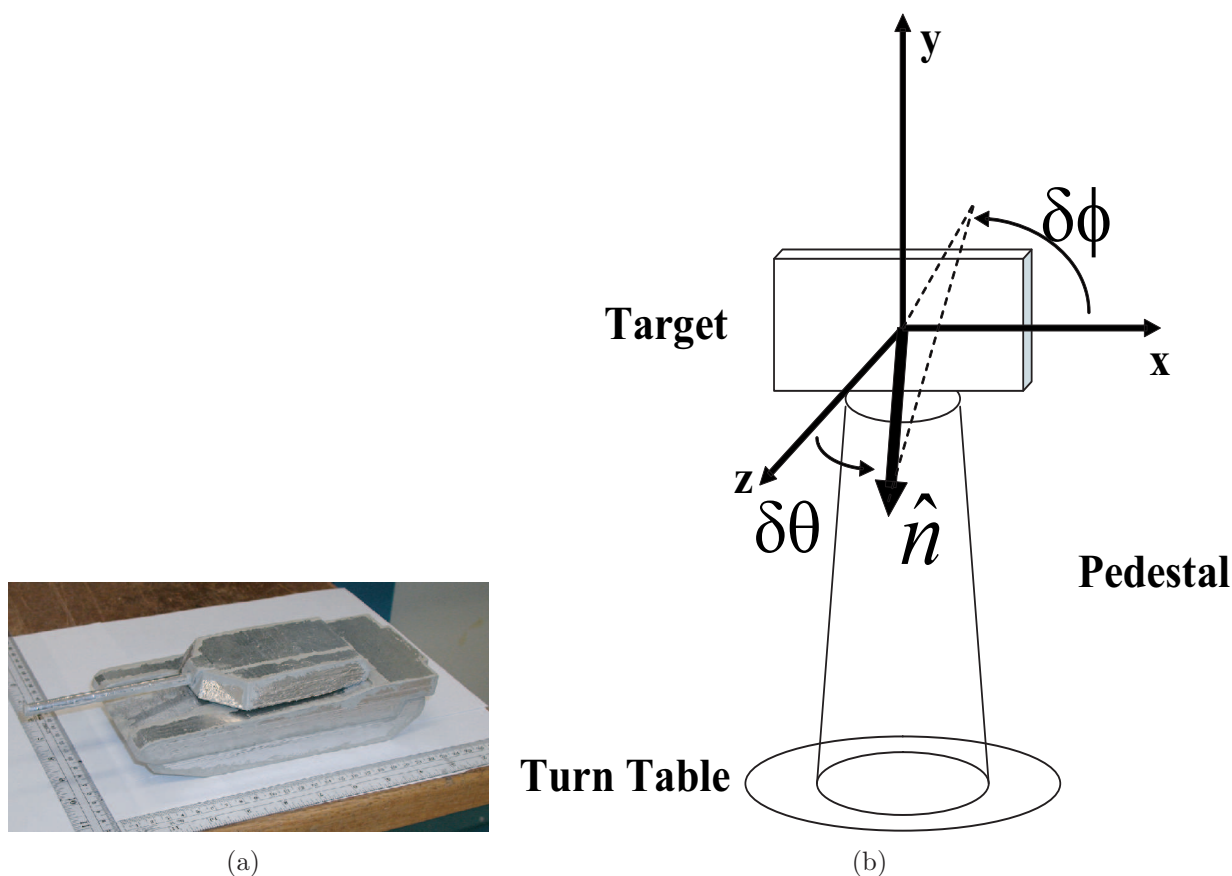
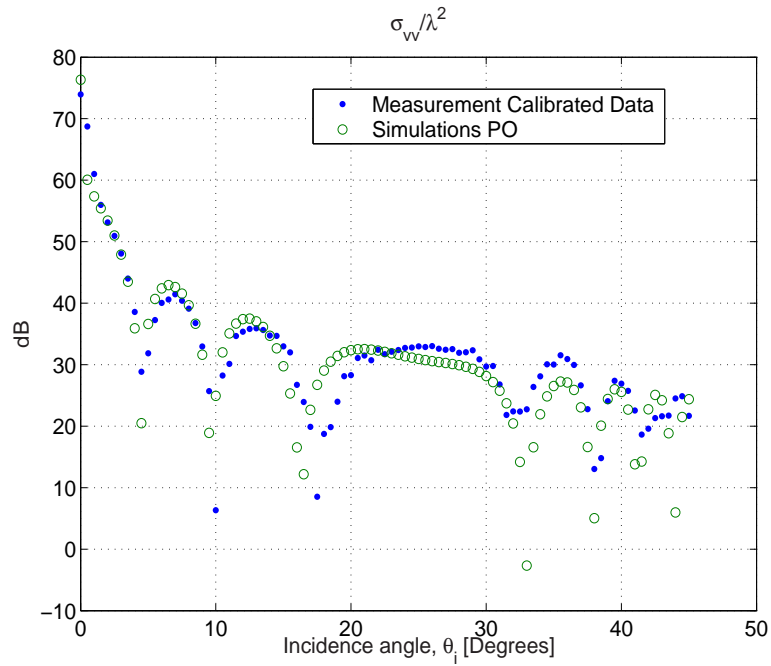
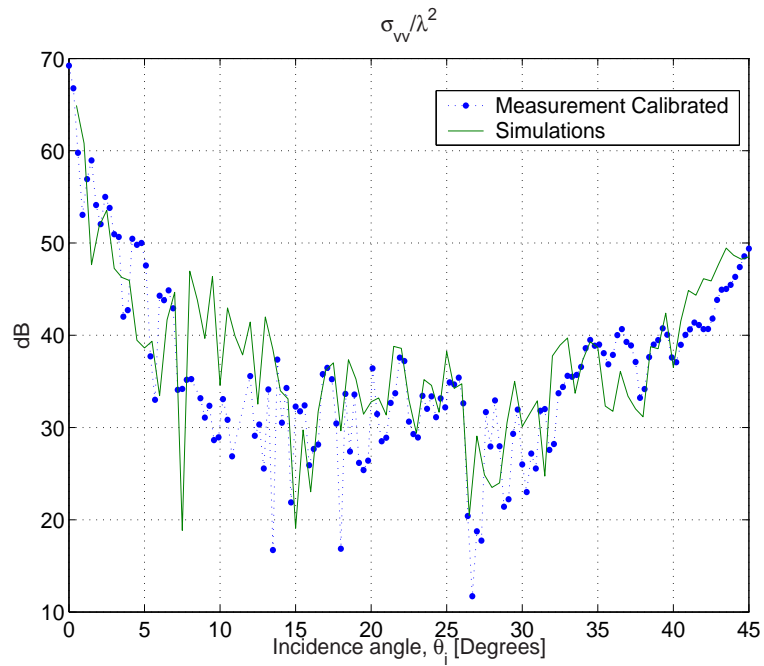


Figure 3.5: (a) A scaled model for a surrogate tank, used for backscatter measurements, over the frequency range of 93 – 94 GHz. (b) Styrofoam target mount over a turntable for backscatter measurement. Here  $\hat{n}$  is the normal to the plate and  $\delta\theta$  and  $\delta\phi$  denote target orientation errors.



(a)



(b)

Figure 3.6: (a) Comparison of the backscattering RCS values between the measured and simulation results for (a) a rectangular PEC plate ( $20.3 \text{ cm} \times 9.5 \text{ cm}$ ) and (b) the scaled tank, at  $\phi_i = 180^\circ$  and different elevation incident angles of  $\theta_i$ , and for vertically polarized incident field.

### 3.4 Computation of Hard Target-Foliage Interaction

The radar backscatter or bistatic scatter field may be decomposed into three basic components. One component of the scattered field emanates from the foliage directly. The second component can be viewed as the direct scattering from the target simply attenuated by the foliage above. This component retains the original signature of the target. Finally the third component is composed of the scattered field interaction between the foliage and the target as well as the target and the foliage. In the previous section the procedure for computation of surface currents on the hard target that includes the effect of scattering from nearby foliage was outlined. To compute the backscatter from the target directly, the dyadic Green's function in the presence of the trees is needed. Noting that the tree components are in the near-field region of the target, computation of the Green's function is very complex and time consuming. In order to simplify the calculation of the backscattered field from the target, inside the forest canopy, and account for the first order target foliage interaction, the reciprocity theorem is used.

Reciprocity theorem has been used in past to account for first order scattering interaction [24], near-field to far-field transition [25]. In this approach, the induced currents and the total incident wave on the target, which are already computed, are needed to formulate the backscattered field. This way, foliage-target as well as target-foliage interactions can be accounted for simultaneously. According to the reaction theorem applied to a linear system composed of two sets of sources and fields, denoted by 1 and 2, we have [69]

$$\langle 1, 2 \rangle = \langle 2, 1 \rangle \quad (3.6)$$

where, for example  $\langle 2, 1 \rangle$  denotes a surface or volume integral of the reaction of source 1, with the fields radiated from source 2 at the location of source 1.

For our problem, the incident field on the target is composed of the superposition of scattered fields from all tree constituents such as branches, trunks, and leaves, and the direct field attenuated by the foliage (mean field). Each of these field components can be decomposed into a direct and a reflected field from the ground plane. Mathematically, this

can be expressed as

$$\bar{E}_1 = (\bar{E}_d + \bar{E}_r)_{mean} + \sum_{Scatterers} (\bar{E}_d + \bar{E}_r) \quad (3.7)$$

where the subscripts  $d$  and  $r$  stand for the direct and reflected fields, respectively. Accordingly, the induced currents on the target, designated here as the second source, can be written as

$$\bar{J}_2 = (\bar{J}_d + \bar{J}_r)_{mean} + \sum_{Scatterers} (\bar{J}_d + \bar{J}_r) \quad (3.8)$$

Considering an elementary electric current source, located at the point (radar position)  $\bar{r}_R$ , oriented along  $-\hat{p}$  and having a magnitude given by

$$\bar{J}_1 = \frac{4\pi}{ik_o Z_o} \frac{r_R}{e^{ik_o r_R}} \delta(\bar{r} - \bar{r}_R) (-\hat{p}) \quad (3.9)$$

the backscattered field  $\bar{E}_2$  can be easily achieved [24]. Here  $k_o$  and  $Z_o$  are the propagation constant and characteristic impedance of the free space, respectively. Since the target is assumed to be a perfect electric conductor (PEC), magnetic current is not considered. The unit vector  $\hat{p}$  can be along  $\hat{h}_i$  or  $\hat{v}_i$ , respectively for horizontal or vertical polarization of the incident field, defined in a global coordinate system according to

$$\hat{h}_i = \frac{\hat{k}_i \times \hat{z}}{|\hat{k}_i \times \hat{z}|}, \quad \hat{v}_i = \hat{h}_i \times \hat{k}_i \quad (3.10)$$

where  $\hat{k}_i$  is the propagation unit vector of the incident field. With these assumptions, it can be shown that using (3.6), each component of the scattered field is expressed by

$$\mathbf{S}_{pq} = \pm \frac{ik_o Z_o}{4\pi} \int_{surface} \bar{E}_{1p} \cdot \bar{J}_{2q} ds' \quad (3.11)$$

where subscript  $p$  and  $q$  can be  $h$  or  $v$  for horizontal and vertical polarizations. The first and second subscripts denote the receive and the transmit polarizations, respectively. Since for the backscattered field  $\hat{k}_s = -\hat{k}_i$ , we have  $\hat{h}_s = -\hat{h}_i$  and  $\hat{v}_s = \hat{v}_i$ , therefore the minus sign in (4.1) is chosen when  $p$  is vertical polarization.

Since both  $\bar{E}_1$  and  $\bar{J}_2$  are computed in the presence of the foliage around the target, the backscattered field computed from (4.1) also includes the interaction of target scattered fields with the foliage. It should be emphasized that the formulation given by (4.1) only accounts for the first-order scattering interaction between the hard target and foliage (and vice versa). Since in practice there are sufficient separations between the hard target and foliage, first-order scattering captures most significant scattering interactions. This approach significantly simplifies backscatter field computation. Finally, RCS of the target can be calculated from,

$$\sigma_{pq}^s = 4\pi |\mathbf{S}_{pq}|^2 \quad (3.12)$$

### 3.5 Simulation of Hard Targets Embedded in Foliage

To examine the importance of foliage in modifying the RCS values and RCS signature of foliage camouflaged targets, simulation of backscatter responses of simple targets in a pine forest is examined. First, we consider a  $3\lambda \times 3\lambda$ , horizontal metallic plate placed 1 m above a lossy ground plane. For this simulation, relative permittivity of the ground plane is set to  $\epsilon_r = 5.6 + i0.8$ , and the frequency of incident plane wave is chosen to be  $f = 2$  GHz. For calculating PO currents, the plate is meshed into 144 segments of  $\lambda/4 \times \lambda/4$  square elementary patches over which the fields and the electric currents are considered constant. The backscatter RCS of the plate in the absence of forest using the reciprocity formula given by (4.1) is first compared with a closed-form PO expression [80]. In spite of small discrepancies, caused by discretization, excellent agreement is achieved for all incidence angles. Then a complete simulation, including 10 pine trees with density of  $0.05$  trees/ $m^2$  randomly located around the plate, is considered. Pine trees are generated by the statistical L-system having an average height of  $15$  m, crown radius of  $3$  m, crown height of  $10$  m, trunk radius of  $10$  cm, and more than 5000 scatterers per tree.

Figures 3.7 (a) and (c) show the plot of RCS of the plate alone inside the forest, as a function of azimuth and elevation incident angles in steps of  $0.5$  degrees for each angle. Strong fluctuation of RCS over a small angular range is indicative of significant foliage target interaction. It is also interesting to observe that RCS variations along the elevation angle

are more than those along the azimuth angle. In order to investigate the sensitivity of backscattered RCS from the plate to the tree arrangement, 10 independent realizations of the pine forest are considered, and RCS values of the plate are computed. Figures 3.7 (b) and (d) show the statistical behavior of the backscatter RCS from the plate alone, at  $\phi_i = 180^\circ$  and for different elevation angles. The limits for the I-bars are the maximum and minimum RCS values observed in the realizations. As it appears, the attenuation and scattering from the forest particles reduce the average RCS and perturb the RCS pattern significantly. Constructive and destructive interferences result in substantial RCS fluctuations.

Similarly, Figs. 3.8 (a) and (c) show the RCS of the forest alone, for different elevation and azimuth angles. It is observed that the average level of the backscattered signal from the forest as well as fluctuation along the incident angles, are higher than that of the plate. As shown in Figs. 3.8 (b) and (d), the backscattering coefficient of the forest is almost constant over the angular range of incidence angle. The backscattering coefficient for vertical polarization ( $\sigma_{vv}^o$ ) is about 5 dB less than that of horizontal polarization ( $\sigma_{hh}^o$ ). This is caused by the reduction in the RCS of the ground-trunk component for vertical polarization due to the Brewster angle effect on tree trunks. In conclusion, changing the elevation or azimuthal incident angles or realization of the trees around the target have similar effects in changing the RCS of the plate. These simulations clearly indicate that simply modeling a forest by an attenuation layer fails to predict such strong RCS fluctuations, caused by the interaction of foliage with the target and vice versa.

Figures 3.9 (a) and (b) compare the backscatter from a metallic structure, shown in Fig. 3.3 (a), having dimensions of  $AB = 8\lambda$ ,  $BC = 4\lambda$ ,  $CD = GH = 2.5\lambda$  and  $DE = EF = 3\lambda$ , and length of  $5\lambda$  along the  $\hat{y}$  direction, placed above a lossy dielectric ground plane, as a function of the incident angle  $\theta_i$ , at  $\phi_i = 180^\circ$ , for one realization of the pine forest. Frequency of operation is set to 2 GHz. Due to the presence of tree trunks, in forward scattering, a horizontally polarized wave has more penetration through the foliage, than the vertically polarized wave. Therefore, as shown in Fig. 3.9, it is observed that the average target RCS at horizontal polarization is higher than that at vertical polarization. Figures 3.10 (a) and (b) compare the backscatter from the metallic tank, shown in Fig. 3.4 (a). In this simulation the scattering effect of two adjacent trees, located at (7,0) and (-7,3), are taken into account.

It is observed that this hybrid target-foliage model is capable of simulating a large domain of computations. The run time is basically determined by the number of discretized facets, structure of the target, the number of included trees (scatterers) around the target, frequency of operation and the processors' features. In addition the run time would increase if the fields or currents on the target are intended for storage. In fact simulations provided in this chapter are run by PC and more complicated and larger targets can be simulated using parallel computers. Table I shows the estimated run time of simulations provided in this work for each realization of forest and each incidence angle. It should be noted that for simulation of the plate, shown in Fig. 3.7, 169 different angles and for each angle 10 different realizations of the forest have been considered.

Comparing the forest backscatter, obtained from  $\sigma^o$ , shown in Fig. 3.8 multiplied by the radar footprint or pixel area, with that of the target shown in Fig.3.9, the signal-to-clutter ratio may be a small quantity depending upon the pixel area. To enhance the signal-to-clutter ratio, the polarization signature of the target and the clutter can be studied to discriminate the target backscatter response from that of the clutter.

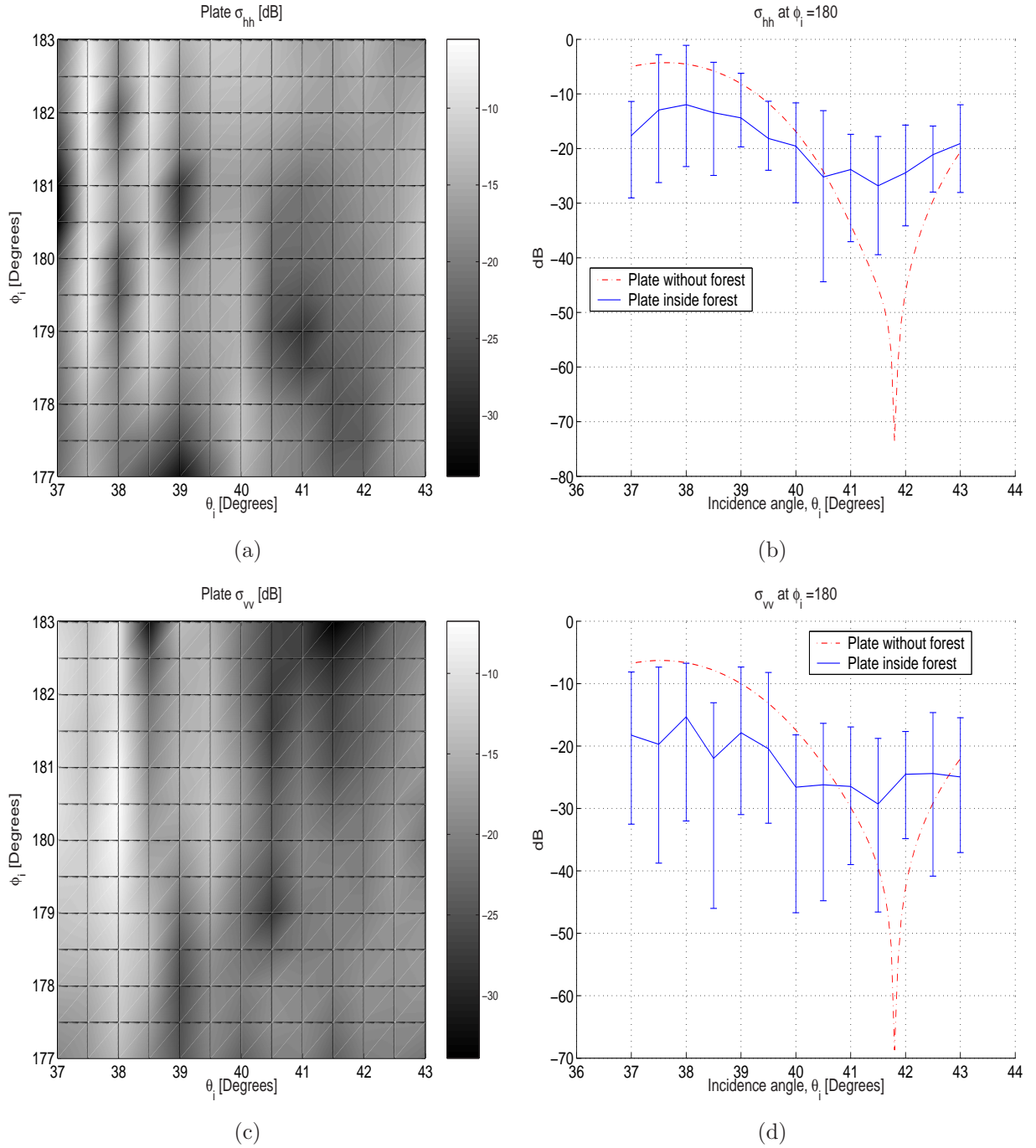


Figure 3.7: Calculated RCS of a  $3\lambda \times 3\lambda$  metallic plate, over a lossy half space embedded inside a pine forest canopy as a function of elevation and azimuth angles (a)  $\sigma_{hh}$  and (c)  $\sigma_{vv}$  at  $2\text{ GHz}$ . Also shown the backscatter from the plate with and without foliage at  $\phi_i = 180^\circ$  and for different elevation angles. I-bar on the mean value shows the fluctuation range of the backscattering cross section for 10 Monte Carlo simulations, (b)  $\sigma_{hh}$  and (d)  $\sigma_{vv}$ .

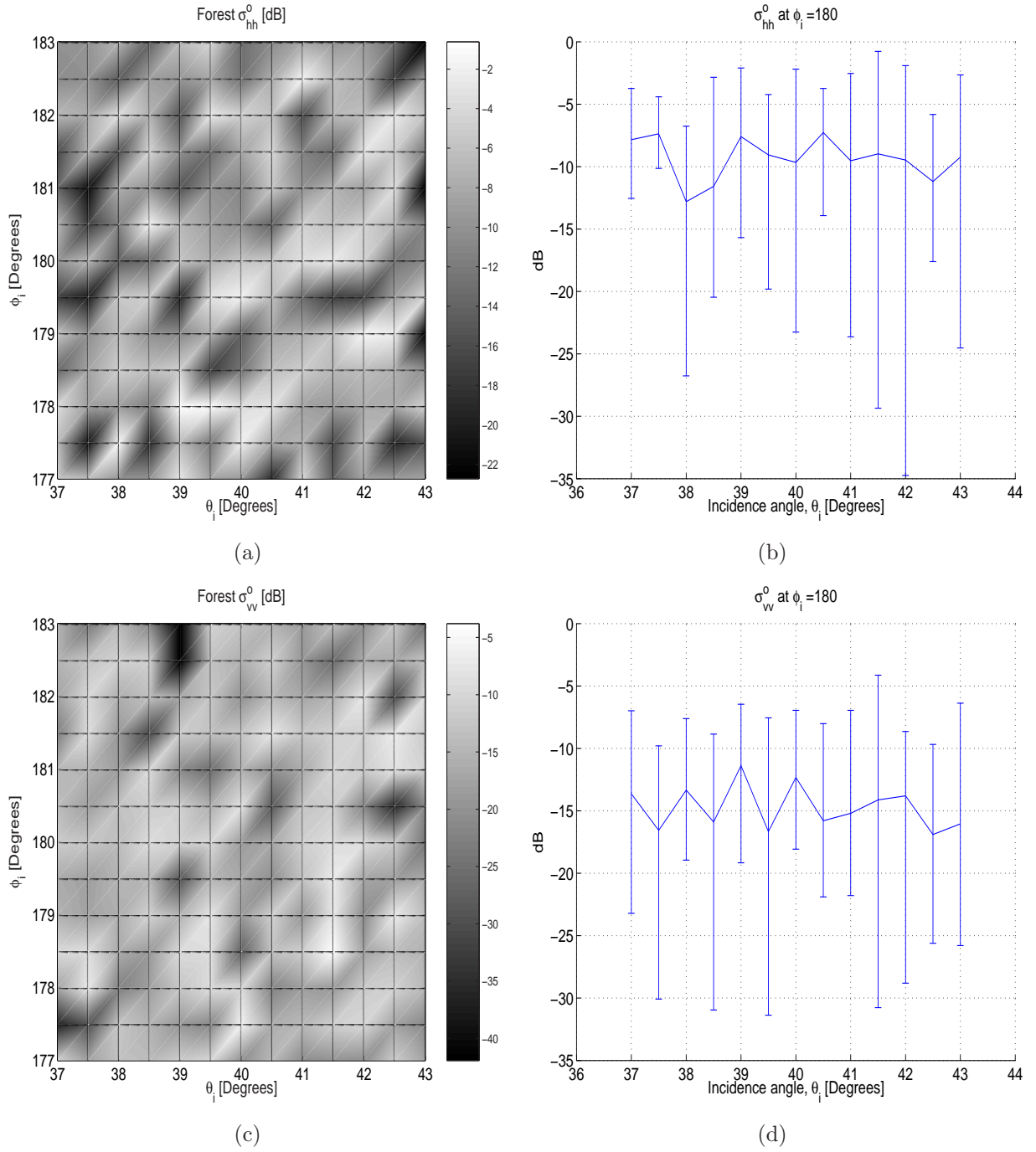
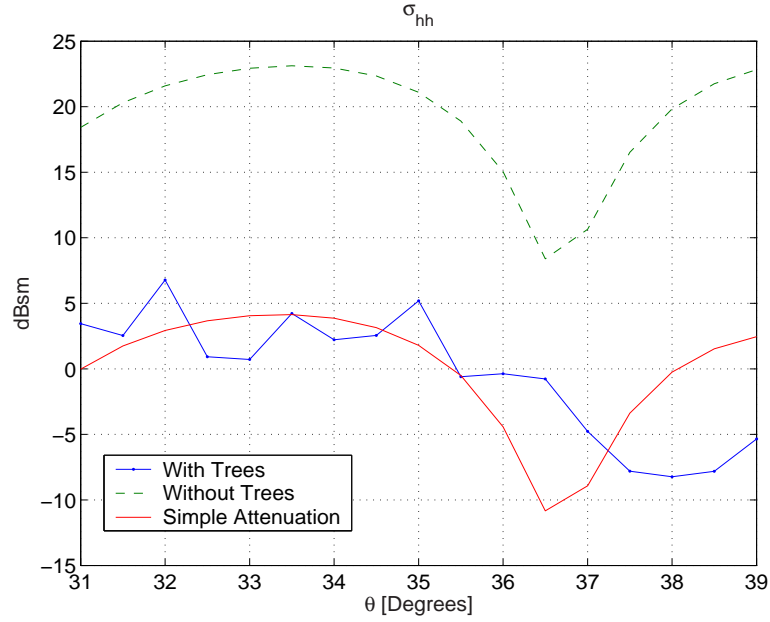
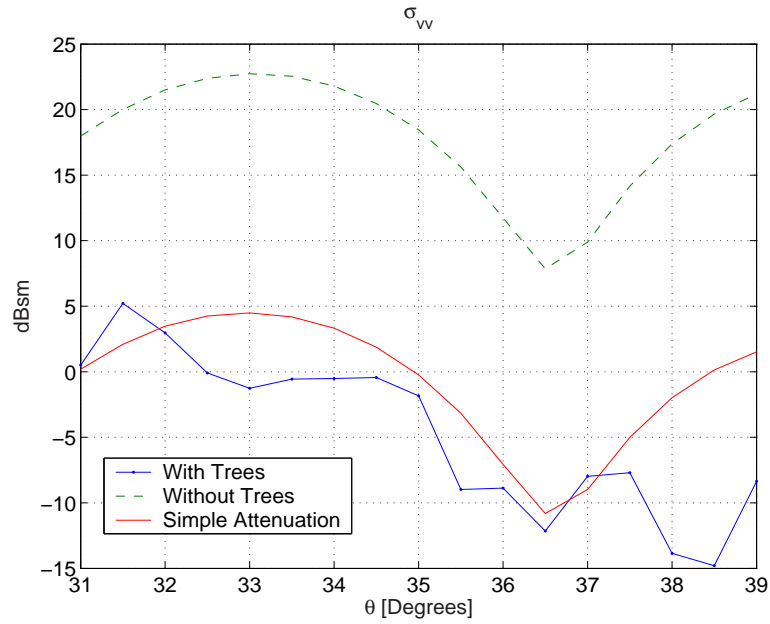


Figure 3.8: Calculated backscattering coefficient of the pine stand as a function of elevation and azimuth angles of  $\theta_i$  and  $\phi_i$ . (a)  $\sigma_{hh}^o$  and (c)  $\sigma_{vv}^o$ . Also shown the backscattering coefficient at  $\phi_i = 180^\circ$  and for different elevation angles. I-bar on the mean value shows the fluctuation range of the backscattering coefficient for 10 Monte Carlo simulations. (b)  $\sigma_{hh}^o$  and (d)  $\sigma_{vv}^o$ .

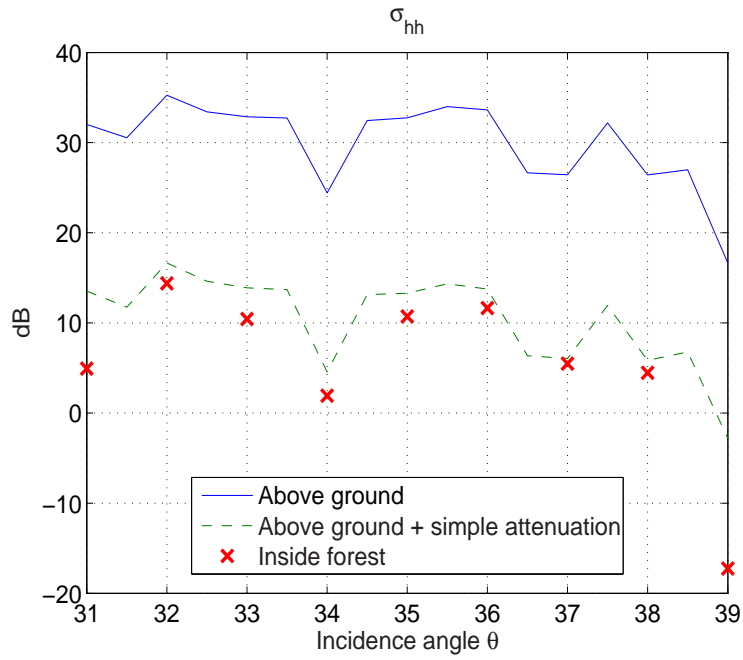


(a)

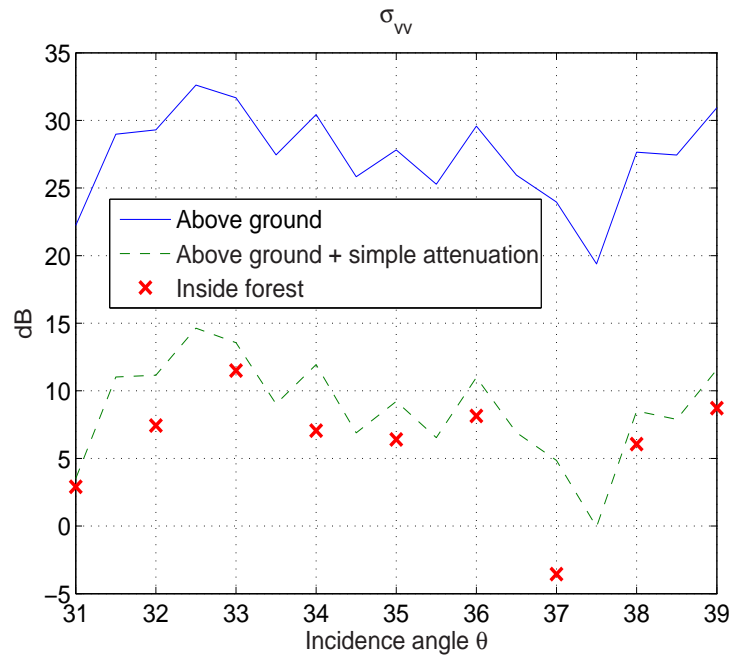


(b)

Figure 3.9: Backscattered RCS of the metallic structure shown in Fig. 3.3, with dimensions of  $AB = 8\lambda$ ,  $BC = 4\lambda$ ,  $CD = GH = 2.5\lambda$  and  $DE = EF = 3\lambda$ , and a length of  $5\lambda$  along the  $\hat{y}$  direction, placed above a lossy dielectric ground at frequency of 2 GHz, as a function of the incident angle  $\theta_i$ , for  $\phi_i = 180^\circ$ , inside and outside the forest. The density of pine trees is  $0.05 \text{ trees}/\text{m}^2$ . (a)  $\sigma_{hh}$  and (b)  $\sigma_{vv}$ . Direct backscatter from the forest is not shown in these figures.



(a)



(b)

Figure 3.10: Backscatter RCS of the metallic tank shown in Fig.3.4(a) at frequency of 2 GHz, as a function of the incident angle  $\theta_i$ , for  $\phi_i = 180^\circ$  with and without the effect of forest. (a)  $\sigma_{hh}$  and (b)  $\sigma_{vv}$ .

Table 3.1: Run time required for each realization of the forest and each incidence angle.

	Num. of facets	Num. of scatterers	Processor [GHz]	RAM [GB]	Storage of currents	Run time
<i>Fig.3.7</i>	144	50000	2.0	0.5	<i>Yes</i>	<i>1 hour</i>
<i>Fig.3.9</i>	7,534	50000	2.0	1.0	<i>No</i>	<i>1 day</i>
<i>Fig.3.10</i>	325,300	10000	2.0	1.0	<i>No</i>	<i>1 week</i>

## 3.6 Conclusion

A novel computationally efficient hybrid target-foliage model is developed for investigating methods for detecting foliage-camouflaged targets. The model is based on the reciprocity theorem for calculation of backscattering and a hybrid GOPOPO method for efficient calculation of induced currents on hard targets embedded in foliage. The proposed method for calculation of RCS is verified using the MoM and RCS measurement of a scaled model at millimeter wave frequencies. In addition, a sensitivity study has been carried out to demonstrate the sensitivity of the backscatter from metallic targets under forest canopies to the polarization, incidence angle and forest realizations. The results clearly indicate the significance of the scattering from tree components on the target response at the microwave frequencies as low as 2 GHz.

## CHAPTER 4

# Analysis of Optimum Polarization for Discrimination of Foliage Camouflaged Hard Targets Using Genetic Algorithms

Using the hybrid target-foliage model, developed for investigating the scattering behavior of metallic hard targets embedded inside a forest canopy at high frequencies, given in chapter 3 many realizations of foliage around a hard target are run to obtain the statistical variations of foliage and target response in a Monte Carlo simulation. This model is based on coherent scattering theory for computation of wave propagation through and scattering from forest and iterative physical optics approximation, for scattering from the hard target. The interaction between these two carried out using reciprocity theorem. Using this powerful foliage-target simulation tool which accounts for near-field interactions between the hard target and foliage, fully polarimetric simulation results of a foliage camouflaged metallic target with compound geometry, performed at 2 GHz, are collected and a polarization synthesis optimization method for improving signal to clutter is presented, by applying genetic algorithms.

### 4.1 Introduction

A very comprehensive physics-based foliage and target scattering model has recently been developed that can account for near field interactions among foliage, ground, and the

target [18], [19]. In this model, individual tree in forest stand is decomposed into its basic constituents, trunk, branches and leaves which are respectively modeled by dielectric cylinders and thin dielectric disks, whose dielectric constants are functions of moisture content, frequency, and temperature [81]. Structure of trees are preserved using a statistical Lindenmayer system which can generate very complex tree structures with a finite number of structural and botanical parameters. Next, single scattering theory, which also includes the interaction of the scatterers with the ground plane, is applied to compute the scattering from and propagation through the forest canopy. The ground plane is modeled by a dielectric half-space whose dielectric constant is mainly determined based on the frequency, soil moisture content, and percentage of sand and clay [82].

The field at a given point inside the foliage is obtained by coherent addition of all the scattering contributions from all adjacent tree components, illuminated by the mean field, and its reflection from the ground. This is in addition to the direct field, attenuated by the foliage (mean field) and its reflection from the ground that directly goes through the foliage. The mean field is computed using Foldy's approximation, which accounts for the phase change as well as extinction due to the scattering and absorption of the tree particles. Scattering from large scatterers are formulated in a uniform fashion that allows field computation from the scatterer near-field to far-field region [19]. Using this foliage model, a hybrid target-foliage model is then developed for investigating the scattering behavior of metallic hard targets embedded inside a forest canopy, at high frequencies [76]. Reciprocity theorem is used very effectively to compute the backscattered field using the incident fields on the target, and induced electric currents. In this hybrid model, calculation of induced electric currents on the target is done using an efficient iterative Physical Optics (PO) and Geometrical Optics (GO) approximations.

The problem of particular interest is to discriminate the target backscattering response from that of the clutter. One way of achieving this, is to investigate the polarization responses of the foliage, and the foliage embedded target and examine whether there exists a particular set of transmit and receive polarizations that maximizes the signal to clutter in the statistical sense. An optimization procedure is needed to find the optimal radar polarization configuration for different clutter realizations and keeping the same target inside the clutter.

Optimization algorithms may be divided into two groups 1) gradient-based methods and 2) stochastic search algorithms. For electromagnetic problems, where there exists a large number of dimensions with many likely local maxima, the gradient-based optimization methods fail to perform a global optimization. On the other hand, stochastic search algorithms such as simulated annealing [83] and genetic algorithms (GA) [84] have very robust features for such optimization problems.

GA has been successfully used before to characterize the optimum polarization for multiple target discrimination [84]. In this chapter, we employ genetic algorithms to find optimum polarization configurations which suppress the effect of forest on the response of the backscattered RCS of a camouflaged hard target. The process is based on the fully polarimetric responses, achieved by running many realizations of foliage around a hard target. The chapter is organized as follows: In Section 4.2, we address the backscattering computation of metallic hard targets inside the foliage and the implementation of genetic algorithm. In Section 4.3, performance of GA is shown and results are provided.

## 4.2 Theory

In calculation of scattering from forest camouflaged target, we used reciprocity theorem. Consider  $\bar{E}_1$  to be the total incident electric field, composed of all the scattering contributions from each tree component in addition to the mean fields and their ground bounces, and  $\bar{J}_2$  is the total electric current on the target. Using reciprocity theorem it can be shown that each component of the backscattered field from target can be computed from [76]

$$\mathbf{S}_{pq}^t = \pm \frac{ik_o Z_o}{4\pi} \int_{\mathbf{S}} \bar{E}_{1p} \cdot \bar{J}_{2q} ds' \quad (4.1)$$

where subscript  $p$  and  $q$  can be  $h$  or  $v$  for horizontal and vertical polarizations. In (4.1) the first and second subscripts denote the receive and the transmit polarizations, respectively. Therefore,  $\bar{E}_{1p}$  is the  $p$ -component of the total incident field on the target, and  $\bar{J}_{2q}$  is the electric current on the surface of the hard target, induced by the  $q$ -polarized incident wave. Generally, polarization unit vectors  $\hat{h}_t$  and  $\hat{v}_t$ , respectively for horizontal and vertical

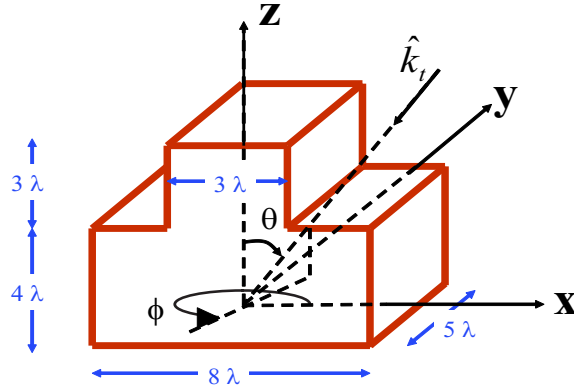


Figure 4.1: The metallic object used as a target embedded inside the forest. Frequency of operation is  $2\text{ GHz}$ . For TE polarization of incident field,  $\phi = 180^\circ$ , and different elevation angles  $\theta$  the backscattered RCS from such an object is reported in [76].

polarization of transmit wave, can be defined in a global coordinate system by

$$\begin{aligned}\hat{h}_t &= \frac{\hat{k}_t \times \hat{z}}{|\hat{k}_t \times \hat{z}|} \\ \hat{v}_t &= \hat{h}_t \times \hat{k}_t\end{aligned}\quad (4.2)$$

where  $\hat{k}_t$  is the propagation unit vector of the transmit field. Therefore, for the backscattered field which  $\hat{k}_r = -\hat{k}_t$ , we have  $\hat{h}_r = -\hat{h}_t$  and  $\hat{v}_r = \hat{v}_t$ . That is the minus sign in (4.1) is chosen when  $p$  is vertical polarization.

Due to the typical electric size of hard targets, we used PO approximation for computation of  $\bar{J}_2$ . For electrically large objects, PO approximation can provide very accurate scattered field near specular directions. In a forest with many scatterers around, many specular points can be obtained. This improves the accuracy of the PO, substantially. The iterative PO approximation is applied to a metallic target, shown in Fig. 4.1. For computation of backscatter RCS a radar operating at frequency of  $2\text{ GHz}$  is assumed. The scattering problem is also solved by exact numerical computation of method of moment (MoM), based on electric field integral equation (EFIE). Very good agreement between backscatter field for a TE polarized incident wave, propagating along  $\phi = 180^\circ$ , and different elevation angles  $\theta$  was observed. The comparison for different dimensions of this metallic object is reported

in [76]. The iteration process converges fast, and takes the effect of shadowing and multiple scattering on the target into account simultaneously. This makes the results more accurate than first order PO.

### 4.2.1 Problem Formulation

The total backscattering which is measured at the radar is basically superposition of embedded target response and clutter response

$$\mathbf{S}_{pq} = \mathbf{S}_{pq}^t + \mathbf{S}_{pq}^c \quad (4.3)$$

where  $\mathbf{S}^t$  is the target backscatter (4.1), and  $\mathbf{S}^c$  is the clutter backscatter, computed directly using single scattering theory. If the transmit and receive polarizations are  $\bar{P}^t$  and  $\bar{P}^r$  respectively, the backscattered field is proportional to  $\bar{P}^{rT} \mathbf{S} \bar{P}^t$ , where superscript  $T$  is for transpose. Hence according to (4.3), the backscattered field has two terms. First term is scattered field from embedded target and second term is from the clutter. If we can find a set of transmit and receive polarization configurations which can minimize the scattering contribution from the clutter (second term), compared to the scattering from the embedded target (first term), then the overall backscatter field has signature of the target, provided that the backscattering from embedded target is not totally distorted by scattering of the forest. Knowing the scattering matrices of embedded target, or clutter we can determine their RCS analytically using [71]

$$\sigma_{pq}(\psi_r, \chi_r : \psi_t, \chi_t) = 4\pi \mathbf{U}^T \mathbf{C} \mathbf{U}^* \quad (4.4)$$

where  $\mathbf{U}$  is the polarization cross-product vector,  $*$  is for complex conjugate

$$\mathbf{U} = \begin{pmatrix} P_v^r P_v^t \\ P_v^r P_h^t \\ P_h^r P_v^t \\ P_h^r P_h^t \end{pmatrix} \quad (4.5)$$

and  $\mathbf{C}$  is the  $4 \times 4$  covariance matrix. In (4.5), polarization unit vector is defined as

$$\bar{\mathbf{P}}^j = \frac{\hat{v}_j + a_j e^{i\delta_j} \hat{h}_j}{\sqrt{1 + a_j^2}} \quad (4.6)$$

where  $j$  can be  $t$  or  $r$ , respectively for transmit and receive fields.  $a_j$  and  $\delta_j$  are described in terms of the tilt angle  $\psi_j$  and ellipticity angle  $\chi_j$ , using

$$\begin{aligned} \tan(\delta_j) &= \frac{\tan(2\chi_j)}{\sin(2\psi_j)} \\ a_j &= \tan\left\{\frac{1}{2} \cos^{-1}[\cos(2\chi_j) \cos(2\psi_j)]\right\} \end{aligned} \quad (4.7)$$

In (4.7) determination of  $\delta_j$  is not unique. Since  $a_j$  is always a positive number, sign of  $\delta_j$  determines polarization handedness. Therefore, based on sign of  $\chi_j$ , sign of  $\delta_j$  is determined. The constraints presented in [84] are applied to remove the uncertainty. It should be noted that since we used  $e^{-i\omega t}$  time dependence,  $\delta_j \geq 0$  ( $\chi_j \geq 0$ ) is for right hand polarization, and  $\delta_j \leq 0$  ( $\chi_j \leq 0$ ) is for left hand polarization. In order to suppress the backscattering RCS from clutter, we may apply two polarization optimizations. First optimization is to maximize the minimum ratio of the backscatter RCS from the embedded target to the backscatter RCS from the clutter among all realizations of forest around the target. Mathematically, the objective function is,

$$\begin{aligned} \text{Maximize}\{ \text{Min}\left\{ \frac{\sigma_t}{\sigma_c}(\psi_r, \chi_r : \psi_t, \chi_t) \right\}_m \}_p \\ \forall m \in \{1, 2, \dots, N_R\} \end{aligned} \quad (4.8)$$

subject to

$$\psi_r, \psi_t \in [-90^\circ, 90^\circ] \quad \chi_r, \chi_t \in [-45^\circ, 45^\circ] \quad (4.9)$$

where  $m$  is the realization number, subscript  $p$  stands for polarization and  $N_R$  is the total number of realizations of the forest. The advantage of optimization (4.8) is finding a maximum level which a set of optimum polarization configurations provides. Basically, minimum level of signal-to-clutter ratio, among all realizations of the forest, achieved by other polariza-

tion configurations, is less than maximum level, characterized by (4.8). The shortcoming of this optimization occurs when the number of realizations of the forest are very large. In this case, some situations may happen that the embedded target backscatter is totally distorted by the scattering from the trees. For example, consider the case where trunk of a nearby tree to the target blocks the incident wave directly. Such a case among all other realizations may change the optimization of (4.8) significantly, and in limit where the number of realizations  $N_R$  goes to infinity,  $Max\{Min\{\frac{\sigma_t}{\sigma_c}\}\}$  approaches zero, and not a useful polarization configuration is found. Therefore another optimization is needed that the effect of such cases are removed.

Basically instead of maximizing the minimum level, which is a worse case scenario, we maximize the number of cases where ratio of the backscatter RCS from embedded target to the backscatter RCS from the clutter is more than a specified level for all realizations of forest. Therefore, the objective function for finding this optimum polarization is

$$\begin{aligned}
 &Maximize\{N[\frac{\sigma_t}{\sigma_c}(\psi_r, \chi_r : \psi_t, \chi_t) > L]_m\}_p & (4.10) \\
 &\forall m \in \{1, 2, \dots, N_R\}
 \end{aligned}$$

subject to (4.9), where  $L$  is a predefined level. Clearly by optimization of (4.10), the probability of having higher signal-to-clutter ratios is increased, and specifically the effect of realizations where response of the embedded target is totally distorted by the forest scattering is eliminated. The disadvantage of this optimization is that its performance depends on the prescribed level  $L$ . Based on the size of the target, backscatter RCS of the target alone in absence of forest, and foot print of the radar, range of this level may be inspected. Lower level of  $L$  make the constrain loose and accordingly provide more options for optimum polarization configurations while for higher levels, optimization may not be performed, successfully. Optimizations (4.8) and (4.10) have been performed using GA. In the following subsection the implementation of GA is outlined.

## 4.2.2 Genetic Algorithm Realization

Generally any genetic algorithm consists of basic 6 steps, 1) Discretization of parameter space, 2) Defining an arbitrary encoding approach to set up a one-to-one relationship between each code and each point in the parameter space, 3) Initialization of parameters, random generation of initial population, 4) Evaluation of parameters' fitness based on objective function and selection of high-ranked parameters, 5) mating and mutation, and 6) Iteration of step 4 and step 5 until termination criteria, convergence, is met.

At the first step we need to discretize the parameter space. For problem at hand the parameter space is a 4-D vector space, consisting of two sets  $(\psi_r, \chi_r)$ , and  $(\psi_t, \chi_t)$ , representing the receive and transmit polarization configurations respectively. Since each set can be associated with a point on a Poincare sphere we need to discretize the area of that sphere into a reasonable number of pixels and associate the longitude and latitude of each pixel to  $\psi$  and  $\chi$  accordingly. Since RCS is a smooth function of polarization angles,  $\chi$  is uniformly discretized with a spacing of  $\Delta\chi = 1^\circ$ . On the other hand, discretization of  $\psi$  can also be performed linearly, achieving more precise results, in expense of a large parameter space. However this may make the optimization an inefficient procedure.

As proposed in [84] the area of each pixel on the Poincare sphere is kept constant. Knowing that area of each pixel depending on specific  $\chi$  is  $\Delta A = 4 I_o^2 \cos(2\chi) \Delta\chi\Delta\psi$ , we have  $\Delta\psi = 180/(N_p \cos(2\chi))$  radians, where  $N_p$  is the total number of pixels. A binary transformation is used for encoding the parameter space, therefore  $N_p = 2^n$  for an integer  $n$  (this is an accomplishment of step 2). For each  $\chi$ , a number of discretized  $\psi$  points, called  $k(\chi)$ , is assigned. Angular form of  $k(\chi)$  is given by  $k(\chi) = \pi/\Delta\psi = (\pi/180) 2^n \cos(2\chi)$ . To get a complete one-to-one encoding transformation we need to have  $\sum_{\chi=-45}^{\chi=45} k(\chi) = 2^n$ . For  $n = 13$  discretized points of  $k(\chi)$ , reported in [84] (table I), are used in this chapter. Combining the receive and transmit genes would results in a 26-bit binary code representing a point in parameter space. Therefore number of total points are 67,108,864 chromosomes.

After random generation of first population in step 3, all chromosomes are sorted based on their fitness values and in step 4 50% of high qualified chromosomes are selected. This selection is known as deterministic approach in contrast with stochastic approaches in which

selection of a chromosome is based on a probability, proportional to its fitness value. In step 5 mating is performed using crossover operation. In this approach, crossover point in parents' chromosomes is selected randomly. Left part of crossover point is preserved in offsprings' chromosomes and the rest of binary codes in parents' chromosomes are swapped in their offsprings' chromosomes. Therefore new parameters with high fitness values are generated. Also mutation should be done to diversify the population. However, the mutation probability is kept small in order to observe convergence. This is accomplished by changing a randomly selected bit from zero to one or vice versa, carried out for a portion of chromosomes. Bit mutation with probability of less than 1% is kept. Step 6 is to check the termination criteria. The convergence is achieved if no difference is observed in fitness value of the best qualified chromosome after certain number of iterations. In this chapter we set this number to be 10.

### 4.3 Simulation Results

Optimization (4.8) is performed on the same metallic target as shown in Fig. 4.1 (a), placed just above a dielectric half space with relative dielectric constant of  $\epsilon_r = 5.6 + i0.8$ , inside a forest, including 10 pine trees with density of  $0.05 \text{ trees}/m^2$  randomly located around the target. Pine trees are generated by the statistical L-system having average height of 15  $m$ , crown radius of 3  $m$ , crown height of 10  $m$ , trunk radius of 10  $cm$ , and more than 5000 dielectric scatterers per tree. Frequency of operation is 2 GHz, and incident field is along  $\theta_i = 35^\circ$ , and  $\phi_i = 180^\circ$ . Since the operating frequency is relatively low, the scattering effect of the needles is ignored.

For  $N_R = 10$  realizations of forest, initial population of 200 chromosomes and different seeds ( $seed = \{1, 2, \dots, 20\}$ ) the optimization is carried out. Basically each seed number provides an initial random population. Two sets of solution are found where the optimum values of the polarization angles are shown in table 4.1. Using the optimum polarization state, the maximum backscattered RCS ratio of target to clutter of  $-6.81 \text{ dB}$  is achieved, assuming the radar footprint or pixel area to be  $200 \text{ m}^2$ . Table 4.1 shows the signal-to-clutter ratio when the polarization configuration is simply V- or H- polarizations. In comparison, about 10  $\text{dB}$  improvement can be achieved. It should be noted that in this optimization

among the realizations, response of the target is not distorted with scattering effect of forest drastically. It is observed that the max-min values eventually approaches to zero, for many more realizations.

Furthermore,  $N_R = 100$  realizations have been collected to examine the statistical variations of foliage and target response in a Monte Carlo simulation. Optimization (4.10) is performed for different levels of  $L$ , about  $-13dB$ ,  $-8dB$ , and  $-3dB$ . These values are selected around  $-6.81 dB$ . Initial population of 200 chromosomes and different seed numbers ( $seed = \{1, 2, \dots, 100\}$ ) are considered in the optimization process. For different seed numbers the optimum tilt angle  $\psi$  and the ellipticity angle  $\chi$  are shown in Fig. 4.2. In this simulation  $L = -8dB$ . As expected, two sets of solutions almost symmetric with respect to  $\hat{v}$  direction are obtained. Tilt angle  $\psi$  can have solution between 20 to 40 degrees and -20 to -40 degrees while ellipticity angle  $\chi$  is around zero. Similar results are also observed for  $L = -3dB$  and for  $L = -13dB$ . Remarkably the transmit and receive fields have polarizations perpendicular to the direction of branches and they are symmetric with respect to  $\hat{v}$  direction (see Fig. 4.3).

Figures 4.4 (a), (b) and (c) show the maximum cost value obtained in terms of number of iterations and for different seed numbers. As shown, optimizations converge fast with less than 30 iterations. Figures 4.4 (d), (e) and (f) show histograms of signal-to-clutter ratio achieved by optimization for different levels of  $L$ . In comparison, it is observed an increase in the number of cases where signal-to-clutter ratio is more than the specified level. Two states of polarization achieved for  $L = -8 dB$  is reported in table 4.2. Using these optimum polarization configurations we may have signal-to-clutter ratio of more than  $-8 dB$  for about 70% of the times.

The average covariance matrices of embedded target and clutter are calculated using 100 independent realizations of forest around the target. Figure 4.5 shows the co-polarized responses of the target embedded in the forest and clutter alone, where responses of the pine forest is in agreement with reported results provided by measurement in [71] (p. 260). A genetic searching algorithm is performed to maximize the signal-to-clutter ratio, employing the average covariance matrices. Figure 4.6 shows the optimum tilt and ellipticity angles of transmit and receive polarizations. Consistent results are also observed for maximization of

signal-to-clutter ratio, in average sense.

## 4.4 Conclusion

Based on fully polarimetric simulation scattering results, performed at low microwave frequencies, from a camouflaged metallic target with complex geometry in pine foliage, a target detection algorithm using a polarimetric radar is demonstrated. Genetic algorithm is used in order to achieve the optimum radar polarization configuration for both transmit and receive antennas to maximize the signal to clutter ratio. It is shown that independent of forest realizations (tree arrangement around the target) there exists a set of polarization that enhances signal to clutter ratio. It is shown that for the optimum polarization set, the transmit and receive electric fields are aligned approximately perpendicular to the direction of branches and have symmetry with respect to the tree trunk direction.

Table 4.1: (a) The optimum polarization states, derived by genetic algorithm using 20 different seeds for initial population sets of 200 chromosomes for maximization of target to clutter backscattering RCS ratio. (b) Minimum target to clutter backscattering RCS ratio for H- and V- polarizations.

(a)

	$\psi_r$	$\chi_r$	$\psi_t$	$\chi_t$	$Max\{Min\{\sigma_t/\sigma_c\}\}$
<i>1<sup>st</sup> Solution</i>	$25.71^\circ$	$-1.0^\circ$	$36.0^\circ$	$6.0^\circ$	$-6.81\text{ dB}$
<i>2<sup>nd</sup> Solution</i>	$-36.0^\circ$	$-10.0^\circ$	$-21.31^\circ$	$2.0^\circ$	$-7.17\text{ dB}$

(b)

	$Min\{\sigma_t/\sigma_c\}$
<i>H – Polarization</i>	$-18.41\text{ dB}$
<i>V – Polarization</i>	$-15.18\text{ dB}$

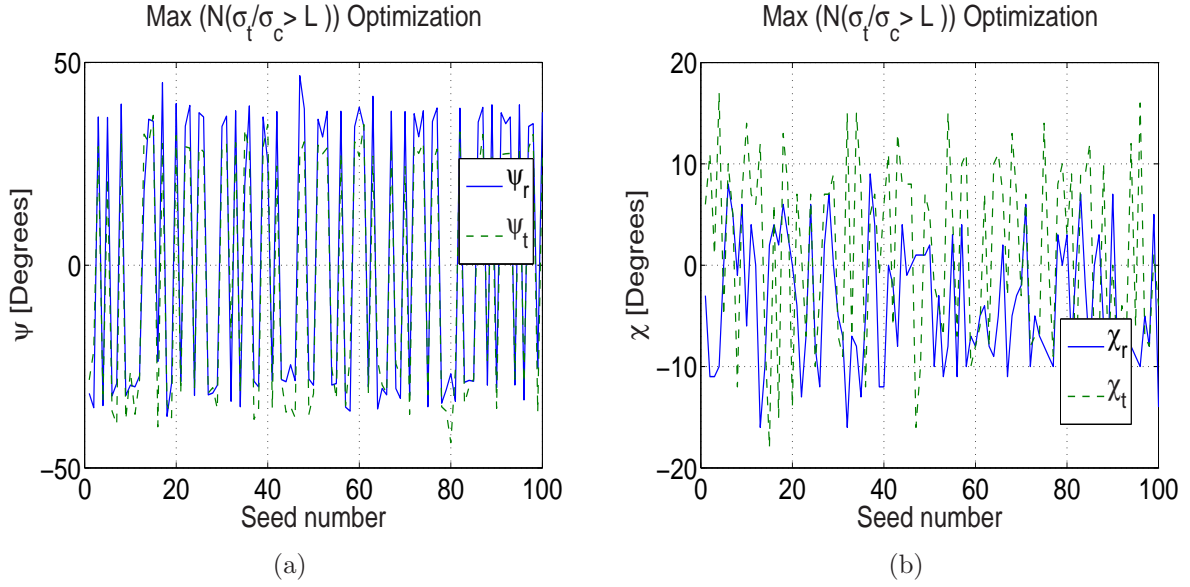


Figure 4.2: Polarization angles (a)  $\psi$  and (b)  $\chi$  for transmit and receive waves, obtained by different seeds, in optimization of  $Max\{N[\frac{\sigma_t}{\sigma_c} > L]\}$ , performed for  $L = -8\text{dB}$ .

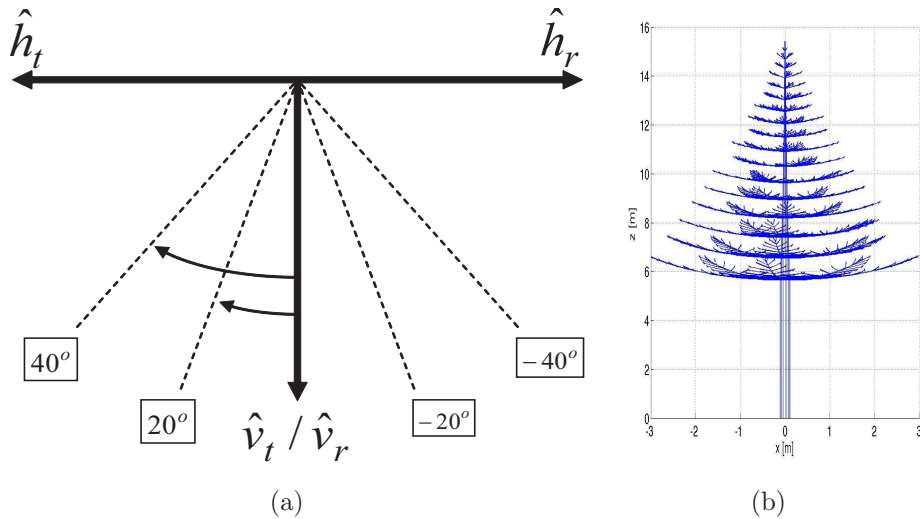


Figure 4.3: (a) Solution regions for tilt angle of transmit and receive polarizations. (b) Structure of a typical pine stand generated in simulation.

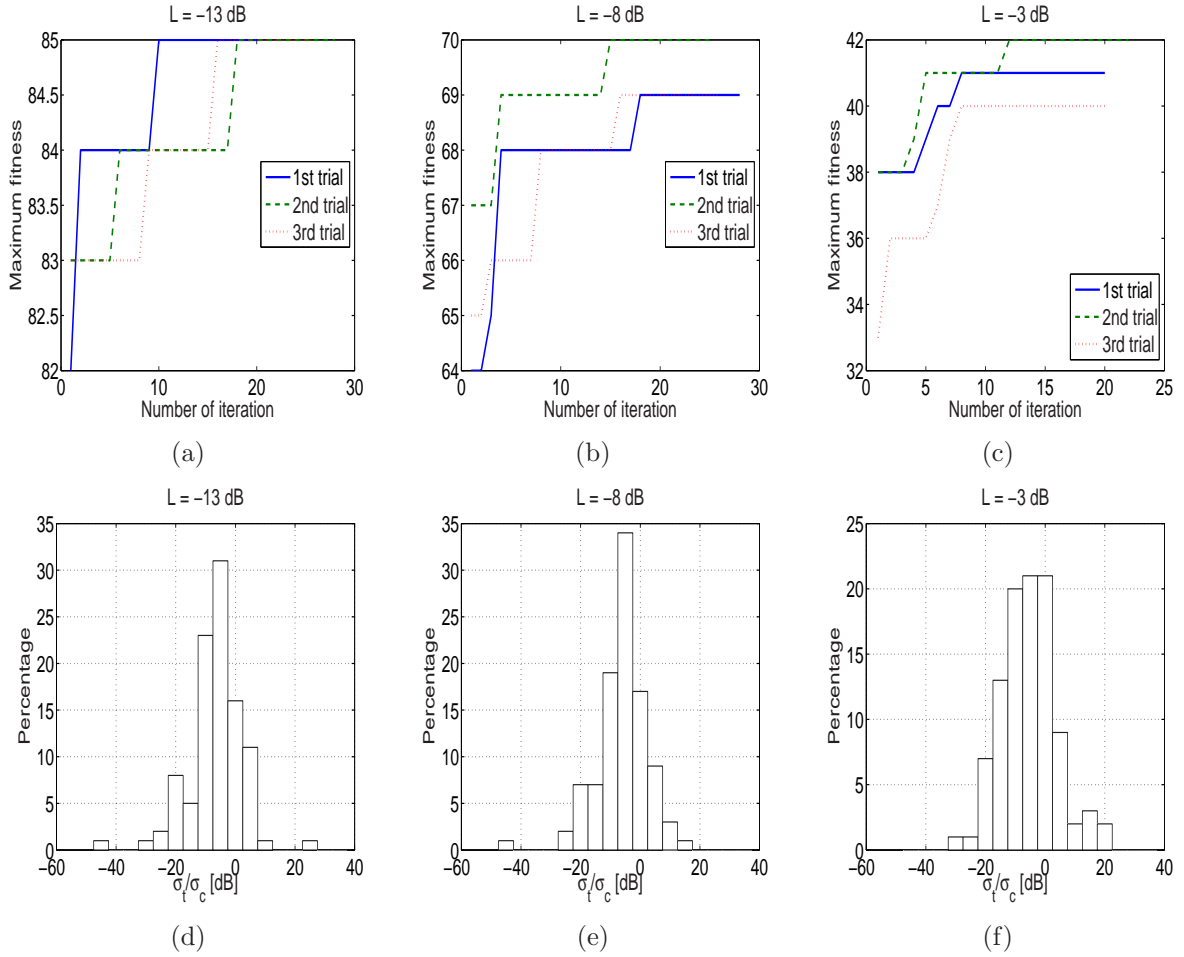


Figure 4.4: The convergence performance of GA in optimization of (4.10) for (a)  $L = -13$  dB, (b)  $-8$  dB and (c)  $-3$  dB. Histogram of signal-to-clutter ratio, using 100 realizations of forest around the hard target for (d)  $L = -13$  dB, (e)  $-8$  dB and (f)  $-3$  dB.

Table 4.2: The optimum polarization states, derived by genetic algorithm using 100 different seeds for initial population sets of 200 chromosomes for optimization (4.10).

	$\psi_r$	$\chi_r$	$\psi_t$	$\chi_t$	$Max\{N[\sigma_t/\sigma_c > -8 \text{ dB}]\}$
1st Solution	$38.95^\circ$	$-8^\circ$	$26.86^\circ$	$-8^\circ$	71
2nd Solution	$-31.62^\circ$	$-3^\circ$	$-28.28^\circ$	$6^\circ$	70

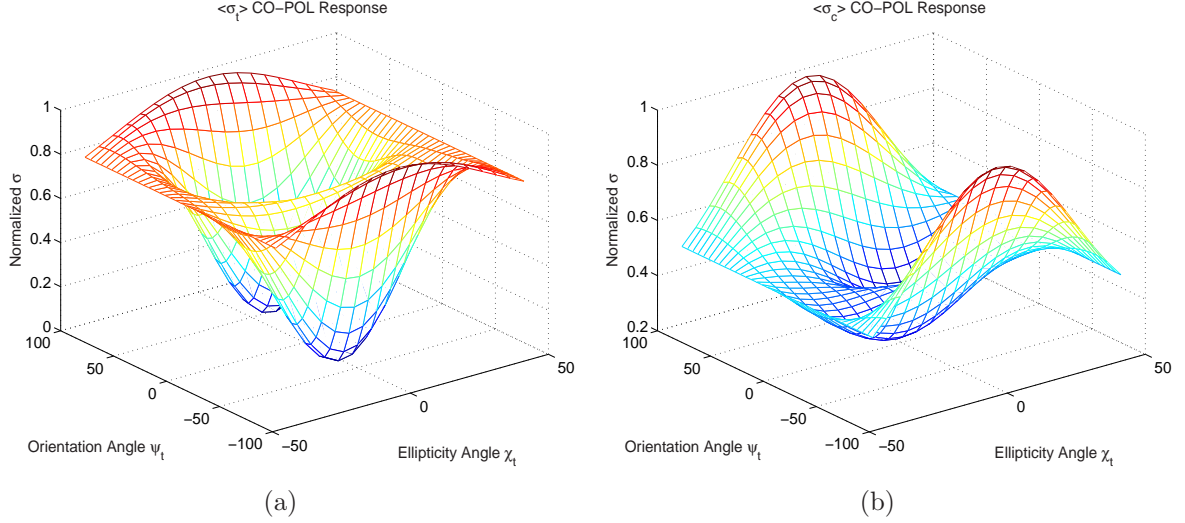


Figure 4.5: Normalized co-polarized backscatter polarization response of the target embedded in foliage and the clutter for an incident plane wave propagating along  $\theta_i = 35^\circ$ , and  $\phi_i = 180^\circ$ , using average covariance matrix of 100 realizations. co-polarization of (a) the target in presence of the foliage and (b) the clutter alone.

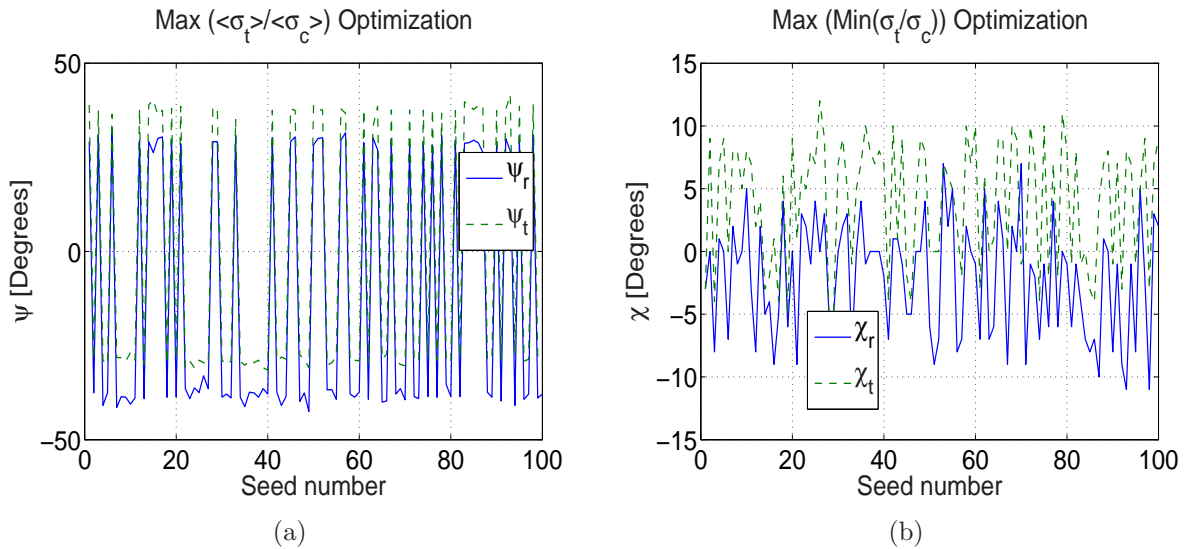


Figure 4.6: Optimum polarization angles of transmit and receive waves, obtained by different seeds, in optimization of  $Max\{\frac{\langle \sigma_t \rangle}{\langle \sigma_c \rangle}\}$  (a)  $\psi$  and (b)  $\chi$ .

## CHAPTER 5

# Refocusing through Building Walls, Using Synthetic Aperture Radar

Through-wall imaging/sensing using synthetic aperture array technique is studied by employing ultra-wideband antennas and for wide incidence angles. The propagation through building walls such as brick and poured concrete in response to point sources near the walls is simulated, using high-frequency methods. Reciprocity is used to find the responses of point targets behind walls which are then used to simulate the Synthetic Aperture Radar (SAR) imaging through the walls. The effect of the building walls on the target image distortions is investigated by simulations and measurements. It is shown that using the idea of match filtering, the effect of the wall can be compensated for and point target response can be reconstructed provided that the wall parameters are known. An optimization method based on minimization of squared error in the SAR image domain within an area confined within expected point spread function is used to estimate the wall parameters and sharpening the image simultaneously. A controlled experiment within the laboratory environment is performed to verify the methods presented. It is shown that for an ultra-wideband system operating over frequency band of 1-3 GHz highly distorted images of two point targets in close proximity of each other behind a wall can be resolved after refocusing. A dual-frequency synthetic method is also presented that can improve the cross-range resolution of the refocused image.

## 5.1 Introduction

There exists a great interest for ability to image the interior of a building and identifying the signature of the interior objects using remote sensing tools [48]-[86]. Solutions to this problem may make many civilian and law enforcement applications possible. For example earthquake rescue operations, police search operations, hostage situations or threat assessment situations, all require the ability to detect and identify objects hidden behind walls.

The capabilities of electromagnetic (EM) waves to penetrate through non-metallic building materials such as wood, glass, plastic, fiberglass, drywalls, cinder blocks, brick and concrete blocks provides a unique opportunity to image inside of optically opaque manmade structures. In addition, since the EM reflections from various materials are different, enough contrast may be provided to identify targets inside. The identification of targets can be further facilitated by providing enough resolution in the images. To achieve the required resolution, operation at high frequencies with a large frequency bandwidth provides the best results. However, the upper limit of frequency of operation is limited by attenuation through the materials. Attenuation of EM waves through different materials has been reported in literature [46], [47]. For example to image targets in the dark, through smoke, or behind thin fibers, infrared frequencies can be used. For imaging through paper, fiberglass, plastic, glass, wood, and drywalls whose attenuations are relatively low millimeter-waves (e.g. 95 GHz) are suggested [48], [49]. Observation shows that attenuation through brick and concrete walls is relatively high due to the construction materials' loss-tangent, moisture contents, and wall thickness. Therefore, depending on the sensitivity of the transceiver system, EM spectrum in the range of UHF to low microwave frequencies are used [33], [50]. Advance tools from microwave sensors and radar technologies can provide the best applicable solutions.

For a scenario where stationary targets are behind building walls, radar system is used to collect the backscattering fields of the targets. The required resolutions to detect human and other objects of similar size is of the order of 10-15 cm. This corresponds to the usage of 1-1.5 GHz of bandwidth at UHF to low microwave frequencies to provide the required range resolution. Cross-range resolutions on the other hand are obtained either by real or synthetic

apertures. Since 3 dB beamwidth of a real aperture radar (cross-range resolution) is inversely proportional to the size of the antenna, operating at lower part of the frequency band requires quite a large aperture size. For instance, at frequency of 1 GHz, 3 dB beamwidth of 10 cm at a range of 1 m is met by an aperture size of about 3 meters. For practical reasons, a synthetic aperture array formation using a relatively small ultra-wideband antenna is preferred. In practice however there is a tradeoff between the required cross-range resolution and the required time to collect the data. An example of such approach is a transient Impulse Synthetic Aperture Radar (ImpSAR), operating at 250-3500 MHz, capable of imaging targets behind walls from a large distance, with resolutions better than ten centimeters [33].

These techniques such as synthetic aperture beamformer using multiple stationary transmit and receive antennas have also been proposed in [34]. The effect of the wall on the target image (i.e. a shift in the target position) and the effect of the wall parameter ambiguities on the performance of the beamformer are provided using computer simulations [34]-[87]. In this chapter, a comprehensive numerical and experimental study is presented that considers different scenarios where the transceiver antenna is moving along a known path away from the wall. Through-wall microwave imaging for various walls including brick and concrete walls is studied. A part from the shift in the target position in the range direction, widening of point spread functions along the cross-range direction, is observed. The latter can significantly degrade SAR image resolution and the system ability to detect/identify the target behind walls. In order to study this effect, transmissivity through building walls are measured and methods for refocusing are provided. Also a post-processing method for enhancing cross-range resolution for the ultra-wideband system is demonstrated. The significance of refocusing methods is illustrated when multiple targets close to each other, are placed behind walls.

The chapter is organized as follows. In Section 5.2, the effect of the walls on the target image and compensation methods for refocusing are addressed through simulations. In this section, the sensitivity of the method to the wall permittivity and thickness is also provided. In Section 5.3, a stepped-frequency synthetic aperture radar system, consisting of two double ridge horn antennas (for ultra-wideband operation), a vector network analyzer and a precision XY-table is set up for the experimental study. Parameters of concern such as

frequency response of the antennas and permittivity of the wall are measured. Experimental image formation and refocusing are demonstrated and it is shown that the resolutions of the images can be significantly improved, and detection of multiple targets in close proximity of each other is possible.

## 5.2 Numerical Simulations

At low microwave frequencies, we may categorize walls into two groups: 1) homogenous walls such as brick, adobe, and poured concrete walls and 2) inhomogeneous walls, such as cinder block, drywalls and re-enforced concrete walls. In this chapter we investigate the effect of the homogeneous walls on the target image.

The following subsections address the basic formulation for constructing the target image using the synthetic aperture array, and the effect of the wall on a point target through numerical computation. Since the wall transmissivity is a function of both frequency and incidence angle SAR images through walls are perturbed. To remove the wall effects, the idea of match filtering is used to refocus the target image. To mitigate the adverse effects of noise for frequencies at which the magnitude of transmission coefficient is low, only phase of transmission coefficient is used to sharpen the image. By compensation of the target image, a resolution similar to the one when the target is imaged in free space is achieved. Also, the exact locations in the images are obtained.

### 5.2.1 Image Construction

Figure 6.1 shows a simple scenario of target detection behind a wall using a SAR system. As shown, the ultra-wideband transceiver antenna moves along the scan line with length of  $L$  and collects the backscattered field for different frequency and observation points. Here, the scan line is chosen to be parallel to the wall, located at  $x_o$ , and a point target is placed at  $-x_s$  behind the wall. Using the standard focused SAR imaging technique and assuming



where  $R_{0n} = |\bar{r}_n - \bar{r}_s|$ . In addition to the target response there is a signal reflected from the wall  $E_r^w$  whose response is given by

$$E_r^w(k_m) = \frac{G\lambda}{8\pi} \frac{e^{2ik_mx_0}}{x_0} \Gamma(\theta_i = 0, k_m) \quad (5.4)$$

where  $\Gamma(\theta_i = 0, k_m)$  is the reflectivity matrix from the wall at normal incidence angle. This reflected signal must be subtracted from the total received signal coherently in order to isolate the target signature on the other side. The effect of direct wall reflection on the target image is explained in Subsection 5.3.3. Along the synthetic aperture, it is assumed that the target is illuminated by the main beam of the antenna and that the antenna pattern does not significantly change inside that beam. Therefore, in equations (5.2) and (5.3), the gain angular dependance is neglected.

The transmissivity matrix  $T$  and reflectivity matrix  $\Gamma$  can be measured or computed by EM models. Here, the Geometric Optics approach is used for computation of transmissivity and reflectivity and also extracted through experimental study. Basically, building walls such as brick, adobe, and poured concrete walls can be modeled by homogeneous dielectric slabs. The matrices  $T$  and  $\Gamma$  are diagonal in the principal coordinate system and are given by

$$T = \begin{bmatrix} t_v & 0 \\ 0 & t_h \end{bmatrix}, \quad \Gamma = \begin{bmatrix} \gamma_v & 0 \\ 0 & \gamma_h \end{bmatrix} \quad (5.5)$$

where the transmission coefficient  $t_{v/h}$  and reflection coefficient  $\gamma_{v/h}$  respectively for vertically or horizontally polarized incident waves through a dielectric slab is given by [88]

$$\begin{aligned} t_{v/h} &= \frac{4 e^{i(k_{1x}-k_{0x})d}}{(1+p_{01})(1+p_{10})(1+R_{01}R_{10}e^{2ik_{1x}d})} \\ \gamma_{v/h} &= \frac{R_{01} + R_{10}e^{i2k_{1x}d}}{(1+R_{01}R_{10}e^{i2k_{1x}d})} \\ R_{10} &= -R_{01} = \frac{1-p_{10}}{1+p_{10}}, \quad p_{10} = \frac{1}{p_{01}}, \end{aligned} \quad (5.6)$$

where  $p_{10} = k_{0x}/k_{1x}$  for  $h$  polarization and  $p_{10} = \epsilon_r k_{0x}/k_{1x}$  for  $v$  polarization of the incident fields. In (7.18),  $\epsilon_r$  is the relative dielectric constant,  $d$  is the thickness of the wall, and

$k_{0x}$  and  $k_{1x}$  are the normal components of the propagation constants in the air and in the dielectric, respectively. The expressions for the vertical/transverse magnetic (TM) and horizontal/transverse electric (TE) unit vectors are given in [88].

Let us consider a scene composed of a brick wall and a point target whose scattering matrix is an identity matrix. The point target is assumed to be behind the brick wall at  $x_s = -0.5$  m. The relative dielectric constant of brick for different frequencies has been reported in the literature [89]-[90]. Accordingly in this example, we assume the permittivity of the brick is constant over the frequency band of 1-3 GHz and equal to  $4.0 + i 0.3$ . The wall thickness is 30 cm, frequency of operation is from 1 GHz to 3 GHz, and step frequency is 12.5 MHz. The antenna is moved in steps along a line (located at  $x_o = 0.5$  m) with steps of 2 cm over the length of  $L = 1.2$  m. Assuming the antenna gain  $G$  is known, the received signal is divided by  $G\lambda/4\pi$  to normalize the signal. For TE-polarized incidence field, the target is imaged, and the result is shown in Fig. 5.2(a). The effects of the wall transmissivity on the target image are: 1) dislocation of the target from its actual position in range, and 2) significant degradation in cross-range resolution.

In the absence of the wall, the point target image is well focused. The point-spread functions for a point target in free space are approximated by *Sinc* functions along the range and cross-range. Spatial resolutions along the range and cross-range are  $\Delta x = c/(2\Delta f)$  and  $\Delta y = \lambda_0(x_o - x_s)/(2L)$ , respectively [10], [91]. Here,  $\Delta f$  is the frequency band, and  $\lambda_0$  is the wavelength at the center frequency. The free space 3-dB spatial resolutions for our system ( $\Delta f = 2$  GHz,  $L = 1.2$  m) in range and cross-range are respectively  $\Delta x = 7$  cm and  $\Delta y = 6$  cm. However, in presence of the brick wall, the spatial resolutions are found to be  $\Delta x = 8$  cm and  $\Delta y = 34.5$  cm (see Fig. 5.3). The point-spread function distortion is exasperated when the wall thickness and/or its dielectric constant is increased. Also cross-range distortion is increased by the frequency bandwidth of the system. To refocus the target image, the effect of the wall has to be compensated for. In the following subsection the refocusing approach and its sensitivity is examined.

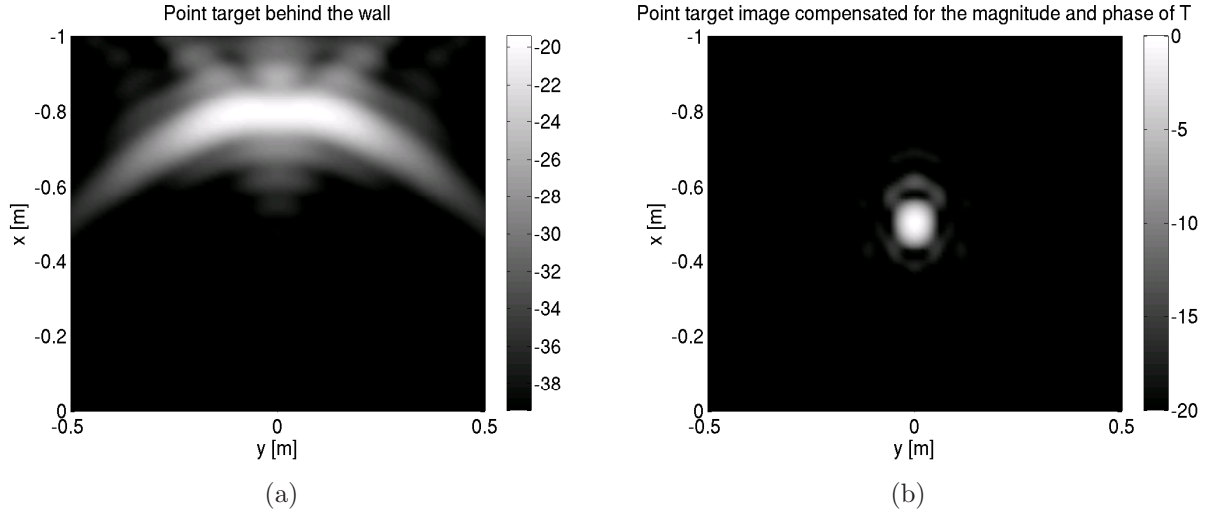


Figure 5.2: Images of the point target behind the brick wall, (a) standard SAR image and (b) refocused image with full compensation,  $C = T^{-2}$ .

## 5.2.2 Refocusing approach and sensitivity analysis

To capture the effect of the wall, instead of (5.1) the following equation is used

$$\tilde{S}^c(\bar{r}) = \frac{1}{N_p N_f} \sum_{m=1}^{N_f} \sum_{n=1}^{N_p} E_r^t(\bar{r}_n, k_m) C(\bar{r}_n, \bar{r}, k_m) R_n^2(\bar{r}_n, \bar{r}) e^{-2ik_m R_n(\bar{r}_n, \bar{r})}, \quad (5.7)$$

where  $C$  is a compensation factor. For the point target behind the brick wall in the previous example,  $C = T^{-2}(\bar{r}_n, \bar{r}, k_m)$  is chosen.  $\tilde{S}^c$  is computed and as shown in Fig.5.2(b) the target image is almost the same as the free-space target image. The spatial resolutions in the compensated image are  $\Delta x = 7$  cm, and  $\Delta y = 5$  cm.

The transmissivity matrix is a function of both frequency and incidence angle. In cases where transmissivity is low and the signal is noisy, division by a small noise-affected number may cause significant distortion. In such cases, one may use only the phase of transmission coefficients as a compensation factor. It is shown that phase compensation alone can refocus the image substantially (see Fig. 5.3). However, the phase compensation alone achieves resolutions that are less than those that can be obtained theoretically using  $C = T^{-2}$ . This is due to the fact that the attenuation through the wall increases by frequency and incidence

angles. In effect,  $C = e^{-2i\angle T}$  applies a windowing on both the frequency and aspect angle domains. The resolutions along the range and cross-range are respectively  $\Delta x = 7.7$  cm, and  $\Delta y = 6.2$  cm. Fig.5.3 shows the point spread functions along the range and cross-range. Results show that both compensation factors can refocus the target image very well.

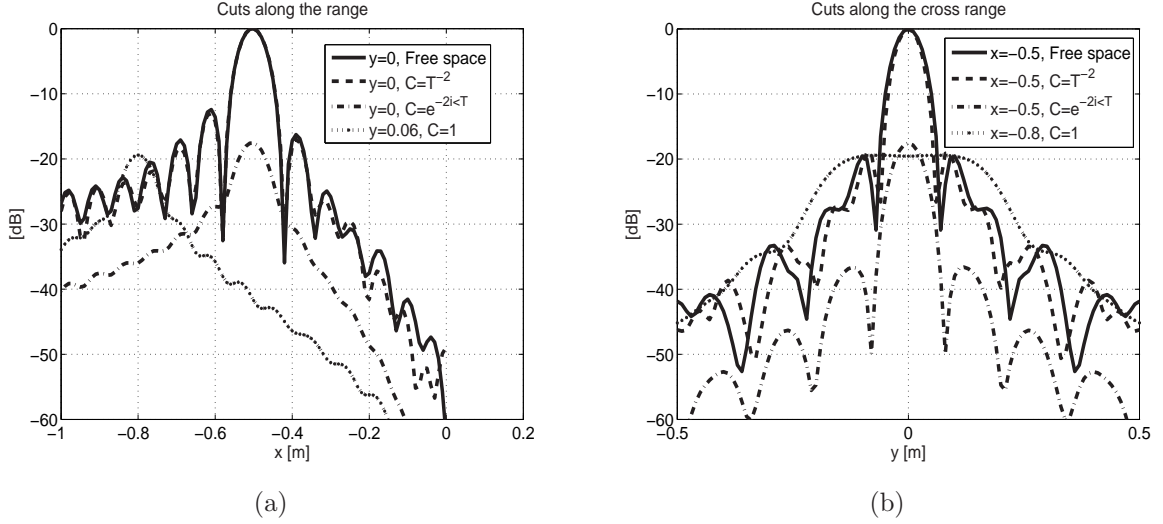


Figure 5.3: (a) Point spread functions along the range and (b) along the cross-range. Solid line (-) is for the target image when there is no wall, dashed line(- -) is for the target image behind the wall when  $C = T^{-2}$ , dash-dotted line (-·-) is for that when  $C = e^{-2i\angle T}$ , and dotted line (· ·) is for the target image behind the wall when no compensation is performed,  $C = 1$ .

An important issue of interest is determination of the sensitivity of the compensation process to the permittivity and the thickness of the wall. That is how the compensated images would differ if the permittivity and/or the thickness, used to compute the compensation factors, are not exactly the same as those of the wall, under the test. This can be quantified using a factor, referred to as the squared error, defined by

$$SE = \sum_{p=1}^P \sum_{q=1}^Q (I(x_p, y_q) - I_0(x_p, y_q))^2, \quad (5.8)$$

where  $P$  and  $Q$  are the number of pixels defining a rectangular box around the target. Here  $I$  and  $I_0$  are the normalized intensity of the target images, respectively for the compensated target image, and for an ideal case where there is no wall in place (e.g.  $I =$

$$|\tilde{S}^c(x_p, y_q)|^2 / \max |\tilde{S}^c|^2).$$

For the example considered here, a  $1\text{m} \times 1\text{m}$  square, centered at  $(-0.5, 0)$ , is considered as the expected target image area containing 10201 pixels (i.e.  $P=Q=101$ ). For different searched parameters (wall permittivity  $\epsilon_{rp}$  and wall thickness  $d_p$ ),  $SE$  is computed and shown in Fig.5.4. Here, only the real part of the relative dielectric constant is changing assuming the imaginary part is 0.3 (i.e.  $\epsilon_{rp} = \epsilon'_{rp} + i 0.3$ ). Figures 5.4(a) and (b) show the squared errors computed for full compensation ( $C = T^{-2}$ ) and phase compensation ( $C = e^{-2i\angle T}$ ), respectively. It is observed that both methods can effectively refocus the target image with the minimum  $SE$  when the excess electrical length  $d_p(\sqrt{\epsilon'_{rp}} - 1)$  is approximately equal to 0.3 ( $0.3(\sqrt{4} - 1)$ ). This is because according to (7.18) the phase of a transmission coefficient is approximately equal to that of  $e^{i(k_{1x} - k_{0x})d}$ , proportional to  $d(\sqrt{\epsilon'_r} - 1)$ . Simulations show that minimization of  $SE$  is not affected by the accurate knowledge of  $\epsilon''_r$ . For example choosing imaginary part of 0.2 instead of 0.3, minimization of SE resulted in the exact excess electrical length of the wall.

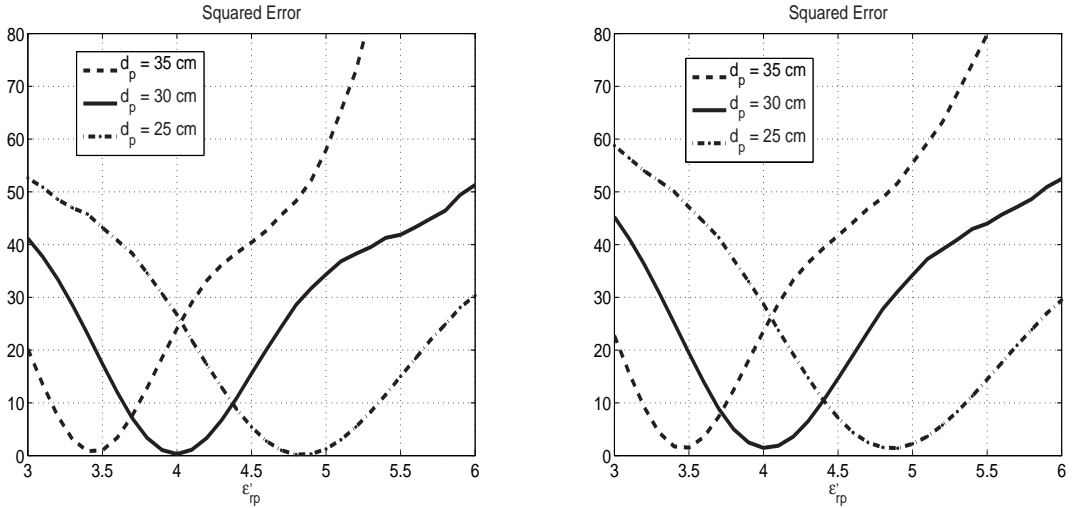


Figure 5.4: Squared errors of the point target image. The images are compensated for (a) the magnitude and phase ( $C = T^{-2}$ ) and (b) only phase ( $C = e^{-2i\angle T}$ ) of the transmissivity. The  $SE$ 's are provided as functions of real parts of permittivity  $\epsilon'_{rp}$ , assuming the imaginary part is 0.3 and for different wall thicknesses  $d_p$ .

### 5.2.3 Application of refocusing method in practice

In practice, the location of the target in the image area is unknown. In this case, for a given intensity  $I$  the minimum of  $SE$  is searched for different permittivity and thickness of the wall and different target positions within the image area. For the example given above, the minimum of  $SE$  is achieved for the exact location of the target and wall's excess electrical length,  $d(\sqrt{\epsilon'_r} - 1)$ .

It is noted that, the refocusing technique is applied on the point target image area only. Let us suppose that the image area has  $N_d$  pixels. Then to apply the refocusing algorithm, the number of computations of transmissivity is proportional to  $N_p N_f N_d$ , where  $N_p$  and  $N_f$  are the number of incidence angles (i.e. number of antenna positions) and frequency points, respectively. Since transmissivities through homogeneous walls are smooth functions of incident angle and frequency, they can be computed *a priori* and stored in a lookup table. This way, the number of calling of transmissivity is proportional to  $N_d$  and the refocusing is performed faster.

For example, to obtain refocused image of Fig.5.2(b) having  $N_p=61$ ,  $N_f=161$ , and  $N_d=10201$ , about 6 minutes run-time is required using an AMD Athlon processor with 1 GB random access memory (RAM) and 2 GHz central processing unit (CPU). On the other hand, by employing a lookup table of transmission coefficients stored for 0-90 incident angles with 1 degree spacing and 1-3 GHz frequency band with 12.5 MHz spacing the running time is reduced to less than a minute.

In the optimization algorithm for minimization of  $SE$ , first the target image is compensated for different excess electric length and then compared with images of an ideal point target located at different positions. Fig.5.5 shows the  $SE$  as a function of  $\epsilon'_{rp}$  and target position  $x_s$  computed for wall thickness of 30 cm. As shown, both the position of the target and excess electrical length are found successfully. The running time for this process depends on the total number of searched parameters  $\epsilon'_{rp}$  and  $x_s$ . Here,  $\epsilon'_{rp}$  and  $x_s$  are discretized with increments of 0.5 and 5 cm, respectively and running time is less than 5 minutes.

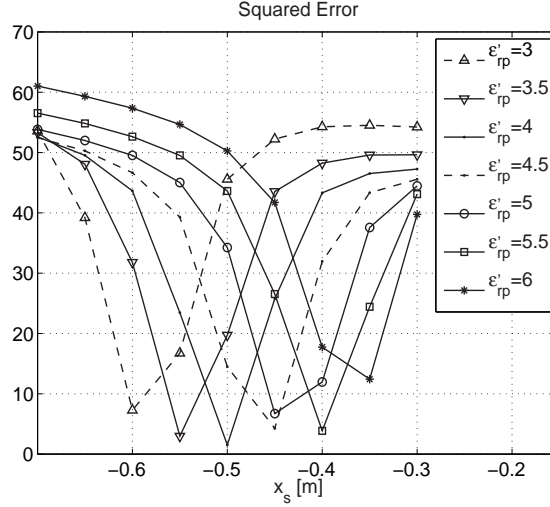


Figure 5.5: Squared error of the point target image as a function of  $\epsilon'_{rp}$  and target position  $x_s$  computed for wall thickness of 30 cm. The target image is compensated for the phase of transmissivity ( $C = e^{-2i\angle T}$ ).

### 5.3 Experimental Study

To demonstrate the effectiveness of the refocusing approach, we examine the method through an experimental study. The measurement setup consists of an HP8753D Vector Network Analyzer (VNA), two double-ridge horn antennas operating from 1 GHz up to 18 GHz, an XY-table along with a control unit (CU), and a personal computer (PC). A wall composed of 78 poured concrete blocks is made on top of a layer of cinder blocks inside the laboratory (see Fig.5.6(a)). The size of each block is about 19.5 cm  $\times$  39.5 cm  $\times$  9.2 cm. The wall is arranged by making 6 blocks in width and maximum of 13 blocks in height. The underlying cinder block layer is used to place the antennas at approximately the middle of the concrete block wall. The overall size of the wall is about 2.37 m in width and 1.77 m in height. Fig.5.6 shows the side view and the schematic of the measurement setup.

Instead of using one port measurement, employing one antenna, two antennas are used. This way the strong reflected signal from the antenna port is eliminated. The two identical double-ridge horn antennas, one for transmitting and one for receiving are connected to the VNA, and S12 is measured. The vertically aligned antennas are mounted on a vertical wooden rod (along the  $z$  axis) attached to the carriage of the XY table. As shown in Fig. 5.6,

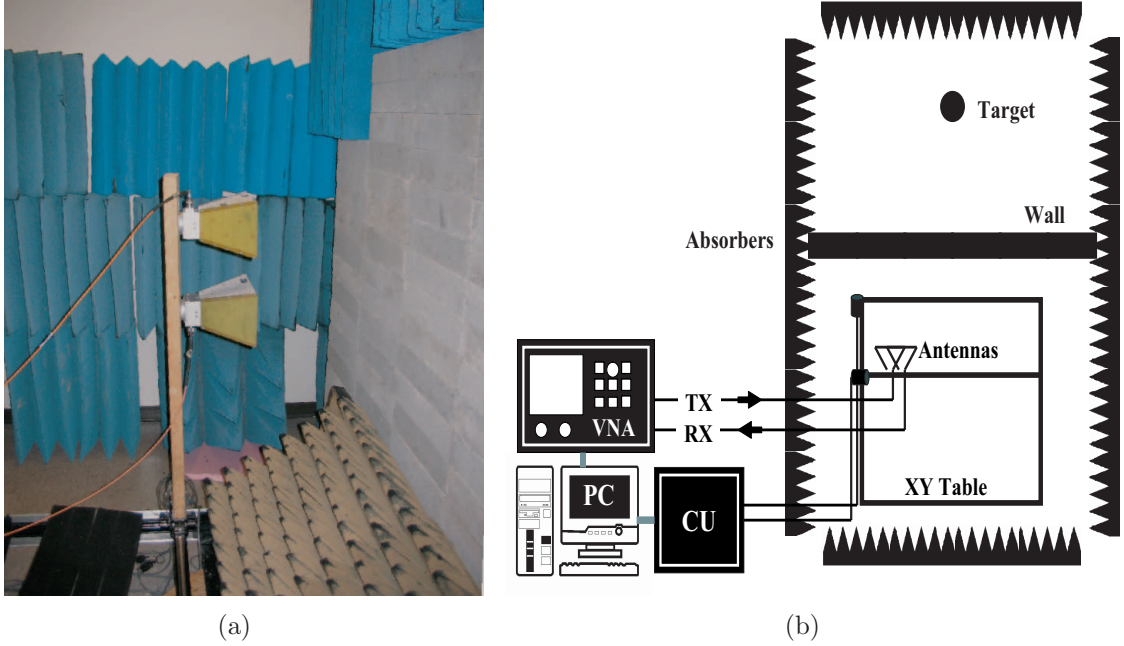


Figure 5.6: (a) Side view and (b) schematic of the measurement setup.

microwave absorbers are put around the measurement setup and on the top of the wall. The reasons for the absorbers are to reduce the multi-path in the small laboratory environment. The absorbers on the top are to eliminate the edge diffraction from the wall top and reflected fields from the ceiling.

In the following subsections calibration of the system, the estimation of the relative dielectric constant of the concrete blocks, and the refocusing of the target image is described.

### 5.3.1 Calibration

The radar system must be calibrated to remove the systematic errors such as uneven frequency responses of the VNA, the cables, and the antennas. Calibration is performed by placing an electrically large metallic plate on the wall, exactly in front of the transceiver. For this scenario S12 measurement is performed, and the frequency response,  $A_R(k_m)$ , is recorded. Since the reflection from the plate is significantly stronger than the leakage from the transmitting antenna to the receiving antenna, the recorded signal consists almost of response of the antennas and the free-space path loss. The leakage and the multiple-bounce between the antennas and the plate can also be gated out in the time domain. Denoting

the uncalibrated backscattering from the targets by  $E_r^{nc}$ , the calibrated data  $E_r^c$  is computed from

$$E_r^c(\bar{r}_n, k_m) = \frac{E_r^{nc}(\bar{r}_n, k_m)}{A_R(k_m) e^{-2ik_m \sqrt{D_W^2 + (D_A/2)^2}}}, \quad (5.9)$$

where  $D_W$  is the distance from the outer aperture of the antennas to the wall, and  $D_A$  is the center-to-center separation between the two antennas.

### 5.3.2 Measurement of the relative dielectric constant of the concrete wall

Concrete blocks are composed of cement, aggregates (i.e. sand and fine gravel), water, and air. The measured properties of the concrete mixes constituting different plain concrete blocks are tabulated in [92]. Nominal ratios of water and aggregates to cement in weight are 0.4-0.6 and 2.7-6.5, respectively. Volumetric air content is 1 to 2% and size of the voids inside concretes is on order of a millimeter. Since the size of inhomogeneities is small, homogeneous dielectric slab models can reasonably predict the transmission and reflection coefficient properties of the walls up to relatively high frequencies [93]. The relative dielectric constant of concrete as a function of porosity and moisture content can be found in [94].

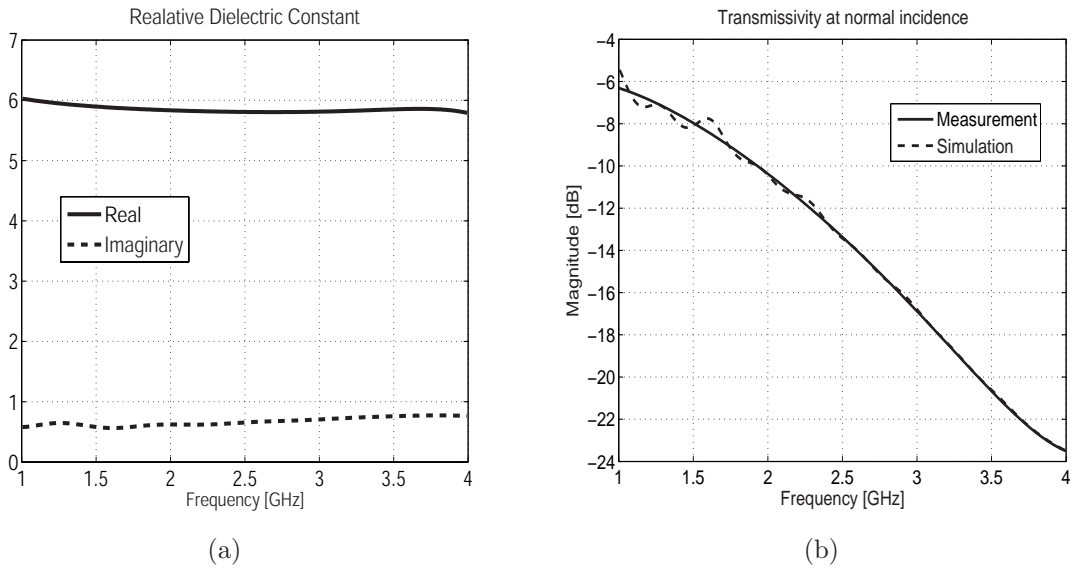


Figure 5.7: (a) The relative dielectric constant of concrete blocks as a function of frequency and (b) transmissivity through the concrete wall at normal incident angle.

To estimate the relative dielectric constant of the wall, the transmissivity of the wall is measured [95]. In this measurement, the two double-ridge horn antennas are placed on different sides of the wall and at the same height (1.28 m). Two S12 measurements are performed, one with and one without the wall. For both measurements the setup, locations of antennas and cables, are all kept the same.

To eliminate multi-path effect, the time domain responses are generated and the desired direct signals are time gated. This is to extract only the direct ray which is propagating through the wall. Then, the gated signals are transferred back to frequency domain. The frequency domain signals are divided to achieve the transmissivity. The measured transmissivity must be compared with the transmission coefficient of a dielectric slab at normal incidence. The computation of permittivity as a function of frequency is performed using [95]:

$$\begin{aligned}\epsilon_r' &\simeq [1 + \frac{c}{2\pi d} \frac{d}{df} \angle t_m(f)]^2 \\ \epsilon_r'' &\simeq \frac{2\alpha \sqrt{\epsilon_r'}}{k_0},\end{aligned}\tag{5.10}$$

where  $\alpha$  is

$$\alpha = \frac{1}{2d} \ln \left[ \frac{\frac{16}{|t_m(f)|^2} + 2 \cos(k_0 \sqrt{\epsilon_r'} d) \frac{(\epsilon_r' - 1)^2}{\epsilon_r'}}{(\sqrt{\epsilon_r'} + 1)^4 \epsilon_r'} \right].\tag{5.11}$$

Here,  $|t_m(f)|$  and  $\angle t_m(f)$  are the magnitude and the phase of the measured transmissivity as a function of frequency respectively, and  $k_0$  is the propagation constant. Equations (5.10) and (5.11) are applicable, assuming that  $\epsilon_r''/\epsilon_r' \ll 1$  and  $e^{-2\alpha d} \ll 1$ , [95]. The results are illustrated in Fig. 5.7(a). The average value over the frequency band is about  $5.9 + i 0.7$ . The measured and simulated values of transmissivity are compared in Fig. 5.7(b) where close agreement is shown. Permittivity values of concretes with different moisture contents as functions of frequency are measured in [96], using an open-ended coaxial probe method. Accordingly, the concrete blocks in this measurement are in a state between saturated and air dried conditions.

### 5.3.3 Refocusing

To demonstrate refocusing experimentally a small trihedral corner reflector, with pentagonal panel geometry is used as a point target behind the wall [77]. The target and its approximate sizes are shown in Fig.5.8 (a). The back corner of the trihedral (scattering phase center) is at  $x = -0.71$  m and at the same height as that of the receiver antenna, 1.28 m above the ground plane. The transmitting and receiving antennas are on the other side of the wall, mounted on a vertical wooden rod and moving along a scan line with length  $L = 95.88$  cm. The transmitting antenna is attached about  $D_A = 0.25$  m below the receiving antenna on the wooden rod. The apertures of both antennas are about  $D_W = 0.45$  m away from the wall. The frequency of operation is from 1-2.5 GHz, the step frequency is 12.5 MHz, and the transceiver moves along the scan line with spacing of 2.04 cm. It is noted that the antennas are in the far-field region of the target.

In a stepped-frequency radar system, the signal at the receiver antenna is mainly composed of two parts, (1) backscattering of the target and (2) reflection from the wall. To reduce the effect of reflection from the wall, background subtraction can be performed. That is two measurements are employed, one with presence of the target and one without the target. By subtracting the received data, the effect of direct reflection from the wall is decreased.

Using standard SAR imaging, the normalized target image is shown in Fig. 5.8(b). To compare the target image and its ideal image another measurement is performed when the wall is removed. The normalized target image is illustrated in Fig.5.9(a). By comparing the two figures, Fig.5.8(b) and Fig.5.9(a), it is obvious that the standard target imaging locates the target further back from its actual position and the cross-range resolution is significantly decreased. The image, Fig.5.8(b), is compensated for the effect of the wall using only the phase of transmission coefficients and the result is shown in Fig.5.9(b) which is similar to Fig.5.9(a). Compensation by  $C = T^{-2}$  has as good performance as the one in Fig.5.9(b). The patterns along the azimuth and range directions are plotted in Fig.5.10. The compensated image is in close agreement with the target image when there is no wall, or equivalently very close to the point spread functions along the range and along the azimuth. The small

discrepancies between the two patterns are due to residual multi-path and imperfections in the calibration process.

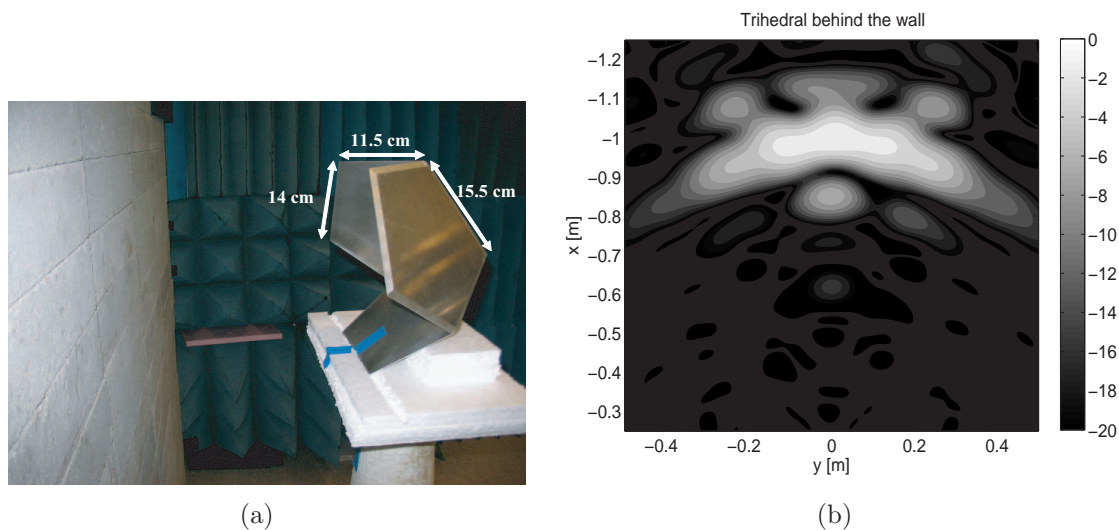


Figure 5.8: (a) The trihedral corner reflector, used as a target behind the wall and (b) its normalized image using the standard SAR imaging.

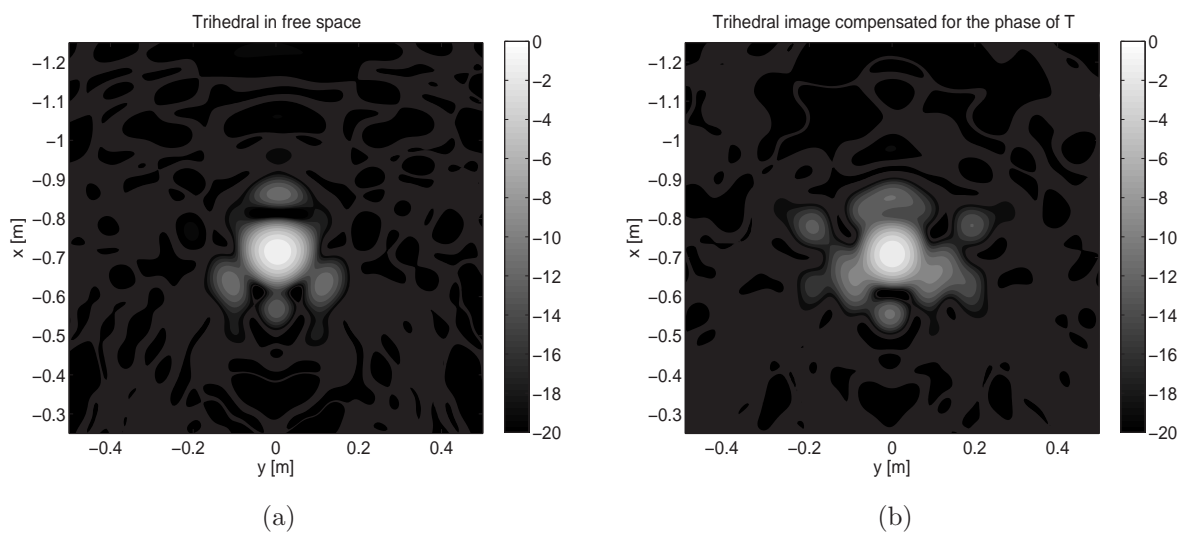


Figure 5.9: (a) The normalized image of the trihedral when there is no wall and (b) the normalized SAR image of the trihedral behind the wall, when the image is compensated for the effect of the wall.

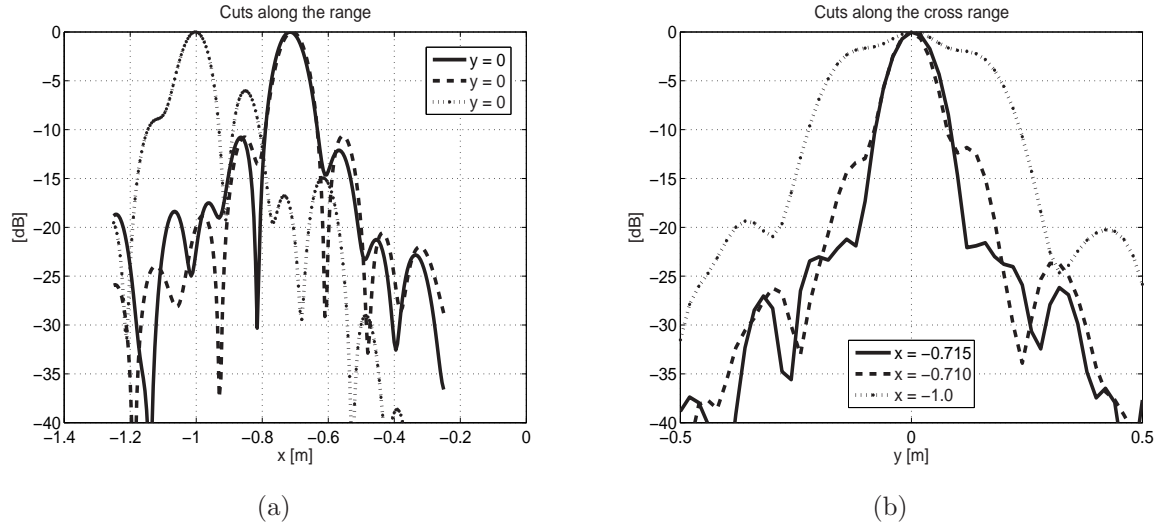


Figure 5.10: (a) Cuts of target images along the range and (b) along the cross-range. Solid line (-) is for the target image when there is no wall, dashed line (- -) is for the target behind the wall when the pattern is compensated, and the dotted line ( $\cdots$ ) is for the target behind the wall, imaged by standard SAR imaging.

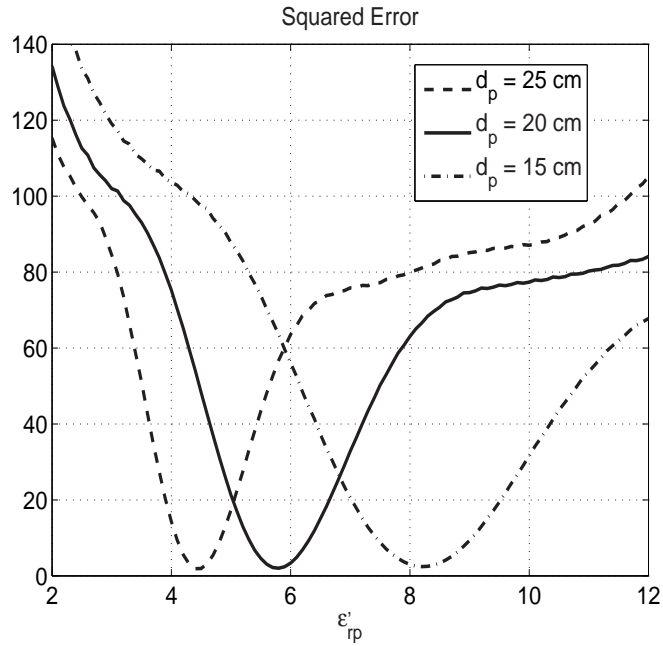


Figure 5.11: Squared error of the trihedral image using the experimental data. The  $SE$ 's are provided as functions of real part of permittivity  $\epsilon'_{rp}$  assuming a fixed imaginary part of 0.7 and for different wall thickness values ( $d_p$ ). The image of the trihedral is compensated for the phase of the transmissivity (i.e.  $C = e^{-2i\angle T}$ ).

The measurement data is used to compute the squared error of the trihedral image and the results are shown in Fig.5.11. In this figure,  $SE$  plots are provided as functions of real part of permittivity assuming a fixed imaginary part of  $\epsilon''_{rp}=0.7$  and for different wall thickness values ( $d_p$ ). In the computation of  $SE$ , we assumed that the response of the target behind wall is unknown and therefore in (5.8)  $I_0$  is the normalized intensity of a point target image with scattering matrix of unity and  $I$  is the normalized intensity of the trihedral obtained from the measurement. As clearly shown in Fig. 5.11, the  $SE$ 's are minimum at points where the excess electrical length is equal to that of the wall, about 27.8 cm.

To examine the effect of reflected signal from the wall on the target image, an image is constructed using total received signal, shown in Fig. 5.12(a). Here, in addition to the target the wall is also imaged. The wall is primarily imaged as two parallel lines showing the front and the back boundaries. In comparison, if the Fourier Transform of a reflection from a dielectric slab is taken, two peaks are observed in the time domain data. The first peak is due to the front boundary and the second peak is due to the boundary in the back. The distance between the two peaks should be approximately equal to the electrical length of the wall (i.e.  $d\sqrt{\epsilon'_r}$  at normal incidence) which in this case is  $19.5\sqrt{5.9} \approx 47$  cm. From Fig. 5.12(a), this distance is about 46 cm.

Since backscatter from the wall is very strong the sidelobes generated by image formation spills over into desired image domain manifested as multiple lines parallel to the wall surfaces. The image after compensation for the effect of transmission through the wall using  $C = e^{-2iZT}$  is shown in Fig.5.12(b). Although the cross-range resolution of the target is regained, existence of the wall sidelobes in the image is still evident. In cases where the scattering from targets is small compared to the reflection from the wall or other clutters in the scene, the detection of targets is difficult. Therefore, in order to increase the signal-to-clutter ratio the reflected signal from the wall must be estimated and subtracted.

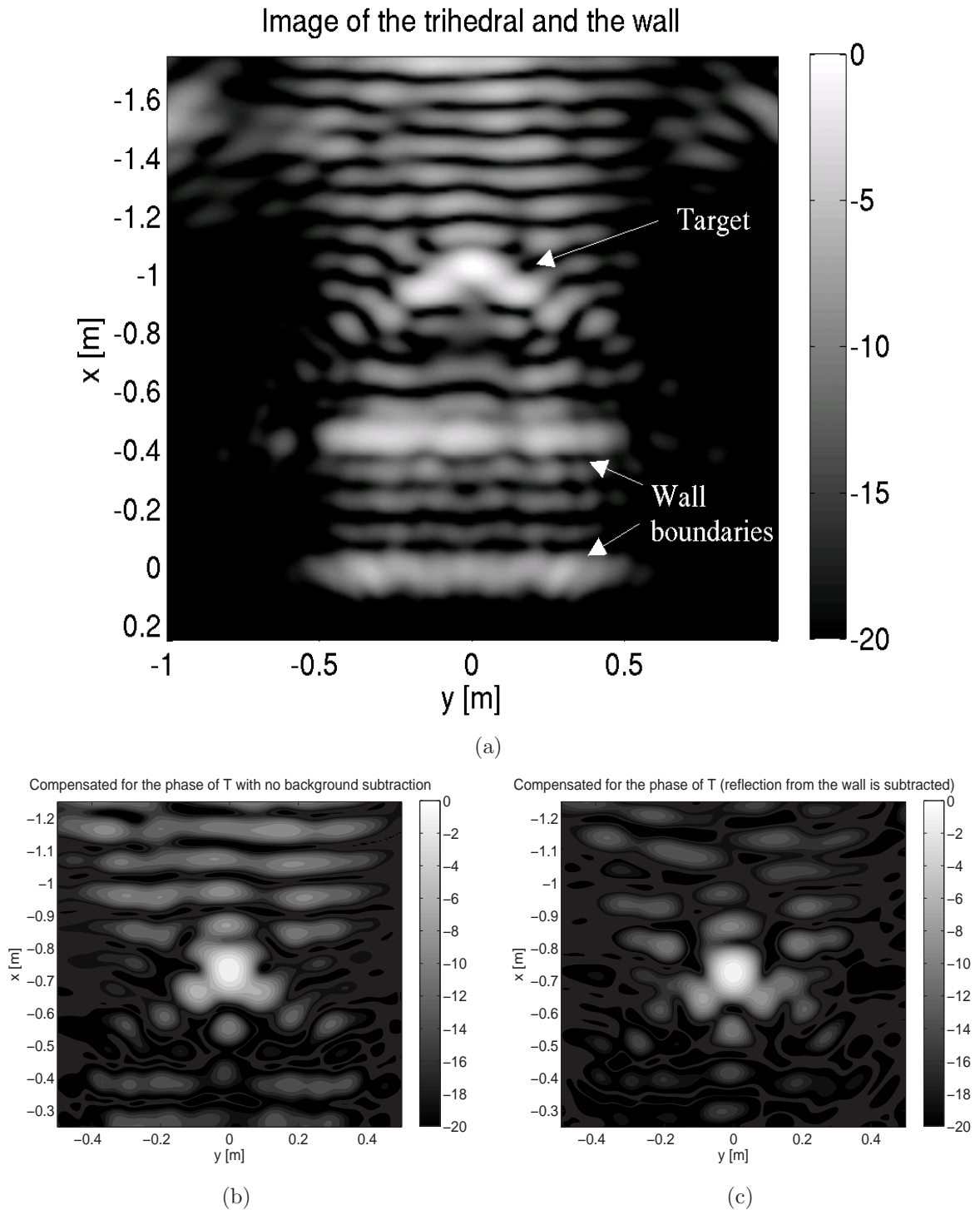


Figure 5.12: (a) The experimental image of the trihedral behind wall, using total received signal. (b) Compensated image using  $C = e^{-2i\angle T}$ . (c) First total received signal is subtracted from analytically computed reflected fields. Next compensated image using  $C = e^{-2i\angle T}$  is calculated.

The wall parameters are first estimated from the time domain backscatter at a given location. Basically, the response of the wall is gated from the total backscatter signal and transferred into the frequency domain. The mean squared error between the calculated reflection coefficient  $\gamma$  computed by (7.18) and the measured reflection coefficient  $\gamma_m$ , given by

$$\delta = \frac{1}{N_f} \sum_{n=1}^{N_f} |\gamma_m(f_n) - \gamma(f_n)|^2 \quad (5.12)$$

is computed and its minimum is searched for the wall thickness and permittivity [97]. Using the measured reflection coefficients, the minimum of  $\delta$  is obtained for wall thickness of 20 cm and permittivity of  $5.7 + i 0.6$ . These results are in close agreement with the wall parameters obtained by transmission measurement shown in Fig. 5.7(a). Next, the wall reflection is computed analytically using (5.4) and subtracted from the total received signal. The resulting image is shown in Fig.5.12(c). By comparing Fig.5.12(b) and (c) a substantial improvement in clutter rejection is observed. The *SE* of both images over the image area of  $1 \text{ m}^2$  is computed. In comparison, the *SE* of Fig.5.12(c) is by a factor of 3 smaller than that of Fig.5.12(b).

Using the same setup, another experiment is performed employing two trihedral corner reflectors with the same radar cross sections (see Fig.5.13 (a)). The back corner of both targets are placed at  $x = -0.71 \text{ m}$ . One trihedral is at  $y = -0.14 \text{ m}$ , and the other is at  $y = 0.14 \text{ m}$ . The image of this scene is constructed over a frequency band of 1-2.5 GHz, using standard SAR imaging, and the result is shown in Fig.5.13(b). It is observed that the point-spread function distortion caused by the wall merges the responses of the two targets. The refocusing processes once using  $C = T^{-2}$  and once using  $C = e^{-2i\angle T}$  are performed and the normalized target images are shown in Fig. (5.14) (b) and (c), respectively. As illustrated with both compensation methods the two targets can now be easily discerned. These results are shown with background subtracted. The refocusing processes are also applied on the images obtained without background subtraction and the two targets are clearly detected. The targets' images can also be compared with the one when there was no wall in place, shown in Fig. 5.14(a). It is observed that the patterns are similar. The cuts along the azimuth and range directions are plotted in Fig.5.15. Here the compensated image

using  $C = T^{-2}$  is compared with the target image obtained when there is no wall and good agreement is shown. The compensated image employing  $C = e^{-2i\angle T}$  also provides almost the same resolution. However, for the cuts along the cross-range, the sidelobe in between the two targets is about 2 dB higher than that when  $C = T^{-2}$  is employed.

To enhance the cross-range resolution a dual-bandwidth imaging method is used. It was noted that for an ultra-wideband system cross-range resolution is approximately proportional to  $\lambda_m/L$ , where  $\lambda_m$  is the mean wavelength across the band and  $L$  is the length of synthetic aperture. This assumes that the backscatter response of point targets is uniform with frequency. For the problem at hand, the two-way attenuation at higher portion of the spectrum creates a non-uniform spectral response. As a result the cross-range resolution, dominated by the lower frequency content of backscatter, is coarser than the expected resolution. However, this image has a high signal-to-noise (S/N) ratio and very low side-lobe level for its point spread function on both range and cross-range directions. Formation of an image using the high portion of the spectrum can provide fine cross-range resolution, but due to poor S/N sidelobes can be high and image looks noisy. The product of these two images will provide fine resolution around the point targets and suppress sidelobes and false targets of the high-band image.

One image is formed with operation frequency of 1-3 GHz and the other with operation frequency of 2.95-3 GHz and then multiplied together and the result is shown in Fig.5.16(a). The highest portion of the frequency band with a minimal bandwidth (2.95-3 GHz) is chosen to achieve the highest possible cross-range resolution. As shown in Fig.5.16(a), the images of the two adjacent trihedrals are quite distinct. A comparison is made between Fig.5.16(a) and a second image, obtained by multiplying the image achieved using the entire frequency band (i.e. 1-3 GHz) by itself. The cuts along the cross-range of first and second images are compared in Fig.5.16(b). It is observed that the 6 dB cross-range resolution of the first image is on average about 15% narrower than that of the second image.

### 5.3.4 Discussion on the modeling and future application of the refocusing method

Generally, backscattered fields from a target caused by multi-path (reflection from ground and/or ceiling) are imaged at different ranges and their magnitudes are less than that of the direct backscattered signal received from the target itself. Specific techniques can be used to further reduce the contributions from multi-path caused by the reflection from the ground and ceiling. For example a vertical array can be considered that can narrow the beam in vertical direction. Other methods such as SAR interferometry along vertical direction can be used to identify elevation of scatterers. In this chapter, however, the emphasis is placed on refocusing through walls as a first step to sharpen point target images and reduce the multi-path caused by walls.

An example showing a possible application of the refocusing technique is described below. Let us consider that the target is inside a building structure composed of multiple parallel walls. The following steps are suggested to refocus the image. From the standard SAR imaging, the map of the building is roughly estimated. The front wall is recognized and using the procedure discussed in subsection C the direct reflection from the wall is gated and its parameters  $(d, \epsilon_r)$  are estimated. Once the wall is characterized, its reflection is analytically computed and subtracted from the total signal and then compensating for the effect of transmission, the interior of the building is imaged. The new image can go through the same process to refocus through the subsequent wall structures.

## 5.4 Conclusions

SAR technique is used to image targets behind the walls. For high resolution images ultra-wideband antennas and wide incidence angles are required. Since the transmissivity of the wall is a function of both frequency and incident angles, the effect of the wall on the target image becomes significant. Basically the cross-range resolution is degraded if standard SAR imaging is applied. Instead a refocusing approach has been applied to remove the effect of the wall, and the target image is sharpened. It is shown that extraction of the

wall parameters and coherent subtraction of the wall reflection can significantly improve the signal-to-clutter ratio. Also cross-range resolution is improved by re-using the high frequency portion of the backscatter spectra where the synthetic aperture length is much larger than the wavelength.

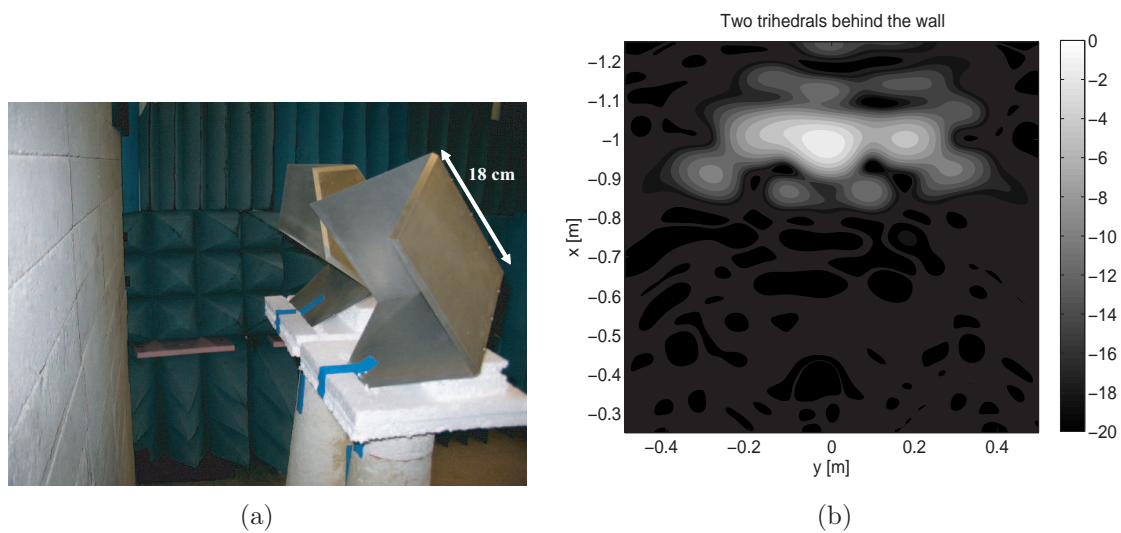


Figure 5.13: (a) Two corner reflectors behind the wall and (b) their normalized image using the standard SAR imaging.

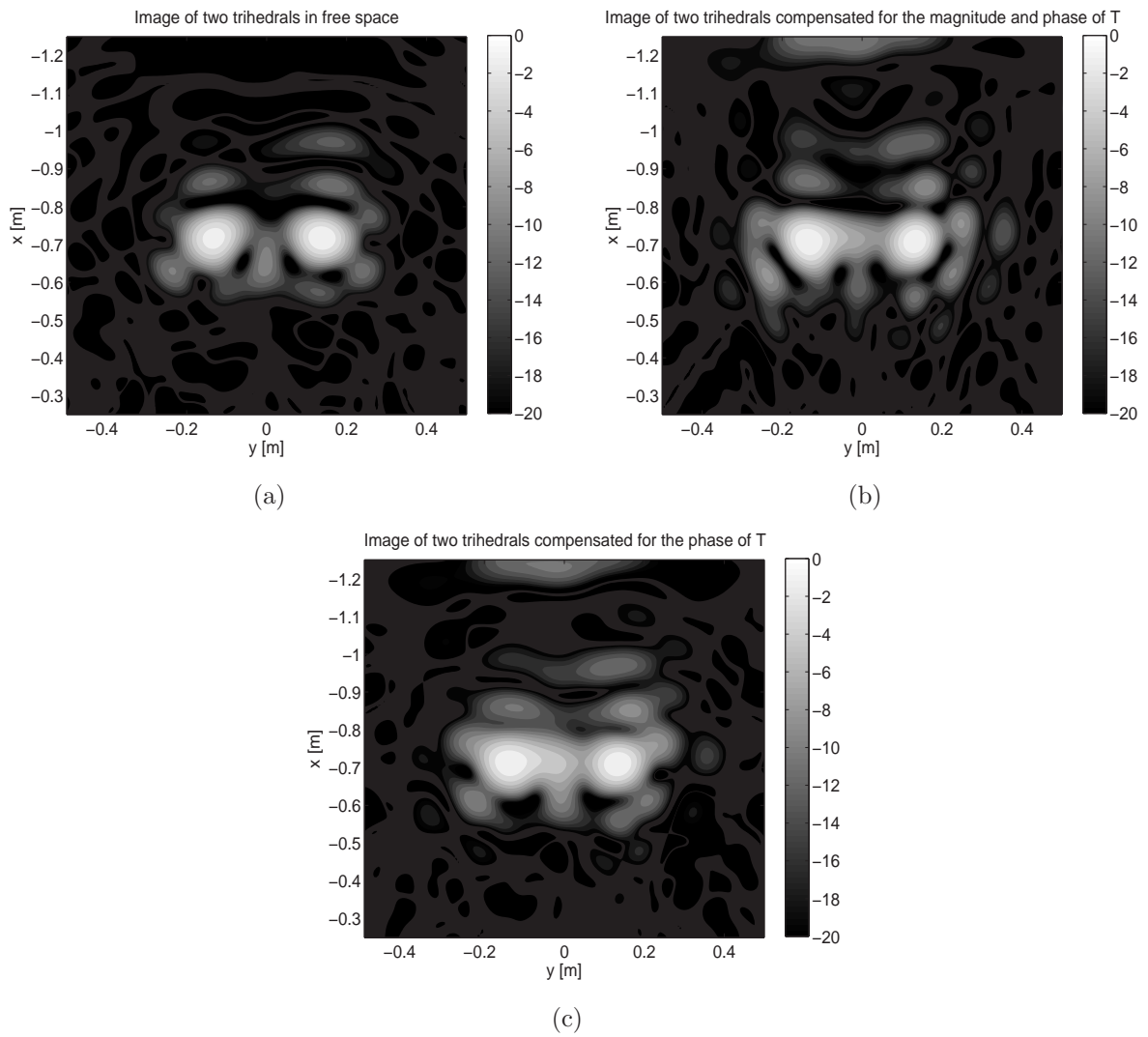


Figure 5.14: (a) Two trihedral corner reflectors when there is no wall in place, and their images when the wall is built: (b) compensated image using both magnitude and phase, and (c) compensated image employing only the phase of transmissivity.

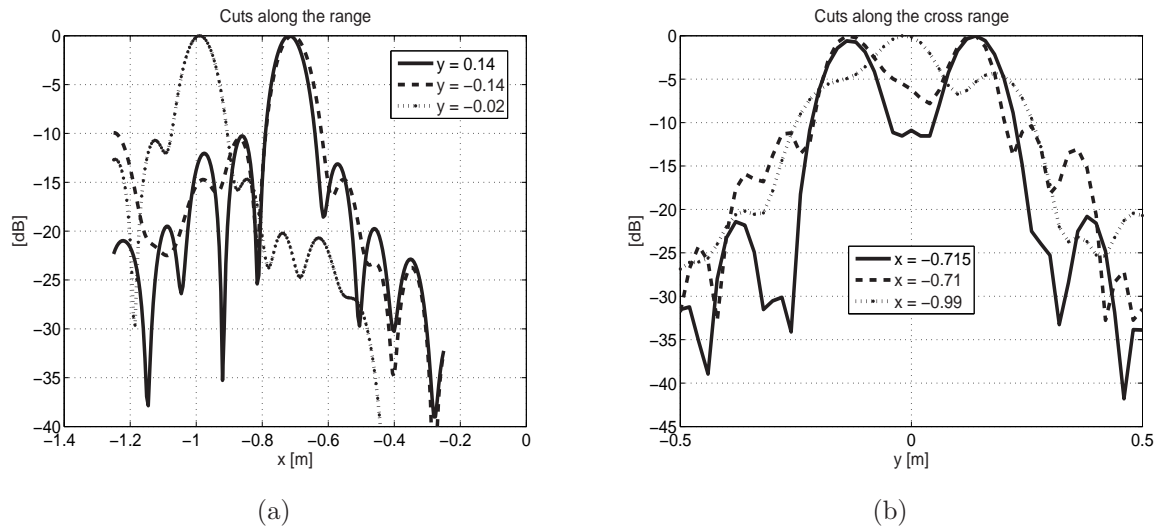


Figure 5.15: (a) Cuts of images along the range and (b) along the cross-range. Solid line (-) is for the two trihedrals image when there is no wall, dashed line (- -) is for the targets behind the wall when the pattern is compensated by  $C = T^{-2}$ , and the dotted line ( $\cdots$ ) is for the targets behind the wall, computed by standard SAR imaging.

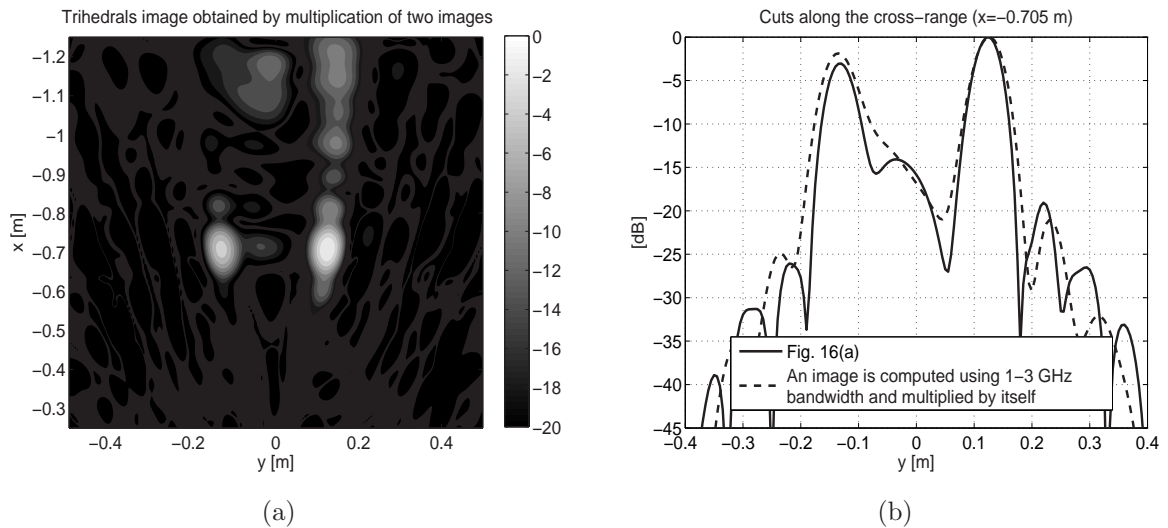


Figure 5.16: (a) Image of two trihedral corner reflectors. Multiplication of two images: one is performed over frequency band of 1-3 GHz, and the other computed for frequency band of 2.95-3 GHz. (b) An image is performed using the entire frequency band (1-3 GHz) and multiplied by itself. The cuts along the cross-range of this image and that of the figure (a) at the range of -0.705 m are compared. All the images are compensated by  $C = T^{-2}$ .

## CHAPTER 6

# Hybrid FDTD and Ray-Optics Approximation for Simulation of Through-Wall Microwave Imaging

### 6.1 Introduction

Imaging through building walls with reasonable target resolutions can be accomplished at microwave frequencies and lower. For instance transient Impulse Synthetic Aperture Radar (ImpSAR) systems, operating at 250-3500 MHz, are capable of imaging targets behind walls from a large distance, with resolutions less than ten centimeters. Unlike free-space imaging, image formation through inhomogeneous building walls is not a straight forward process. The interaction of electromagnetic waves with various types of walls, e.g. cinder block, adobe, brick, etc., with different geometrical and material properties can significantly defocus a target image and even create multiple image points due to the presence of multi-path and Bragg modes. In this chapter we examine phenomenology of the near-field microwave imaging through cinder block walls. A hybrid FDTD numerical technique and Physical Optics (PO) approximation in conjunction with phase conjugation method is used, for computation of transmitted field through different walls and image formation. Numerical results, delineating features of wideband and wide angle wave propagation and imaging through walls are presented.

## 6.2 Theoretical Model

Cinder block or even a homogenous poured concrete wall can be viewed as a periodic structure, composed of a large number of dielectric blocks. Fig. 6.1 shows a cinder block wall as an example, where the building blocks are periodically arranged in the  $y$  and  $z$  directions. The wall is illuminated by a field radiated from antenna placed at a distance from the wall so that the wall is in its far-field region. If the antenna is also located in the far-field region of each block the incident field on each block is approximated locally by a plane wave proportional to the ray emanated from the transmitter antenna. In this case, the radiated field can be viewed as a set of rays. The fields inside each block is then approximated as if it was located inside an infinite structure of periodic blocks illuminated by a plane wave. This approximation is valid when the blocks are sufficiently away from the antenna and/or the blocks are sufficiently small. Using this assumption, the field  $\bar{E}$  inside each block, is computed for an incident wave propagating along  $\hat{k}_i$ , where  $\hat{k}_i$  is the unit vector directed from the antenna location to the center of the block in the  $y$ - $z$  plane. Replacing the dielectric wall with polarization current given by

$$\bar{J} = -ik_0 Y_0 (\epsilon_r - 1) \bar{E} \quad (6.1)$$

where  $k_0$  is propagation constant of free space,  $Y_0$  is the characteristic admittance of free space, and  $\epsilon_r$  is the relative dielectric constant of the building material, the scattered field can be computed. Having the equivalent current at discretized points inside each block the scatter field at the observation line can be obtained using the far-field expression of the dyadic Green's function  $\bar{\bar{G}}(\bar{r}, \bar{r}')$ . Finally, the total scattered field  $\bar{E}_s(\bar{r})$  is expressed as a sum of scattering contributions from all blocks and is given by

$$\bar{E}_s(\bar{r}) = ik_0 Z_0 \sum_{n=1}^N \sum_{m=1}^M \int \bar{J}_{m,n}(\bar{r}') \cdot \bar{\bar{G}}(\bar{r}, \bar{r}') d\bar{r}' \quad (6.2)$$

where  $M$  and  $N$  are the number of blocks in  $y$  and  $z$  directions, respectively. Evaluating (6.2) numerically, the computation of scattering at the observation points in the near-field of the wall is possible.

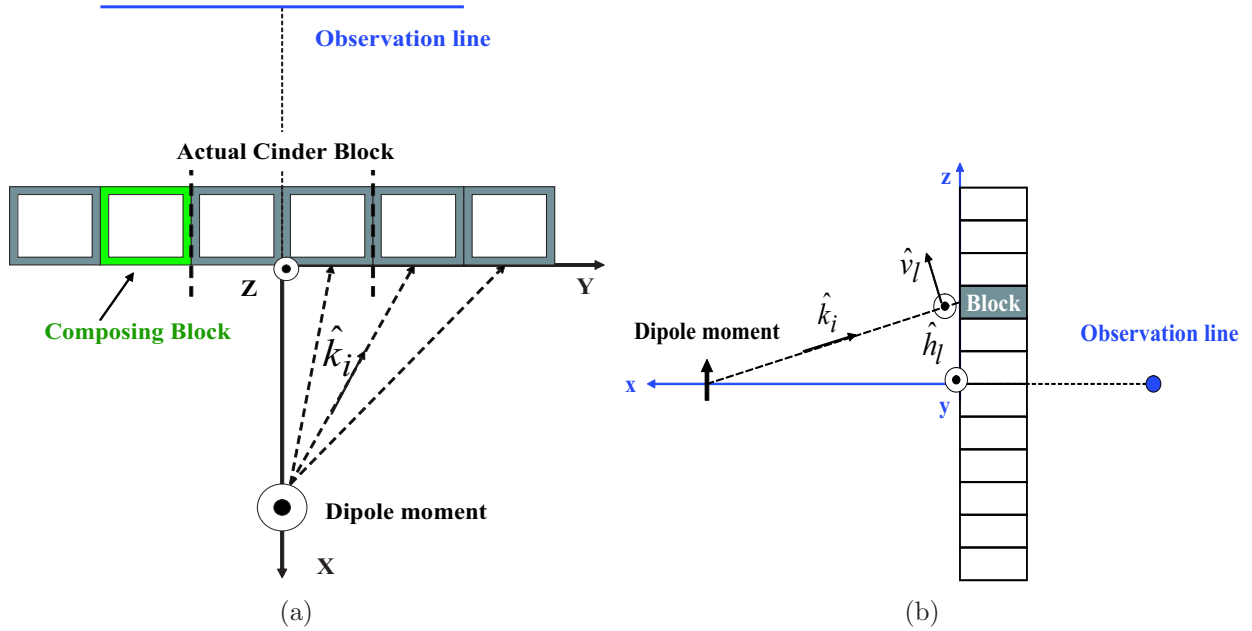


Figure 6.1: Emanating fields from transmitter antenna is considered as a set of rays incident to the wall. One ray is considered for each composing block, assuming the incident field is locally plane wave for that block. (a) top view (b) side view.

Depending on the wall structure, different geometries can be prescribed for the building blocks. For example for concrete, brick, and adobe walls the building block is modeled by a solid dielectric block, whereas for cinder block walls and interior walls made of dry wall and studs, a more complex geometry shown in Fig. 6.1(a) is used as a building block. For solid blocks, the expression for the internal fields can be approximated with the ones inside an infinite dielectric slab which can be derived analytically. The mathematical formulation can be found for example in [98] and [55]. In this technique the incident field  $\bar{E}_i$  is first decomposed into transverse electric and transverse magnetic components, locally defined for each block (see Fig. 6.1(b)). Then the internal fields are expressed in terms of the Fresnel reflection coefficients from a dielectric slab. On the other hand, the computation of the fields inside the cinder blocks is performed numerically using FDTD technique [67]. For computation of the fields inside each block the periodic boundary conditions are applied where the block is assumed to be located inside an infinite periodic structure. Using proper time steps, and time delays the fields inside each block are transferred from the time domain into the frequency domain using the Fourier transform. Since the incident field is differentiated Gaussian pulse,

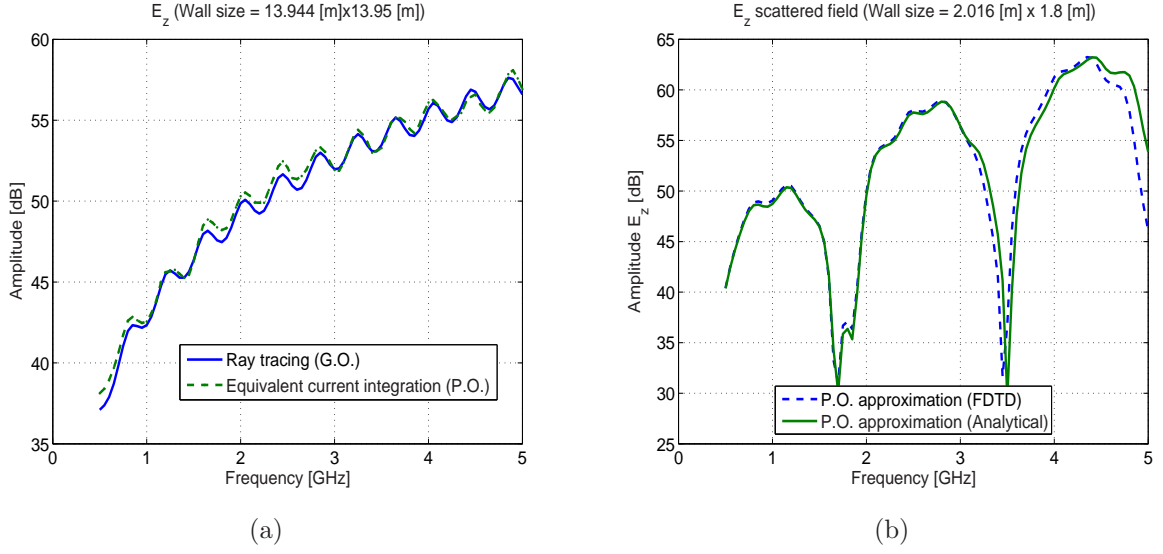


Figure 6.2: Comparison of (a) total propagated field through a solid wall between GO and proposed PO method using analytical formulations, and (b) scattered field from a solid wall using proposed PO method with FDTD and with analytical formulations.

the scattered field is compensated for that pulse shape. The frequency domain data are used in (6.2).

The numerical process proposed in this chapter is validated using a dipole moment as a source located at  $x = 3$  m in front of a solid block wall with a relative dielectric constant of  $\epsilon_r = 3.5$ , and thickness of 0.198 m. The observation point is located at  $x = -1$  m. First for an electrically large size wall (13.944 m  $\times$  13.95 m), the PO equivalent currents inside each block is computed, using analytical formulations. Then, the total field at the observation point is compared with Geometrical Optics (GO) solution for different frequency points. Figure 6.2(a) compares the PO results with GO results, where an excellent agreement is shown. In these simulations the size of each block is (0.198 m  $\times$  0.168 m  $\times$  0.09 m). Next the proposed technique based on FDTD numerical analysis is validated for a solid block wall with 12  $\times$  20 blocks (2.016 m  $\times$  1.8 m). Comparison of the scattered fields from the wall calculated by PO approximation using analytical formulations and FDTD numerical technique are shown in Fig.6.2(b).

The proposed numerical technique for computation of transmitted field through the wall is applied on a prominent application which is imaging of a target behind the cinder block wall.

To do this task, SAR algorithm is used. According to Fig. 6.1(a), we assume a transceiver antenna that is moving along an observation line and a point target, located on the dipole moment position. Basically in this process, the received signals along the observation line (scan line) for a prescribed range of frequencies are required. If the transmission matrix of the wall is denoted by  $\overline{\overline{T}}$ , the received signal due to the target is

$$\overline{E}_r = \frac{e^{i2k_0R}}{R^2} (\overline{\overline{T}} \overline{\overline{S}} \overline{\overline{T}}) \cdot \overline{E}_i^0 \quad (6.3)$$

where  $R$  is the distance between the transceiver antenna and the point target,  $\overline{\overline{S}}$  is the volumetric scattering matrix of the point target, and  $\overline{E}_i^0$  is the incident field estimated at the transmitting point. It is noted that in (6.3), the backscatter from the wall itself is assumed to be known and subtracted. The SAR algorithm to construct the target image can be found for example in [55].

### 6.3 Simulation Results

Simulation results for imaging of a point target located behind a cinder block wall is presented in this section. As an example we chose a transceiver antenna (for instance a dipole antenna) which transmits and receives along vertical polarization and the point target that has a unitary scattering matrix. The approximate geometrical parameters of an actual cinder block, with a relative dielectric constant of  $\epsilon_r = 3.5$  are used in the numerical calculations. In order to decrease the size of computational domain in the FDTD numerical analysis, approximately half size of each block along the  $y$  and  $z$  directions are set to be the period (see Fig.6.3(a)). As shown, the size of each block is 0.198 m×0.168 m×0.09 m. Here 12×20 blocks (2.016 m × 1.8 m), corresponding to the structure of 6×10 actual cinder blocks are considered in the simulation. This way a very fine discretization in space and time is achieved, accurate results are obtained, and the distance of the transmitter from the wall is decreased by a factor of about 1/2.44. For frequency range of 0.5 GHz-4.0 GHz, step frequency of 50 MHz, scan line of 1 m, and the spacing between the antenna positions of 2 cm, the target behind the wall is imaged and the results are shown in Fig. 6.3(b). In this

simulation, the target is at  $x = -3$  m, and the scan line is at  $x = 1$  m. As shown, dispersion of the target image as well as presence of multiple strong peaks along the  $x$  direction is due to the scattering effect of periodic cinder block wall.

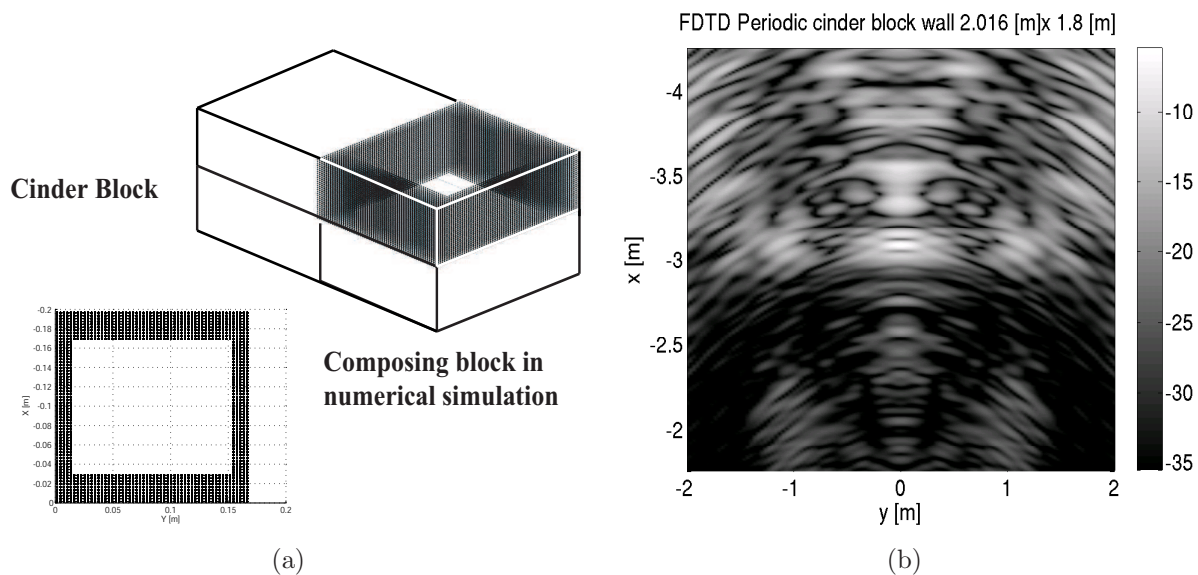


Figure 6.3: (a) Each composing block is considered as a quarter of an actual cinder block. (b) Image of a point target located at  $x = -3$  m behind a cinder block wall.

## 6.4 Experimental Results

To demonstrate the effect of the transmission through the cinder block walls on a point target image an experimental study is also carried out. The measurement setup is similar to the one explained in chapter 5 Section 5.3, except the wall is composed of  $6 \times 10$  cinder blocks (see Fig.6.4). The size of each block is  $19.5 \text{ cm} \times 39.5 \text{ cm} \times 19 \text{ cm}$  and the overall size of the wall is  $2.37 \text{ m} \times 1.90 \text{ m}$ . A metallic sphere with a diameter of  $30.48 \text{ cm}$  is used as a target and placed at about  $2.7 \text{ m}$  behind the wall. The antennas are located at  $0.9 \text{ m}$  in front of the wall. They move along a  $1 \text{ m}$  scan-line with step of  $2.04 \text{ cm}$ . The target image is computed using the backscattered data collected for the frequency range of  $1\text{-}4 \text{ GHz}$  and the step frequency of  $12.5 \text{ MHz}$ . The result is illustrated in Fig.6.5(a). As shown, multiple focused points along the range are generated in the image. This is in agreement with what have been predicted by simulations, shown in Fig.6.3(b).

To refocus the image, another measurement is carried out to estimate the transmissivity of the wall. The process is similar to that explained in chapter 5 subsection III-B. The transmitting antenna is placed at the target position and the receiving antenna is kept in front of the wall at its original position. For different position of the receiving antenna,  $S_{12}$  is measured for two cases, one with the wall and one without the wall. The transmissivity is estimated as the ratio of the two recorded signals. The backscatter data is compensated for the phase of measured transmissivity and the result is shown in Fig.6.5(b). As shown, the image is well focused and the point target image is reconstructed.



Figure 6.4: A cinder block.

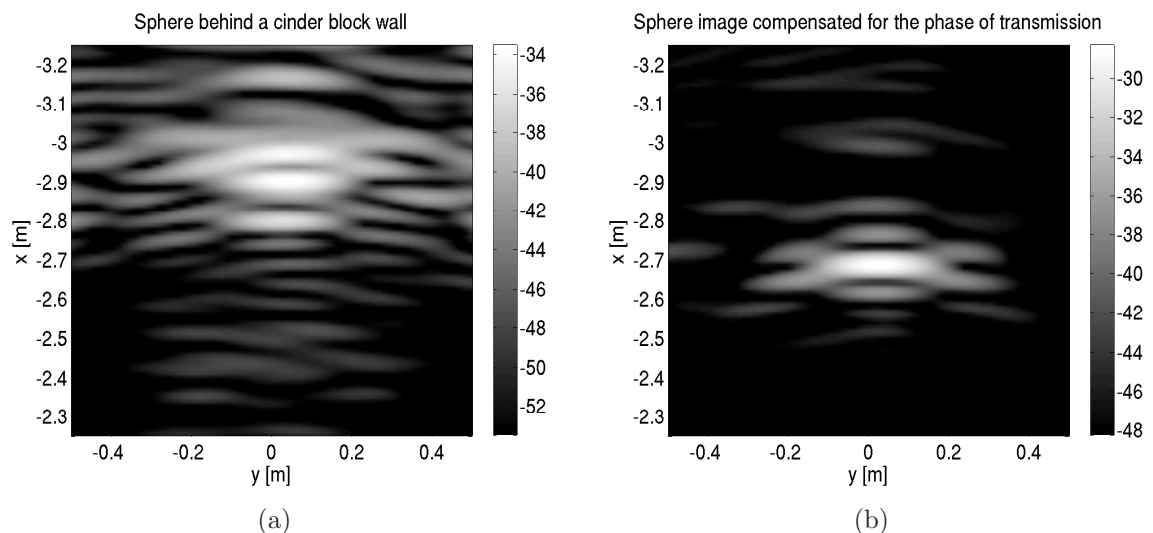


Figure 6.5: (a) Image of the sphere behind the cinder block wall. (b) Image of the sphere compensated for the phase of measured transmissivity.

## CHAPTER 7

# An Approximate Solution of Scattering from Reinforced Concrete Walls Using An Analytic 1-D Periodic Green's Function

Scattering from reinforced concrete walls such as vertical rebar and crossed rebar walls is analyzed, using an accurate approximate analytical approach. The solution is obtained for a plane wave incidence with arbitrary angle of incidence and polarization under the thin wire approximation. The formulation is based on derivation of the Green's function of a one-dimensional periodic structure inside a dielectric slab. Since the metal thickness is assumed small compared to the wavelength, the induced currents are predominantly axial and the transverse components of the induced currents are ignored. This drastically simplifies the solution for this problem which is obtained using a straightforward point-matching technique. The solution for two-dimensional periodic crossed rebar concrete walls is also cast in terms of the one-dimensional periodic Green's function obtained for vertical rebar walls. Using the Finite Difference Time Domain simulation results, it is shown that the induced currents on thin crossed rebars (diameter  $< \lambda_0/5$ ) have primarily a progressive phase equal to that of the incident field in both directions. This observation also points to a simple approximate solution where the problem of scattering from a two-dimensional periodic crossed rebar concrete wall is decomposed into two coupled one-dimensional periodic structures of vertical and horizontal rebar walls. The Bragg mode scattered fields of the reinforced walls are computed for different wall parameters and incidence angles for an operation frequency

range of 0.5-2.0 GHz and validated by Finite Difference Time Domain simulation results. In addition, the validity of the solution is tested using the law of conservation of power for lossless cases.

## 7.1 Introduction

Characterization of propagation and scattering of electromagnetic (EM) waves in urban and indoor environments is of interest for a number of applications such as wireless communication and remote sensing using radar systems. In the area of wireless communication, the radio channel is characterized by an accurate understanding of wave interaction with the building materials, such as building walls. Likewise, in the area of remote sensing using radar systems, detection of targets behind walls is accomplished through an extensive phenomenological studies of scattering from and propagation through building structures using the lower portion of the microwave spectrum. In this case, transmissivity of EM waves through different building walls are needed in order to properly form radar images and develop detection algorithms.

Wave propagation through building structures has been investigated using high frequency Ray-tracing techniques [99]. For homogenous building walls such as poured concrete, brick, and adobe walls, dielectric slab models can predict the transmission and reflection coefficient properties of the walls with reasonable accuracies [35]. On the other hand, for inhomogeneous walls such as reinforced concrete walls (i.e. walls with embedded vertical rebars and crossed rebars) and cinder block walls where the spatial inhomogeneities are comparable to the wavelength, detailed models are needed [100]-[38]. Basically, these walls can be modeled by one-dimensional (1-D) or two-dimensional (2-D) periodic structures. The importance of such models becomes pronounced at relatively high frequencies where the existence of high order Bragg mode scattered fields is evident. In this case, the incident signal power is divided into multitudes of propagating Bragg modes with different wave vectors.

Approximate quasi-static formulas for scattering from reinforced concrete walls are given in [102] which are valid for small concrete-mesh dimensions compared to the wavelength. These models do not account for Bragg modes and thus for practical applications, where

wall periodicity is comparable to or larger than the wavelength the quasi-static solutions are inadequate. On the other hand, accurate scattering from reinforced concrete walls has been examined either by numerical simulations [100], [101], [103] or experiments [36]. The transmission and reflection coefficients of reinforced concrete walls have been computed using the exact numerical methods such as Finite Difference Time Domain (FDTD) technique [100], Finite Element (FEM) method [101], and method of moment (MoM) [103]. In real scenarios building dimensions are much larger than the wavelength and the application of full-wave simulation becomes intractable. Therefore, for simulations of indoor wave propagation, hybrid methods may be used [42]. For such techniques, propagation and scattering of waves with arbitrary polarization and incidence angles from wall segments are required. Hence, the transmission and reflection coefficients and their sensitivity against different wall parameters such as relative dielectric constant and conductivity of the concrete, wall thickness, metal thickness, periodicity of metallic rods, and different polarization and the frequency of the incident field must be computed. This will require considerable amount of computation and storage if full-wave solvers are used. In addition, limitations in implementing numerical techniques may be prohibitive to realize all the simulation configurations. For example, an FDTD method which uses split-field technique requires a long computational time for simulation of periodic structures with low-loss dielectric materials at oblique incidence angles and produces erroneous results for near grazing incident angles [104].

This chapter provides approximate analytical formulations for analyzing wave scattering from reinforced concrete walls which enable simulation of reflection, transmission, and Bragg mode scattering from rebar and crossed rebar structures with arbitrary wall parameters and incident wave attributes so long as the diameter of the metallic bar is small compared to the wavelength. To solve the scattering problem, 1-D periodic Green's function at oblique incidence with sources inside a dielectric slab is derived first. Next, the electric field inside the dielectric slab due to a plane wave illumination (in the absence of metallic rods) is computed and used as the excitation source. Assuming that the embedded metals in the concrete layer are thin relative to the wavelength, only the axial components of the induced currents are considered in this analysis. Then, the induced currents on the metallic rods are calculated by applying the boundary conditions. Finally, all Bragg modes are computed using the Green's

function and the induced currents. It is shown that the induced currents on the crossed rebars have primarily a progressive phase equal to that of the incident field. Therefore, to simulate the scattered fields from crossed rebar concrete walls, the 2-D periodic structure is broken into two coupled 1-D periodic structures. To validate the formulations, transmission and reflection coefficients of different walls for different incidence angles are computed and compared with the results obtained from FDTD numerical simulations.

The chapter is organized as follows. In Section 7.2, the formulation for 1-D periodic Green's function with sources inside a dielectric layer is derived and used to compute induced currents on metallic rods embedded in a dielectric slab. In Section 7.3, the formulation for the vertical rebar is extended to include the scattering from crossed rebar concrete walls. Validation through a comprehensive numerical comparison with FDTD results is provided in Section 7.4.

## 7.2 Formulation

Geometry of the scattering problem for a reinforced concrete wall is shown in Fig. 7.1. Assuming the wall height is much longer than the wavelength, the scatterer can be viewed as a 1-D periodic structure. Metallic rods with thickness of  $2a$  are placed at  $z = s'$  with period  $L_x$  along x-axis inside a concrete wall with thickness of  $d$  and relative complex dielectric constant of  $\epsilon_r$ . First, let us consider a simple case where the metallic rods are against a uniform dielectric background (e.g. free-space) [105]. Assuming axial currents only, all field quantities can be obtained from coaxial component  $E_y$  which satisfies the scalar wave equation given by

$$\nabla^2 E_y + k^2 E_y = -ikZ J_y. \quad (7.1)$$

Here  $J_y$  is the induced current density, along  $\hat{y}$  direction. Suppose a plane wave given by

$$\bar{E}_i = \hat{e} e^{i\bar{k}_i \cdot \bar{r}} \quad (7.2)$$

is illuminating the structure whose propagation wave vector and polarization are respectively given by  $\bar{k}_i = k_{xi}\hat{x} + k_{yi}\hat{y} + k_{zi}\hat{z}$  and  $\hat{e}$ . Since there is no variation along  $\hat{y}$  direction, all field

components have the same  $y$ -dependence as that of the incident field, i.e.  $E_y(x, y, z) = E_y e^{ik_{yi}y}$ . It can be shown that field components on the transverse plane (i.e.  $xz$ -plane) can be computed from [88]

$$\begin{aligned}\bar{E}_t &= \frac{i}{k^2 - k_{yi}^2} (k_{yi} \nabla_t E_y + kZ \nabla_t H_y \times \hat{y}) \\ \bar{H}_t &= \frac{i}{k^2 - k_{yi}^2} (k_{yi} \nabla_t H_y - kY \nabla_t E_y \times \hat{y})\end{aligned}\quad (7.3)$$

where  $\bar{E}_t = E_x \hat{x} + E_z \hat{z}$ ,  $\bar{H}_t = H_x \hat{x} + H_z \hat{z}$ , and  $\nabla_t = \frac{\partial}{\partial x} \hat{x} + \frac{\partial}{\partial z} \hat{z}$ .

Now consider an array of filament currents with periodicity of  $L_x$  flowing along  $\hat{y}$  direction. This constitutes the Green's function of the structure. Let us suppose the position of the filament current in the first period is specified by  $\bar{\rho}' = (x', z')$ . Denoting the scalar Green's function by  $g_p(\bar{\rho}, \bar{\rho}')$ , we have

$$(\nabla_t^2 + k_\rho^2) g_p(\bar{\rho}, \bar{\rho}') = - \sum_{n=-\infty}^{+\infty} e^{ik_{xi}(nL_x)} \delta(\bar{\rho} - \bar{\rho}'_n) \quad (7.4)$$

where  $k_\rho^2 = k_0^2 - k_{yi}^2$  and  $\bar{\rho}'_n = (x' + nL_x, z')$ . It can be shown that [88]

$$g_p(x, z; x', z') = \frac{i}{2L_x} \sum_{n=-\infty}^{+\infty} \frac{1}{k_{nz}} e^{ik_{nx}(x-x')} e^{ik_{nz}|z-z'|} \quad (7.5)$$

where  $k_{nx} = k_{xi} + \frac{2\pi n}{L_x}$  and  $k_{nz} = \sqrt{k_\rho^2 - k_{nx}^2}$ . The Green's function in (7.5), is a summation of plane waves whose wave vectors are  $k_{nx} \hat{x} + k_{yi} \hat{y} \pm k_{nz} \hat{z}$ . Of these waves, the modes with non-negative  $k_\rho^2 - k_{nx}^2$  are propagating modes. It is noted that the currents have only  $\hat{y}$  component, and therefore for this case where the array of filament currents is in a homogeneous medium,  $H_y=0$ . Explicitly, the solution of (7.1) due to a periodic array of filament currents with excitation of  $I_y$ , is given by

$$E_y = \frac{-kZI_y}{2L_x} \sum_{n=-\infty}^{+\infty} \frac{1}{k_{nz}} e^{ik_{nx}(x-x')} e^{ik_{nz}|z-z'|}. \quad (7.6)$$

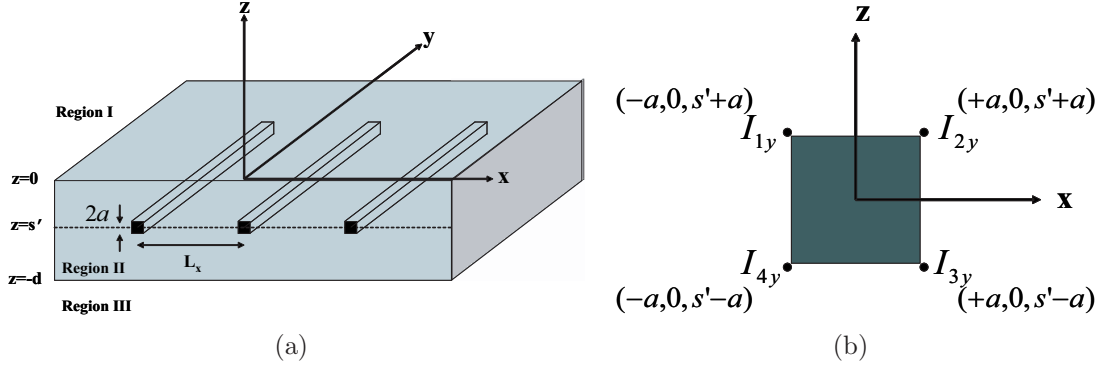


Figure 7.1: (a) Geometry of a vertical rebar concrete wall. (b) Cross section of a metallic rod.

### 7.2.1 Computation of induced currents on metallic rods

To solve for the induced currents on the metallic rods, thin wire approximation can be used. For metallic rods with thickness much smaller than the wavelength  $\lambda$  (i.e.  $a \ll \lambda$ ), the induced surface current is approximated by a  $\hat{y}$ -directed filament current, placed at the center of the rod ( $z = s'$ ). By applying the boundary condition on the metal surface,  $z = s' + a$ , we have

$$I_y = \frac{2L_x}{k_0 Z_0} \frac{e^{ik_{zi}(s'+a)}}{\sum_{n=-\infty}^{+\infty} \frac{e^{ik_{nz}a}}{k_{nz}}} \hat{e} \cdot \hat{y} \quad (7.7)$$

This closed-form solution provides satisfactory results for a practical rod thickness of less than 2.4 cm up to 2 GHz in free-space background. However, in a concrete with relative dielectric constant of  $\epsilon_r = 6$  the apparent dimensions of the metallic rods become larger (2.4 cm rod thickness is about  $0.4 \lambda_d$ , where  $\lambda_d$  is the wavelength inside the dielectric at 2 GHz). In this case, induced currents computed under thin wire approximation given by (7.7) does not provide the required accuracy. Much better results are obtained by modeling the induced currents on each rod by four filament currents, placed at four corners of the rod. Figure 7.1(b) shows a cross section of the metallic rod where four filament currents with four unknown coefficients  $I_{1y}$ ,  $I_{2y}$ ,  $I_{3y}$ , and  $I_{4y}$  are placed at corners of the rod. The unknown coefficients are computed using the MoM and a direct analytical inversion. The assumption that four filament currents are sufficient to represent the induced currents is justified by simulation results, provided in Section 7.4. By evaluating the scattered fields from (7.6) over

the surface of the metal and applying the boundary conditions, the excitation currents are calculated.

### 7.2.2 1-D periodic Green's function for the case where sources are inside a dielectric slab

For the problem where the metallic rods are inside a dielectric slab, the total field inside region II, is composed of the fields from the source directly, downward-going waves from the source reflected at interface between region I and II, and upward-going waves from the source reflected at the interface between region II and III (see Fig.7.1). In order to find the Green's function of the problem, we use the same form of the scattered fields derived previously in (7.6) except we introduce new coefficients to describe the upward-going and downward-going waves inside region II. Unlike the free-space case the air-dielectric interface produces non-vanishing  $H_y$  and therefore both axial field components  $E_y$  and  $H_y$  are needed to fully represent all field components in the transverse plane. Therefore, for the array of filament currents inside the dielectric slab, the axial components are given by

$$\begin{aligned}
 E_y^{II} &= \sum_{n=-\infty}^{+\infty} \frac{1}{k_{1nz}} e^{ik_{nx}(x-x')} (\tilde{I}_y e^{ik_{1nz}|z-z'|} + \\
 &\hspace{15em} A_n e^{ik_{1nz}z} + B_n e^{-ik_{1nz}z}) \\
 H_y^{II} &= \sum_{n=-\infty}^{+\infty} \frac{1}{k_{1nz}} e^{ik_{nx}(x-x')} (A'_n e^{ik_{1nz}z} + B'_n e^{-ik_{1nz}z}) \tag{7.8}
 \end{aligned}$$

where  $\tilde{I}_y = -\frac{k_1 Z_1}{2L_x} I_y = -\frac{k_0 Z_0}{2L_x} I_y$ , and  $k_{1nz} = \sqrt{k_1^2 - k_{nx}^2 - k_{yi}^2}$ . The unknown coefficients  $A_n$ ,  $B_n$ ,  $A'_n$ , and  $B'_n$  are representing the standing waves coefficients and must be determined by applying the boundary conditions at both sides of the air-dielectric interfaces. Similarly,  $E_y$

and  $H_y$  in regions I and III are expressed by

$$\begin{aligned}
E_y^I &= \tilde{I}_y \sum_{n=-\infty}^{+\infty} \frac{C_n}{k_{nz}} e^{ik_{nx}(x-x')} e^{ik_{nz}(z-z')} \\
H_y^I &= \sum_{n=-\infty}^{+\infty} \frac{D_n}{k_{nz}} e^{ik_{nx}(x-x')} e^{ik_{nz}z} \\
E_y^{III} &= \tilde{I}_y \sum_{n=-\infty}^{+\infty} \frac{E_n}{k_{nz}} e^{ik_{nx}(x-x')} e^{-ik_{nz}(z-z')} \\
H_y^{III} &= \sum_{n=-\infty}^{+\infty} \frac{F_n}{k_{nz}} e^{ik_{nx}(x-x')} e^{-ik_{nz}z}.
\end{aligned} \tag{7.9}$$

By applying the boundary conditions to the tangential electric and magnetic field components,  $E_x$ ,  $E_y$ ,  $H_x$ , and  $H_y$  at  $z = 0$  and  $z = -d$ , eight equations are obtained which are sufficient to solve for the eight unknowns,  $A_n$ ,  $B_n$ ,  $A'_n$ ,  $B'_n$ ,  $C_n$ ,  $D_n$ ,  $E_n$ , and  $F_n$ . Two other tangential components,  $E_x$  and  $H_x$ , are derived using (7.3) and reported in the appendix. After much algebraic manipulation four equations governing  $A_n$ ,  $B_n$ ,  $A'_n$ , and  $B'_n$  are obtained which are given in a matrix form in the bottom of this page.

In (7.10),  $\gamma_1$ ,  $\gamma_2$ ,  $\gamma_3$ ,  $\gamma_4$ , and  $\gamma_5$  are given by

$$\begin{aligned}
\gamma_1 &= \frac{k_{nx}k_{yi}}{k_{1nz}} \left( \frac{k_{\rho 1}^2}{k_{\rho 0}^2} - 1 \right), \\
\gamma_2 &= k_0 Z_0 \left( \frac{k_{nz}}{k_{1nz}} \frac{k_{\rho 1}^2}{k_{\rho 0}^2} - 1 \right), \quad \gamma_3 = k_0 Z_0 \left( \frac{k_{nz}}{k_{1nz}} \frac{k_{\rho 1}^2}{k_{\rho 0}^2} + 1 \right), \\
\gamma_4 &= \frac{k_{nz}}{k_{1nz}} \frac{k_{\rho 1}^2}{k_{\rho 0}^2} - \epsilon_r, \quad \gamma_5 = \frac{k_{nz}}{k_{1nz}} \frac{k_{\rho 1}^2}{k_{\rho 0}^2} + \epsilon_r,
\end{aligned} \tag{7.11}$$

where,  $k_{\rho 1}^2 = k_1^2 - k_{yi}^2$  and  $k_{\rho 0}^2 = k_0^2 - k_{yi}^2$ . From equation (7.10),  $A_n$ ,  $B_n$ ,  $A'_n$ , and  $B'_n$  are derived analytically. To save the space, their expressions are not reported here. Equations

---


$$\begin{pmatrix} \gamma_1 & \gamma_1 & -\gamma_2 & -\gamma_3 \\ \gamma_4 & \gamma_5 & \frac{Z_0}{k_0} \gamma_1 & \frac{Z_0}{k_0} \gamma_1 \\ \gamma_1 e^{-ik_{1nz}d} & \gamma_1 e^{+ik_{1nz}d} & \gamma_3 e^{-ik_{1nz}d} & \gamma_2 e^{+ik_{1nz}d} \\ \gamma_5 e^{-ik_{1nz}d} & \gamma_4 e^{+ik_{1nz}d} & -\frac{Z_0}{k_0} \gamma_1 e^{-ik_{1nz}d} & -\frac{Z_0}{k_0} \gamma_1 e^{+ik_{1nz}d} \end{pmatrix} \begin{pmatrix} A_n \\ B_n \\ A'_n \\ B'_n \end{pmatrix} = -\tilde{I}_y \begin{pmatrix} \gamma_1 e^{-ik_{1nz}z'} \\ \gamma_4 e^{-ik_{1nz}z'} \\ \gamma_1 e^{ik_{1nz}(d+z')} \\ \gamma_4 e^{ik_{1nz}(d+z')} \end{pmatrix} \tag{7.10}$$

for  $C_n$ ,  $D_n$ ,  $E_n$ , and  $F_n$  in terms of  $A_n$ ,  $B_n$ ,  $A'_n$ , and  $B'_n$  are given by

$$\begin{aligned}
C_n &= e^{ik_{nz}z'} \frac{k_{nz}}{k_{1nz}} \left[ \frac{1}{\tilde{I}_y} (A_n + B_n) + e^{-ik_{1nz}z'} \right] \\
D_n &= \frac{k_{nz}}{k_{1nz}} (A'_n + B'_n) \\
E_n &= e^{-ik_{nz}(d+z')} \frac{k_{nz}}{k_{1nz}} \\
&\quad \left[ \frac{1}{\tilde{I}_y} (A_n e^{-ik_{1nz}d} + B_n e^{+ik_{1nz}d}) + e^{ik_{1nz}(d+z')} \right] \\
F_n &= e^{-ik_{nz}d} \frac{k_{nz}}{k_{1nz}} (A'_n e^{-ik_{1nz}d} + B'_n e^{+ik_{1nz}d}). \tag{7.12}
\end{aligned}$$

### 7.2.3 Computation of incident fields inside the dielectric slab

In order to compute the induced currents on the metallic rods, the fields inside the dielectric slab (in the absence of metallic rods) due to an incident plane wave are needed. Reflection and transmission by a layered media is explained in [88]. Here, formulations for reflected and transmitted fields and the expression of fields inside the dielectric slab are given. The polarization unit vector  $\hat{e}$  given in (7.2) can be decomposed into vertical and horizontal unit vectors, defined in the global coordinate system by

$$\begin{aligned}
\hat{h}_i &= \frac{\hat{k}_i \times \hat{z}}{|\hat{k}_i \times \hat{z}|} \\
\hat{v}_i &= \hat{h}_i \times \hat{k}_i. \tag{7.13}
\end{aligned}$$

If we define  $\alpha = \hat{e} \cdot \hat{v}_i$  and  $\beta = \hat{e} \cdot \hat{h}_i$ , it can be shown that the fields inside region I and III are respectively

$$\begin{aligned}
\bar{E}_i^I &= \alpha (\hat{v}_i e^{i\bar{k}_i \cdot \bar{r}} + R_{TM} \hat{v}_r e^{i\bar{k}_r \cdot \bar{r}}) + \\
&\quad \beta (\hat{h}_i e^{i\bar{k}_i \cdot \bar{r}} + R_{TE} \hat{h}_r e^{i\bar{k}_r \cdot \bar{r}}) \\
\bar{E}_i^{III} &= \alpha T_{TM} \hat{v}_i e^{i\bar{k}_i \cdot \bar{r}} + \beta T_{TE} \hat{h}_i e^{i\bar{k}_i \cdot \bar{r}} \tag{7.14}
\end{aligned}$$

where  $\bar{k}_r = k_{xi}\hat{x} + k_{yi}\hat{y} - k_{zi}\hat{z}$ . Here,  $\hat{v}_r$  and  $\hat{h}_r$  are computed using (7.13), where  $\hat{k}_i$  is replaced by  $\hat{k}_r = \hat{k}_i - 2\hat{k}_i \cdot \hat{z}$ .  $R_{TE}$  and  $R_{TM}$  are the reflection coefficients of dielectric slab

for horizontal and vertical polarization of incident field, respectively. Similarly  $T_{TE}$  and  $T_{TM}$  are the transmission coefficients of the dielectric slab for horizontal and vertical polarization of incident field, respectively. The expressions for the transmission and reflection coefficients are given in [88]. It can be shown that the fields inside region II is

$$\begin{aligned}\bar{E}_i^{II} = & (A\bar{v}_t^+ + B\hat{h}_t^+)e^{i\bar{k}_t^+ \cdot \bar{r}} + \\ & (C\bar{v}_t^- + D\hat{h}_t^-)e^{i\bar{k}_t^- \cdot \bar{r}}\end{aligned}\quad (7.15)$$

where  $\bar{k}_t^\pm = k_{xi}\hat{x} + k_{yi}\hat{y} \pm k_z\hat{z}$  and  $k_z = \sqrt{k_1^2 - k_{xi}^2 - k_{yi}^2}$ . Here  $\hat{h}_t^\pm$  and  $\bar{v}_t^\pm$  are

$$\begin{aligned}\hat{h}_t^\pm &= \frac{\bar{k}_t^\pm \times \hat{z}}{|\bar{k}_t^\pm \times \hat{z}|} \\ \bar{v}_t^\pm &= \frac{k_0 Z_0}{Z_1} \frac{1}{\bar{k}_t^\pm \cdot \bar{k}_t^\pm} (\hat{h}_t^\pm \times \bar{k}_t^\pm)\end{aligned}\quad (7.16)$$

and coefficients  $A$ ,  $B$ ,  $C$ , and  $D$  are found to be

$$\begin{aligned}A &= \frac{\alpha Z_1}{Z_0} \frac{1 + R_{TM} - T_{TM}e^{-i(k_{zi}+k_z)d}}{1 - e^{-2ik_z d}} \\ B &= \beta \frac{1 + R_{TE} - T_{TE}e^{-i(k_{zi}+k_z)d}}{1 - e^{-2ik_z d}} \\ C &= \frac{\alpha Z_1}{Z_0} \frac{1 + R_{TM} - T_{TM}e^{-i(k_{zi}-k_z)d}}{1 - e^{+2ik_z d}} \\ D &= \beta \frac{1 + R_{TE} - T_{TE}e^{-i(k_{zi}-k_z)d}}{1 - e^{+2ik_z d}}.\end{aligned}\quad (7.17)$$

Once the electric fields inside the dielectric slab is calculated using (7.15), the induced currents  $\tilde{I}_{1y}$ ,  $\tilde{I}_{2y}$ ,  $\tilde{I}_{3y}$ , and  $\tilde{I}_{4y}$  at four corners of the metallic rod are computed by evaluating the scattered fields using (7.8) and applying the boundary conditions.

## 7.2.4 Computation of transmission and reflection coefficients

It is noted that the expressions of scattered fields given in (7.9) are summations of plane waves. The reflected field in region I is a summation of plane waves, propagating along  $\bar{k}_{nr} = k_{nx}\hat{x} + k_{yi}\hat{y} + k_{nz}\hat{z}$  and similarly transmitted field in region III is a summation of plane

waves, propagating along  $\bar{k}_{nt} = k_{nx}\hat{x} + k_{yi}\hat{y} - k_{nz}\hat{z}$ , where  $n$  is the mode number of each propagating wave. Polarization of each plane wave reflected field (or transmitted field) can be determined by defining vertical and horizontal unit vectors  $\hat{v}_{nr}$  (or  $\hat{v}_{nt}$ ) and  $\hat{h}_{nr}$  (or  $\hat{h}_{nt}$ ). These unit vectors are defined using (7.13), where  $\hat{k}_i$  is replaced by  $\hat{k}_{nr}$  (or  $\hat{k}_{nt}$ ). Reflection coefficient  $R_n$  and transmission coefficient  $T_n$  of the  $n$ th propagating mode is given by

$$\begin{aligned} R_{npq} &= \bar{E}_{nq}^I \cdot \hat{p}_{nr} \\ T_{npq} &= \bar{E}_{nq}^{III} \cdot \hat{p}_{nt} \end{aligned} \quad (7.18)$$

where  $q$  can be  $v$  or  $h$  respectively for vertical or horizontal polarization of the incident field, and  $p$  can be  $v$  or  $h$  respectively for vertical or horizontal polarization of the reflected or transmitted field. In (7.18),  $\bar{E}_{nq}^I$  and  $\bar{E}_{nq}^{III}$  are the  $n$ th order propagating Bragg modes respectively in region I and III, computed at the origin when the polarization of incident field is  $\hat{q}$ , which can be  $\hat{v}_i$  or  $\hat{h}_i$ . It is noted that for  $n=0$  (i.e. the zeroth order mode) the total field in region I and III is the superposition of scattered fields from the induced currents derived from (7.9) and the reflected and transmitted fields due to the incident field itself, calculated from (7.14).

The normalized power ratio associated with the  $n$ th order Bragg mode is defined by

$$P_n = \left| \frac{k_{nz}}{k_{zi}} \right| \frac{|\bar{E}_{nq}^I|^2 + |\bar{E}_{nq}^{III}|^2}{|\bar{E}_i|^2} \quad (7.19)$$

where  $|\bar{E}|^2 = |\bar{E} \cdot \hat{x}|^2 + |\bar{E} \cdot \hat{y}|^2 + |\bar{E} \cdot \hat{z}|^2$ . The quantity  $|k_{nz}/k_{zi}|$  accounts for the ratio of intersected areas, perpendicular to collimated beams along the directions of propagation. Based on the law of conservation of power, the summation of  $\sum_n P_n$  over all the propagating modes must be unity for lossless materials.

### 7.3 Scattering from crossed rebar walls

The geometry of a crossed rebar concrete wall is shown in Figure 7.2. The crossed rebar wall can be viewed as a 2-D periodic structure. To solve the problem in an accurate fashion, a solution based on a 2-D periodic Green's function must be considered [106]. That is,

the induced currents on the metallic rods must be discretized into a 2-D periodic array of Hertzian elements in the  $xy$ -plane. The Green's function for this problem is rather complex and does not render a simple closed-form solution for the induced currents. Solution to this problem has been considered using a numerical solution based on MoM [103]. Here we consider the geometrical features of the structure that have not been exploited before and can be utilized to arrive at a simple solution.

Using the thin wire approximation as before, it is realized that the induced currents on the metallic bars are predominantly axial. It is also observed that the metallic bars are on a perpendicular grid which minimizes intermodal coupling. For a 2-D periodic structure, the Bragg modes would propagate along  $k_{nm} = k_{nx}\hat{x} + k_{my}\hat{y} \pm k_{nmz}\hat{z}$ , where  $k_{nx} = k_{xi} + \frac{2\pi n}{L_x}$ ,  $k_{my} = k_{yi} + \frac{2\pi m}{L_y}$ , and  $k_{nmz} = \sqrt{k_0^2 - k_{nx}^2 - k_{my}^2}$ . Each Bragg mode is specified by a pair index  $(n, m)$  associated with the propagating wave constants  $k_{nx}$  and  $k_{my}$ . Our conjecture is that the energy stored or carried by the  $(n, m)$  mode with  $n \neq 0$  and  $m \neq 0$  is negligible. If this is true, the solution for the 2-D problem can be cast in terms of two coupled 1-D problems.

Let us consider a practical crossed rebar concrete wall shown in Fig. 7.2 with the following parameters. The wall thickness is 10.2 cm, metal thickness is 1.2 cm,  $L_x = L_y = 38.1$  cm, the relative dielectric constant and conductivity of the concrete are respectively  $\epsilon_r = 6$  and  $\sigma = 0.01$ . Position of the metallic rod is at the middle of the dielectric (i.e.  $s' = -5.1$  cm). For an incident wave vector along  $\theta = 150^\circ$  and  $\phi = 30^\circ$ , the propagating Bragg modes have indices of  $(0, 0)$ ,  $(\pm 1, 0)$ ,  $(0, \pm 1)$ ,  $(-2, 0)$ ,  $(0, -2)$ ,  $(-3, 0)$ , and cross-mode combinations that neither  $n$  nor  $m$  is zero, including  $(-1, 1)$ ,  $(\pm 1, -1)$ ,  $(\pm 1, -2)$ ,  $(-2, \pm 1)$ ,  $(-3, \pm 1)$ ,  $(-2, -2)$ ,  $(-3, -2)$ ,  $(-1, -3)$ , and  $(-2, -3)$ . Here,  $\theta$  is the angle between  $\bar{k}_i$  and  $\hat{z}$  and  $\phi$  is the angle between projection of  $\bar{k}_i$  in the  $xy$ -plane and  $\hat{x}$ . An FDTD code is used to generate all these Bragg modes. Comparisons have been made between the  $(0, 0)$  order mode, and the rest of the modes. It is observed that, scattered modes with indices  $(n, 0)$  and  $(0, m)$  are on average about one order of magnitude smaller than the zeroth order mode and the rest of the modes with indices  $(n, m)$  with  $n \neq 0$  and  $m \neq 0$  are about two orders of magnitude smaller than zeroth order mode.

The normalized power ratio  $P_{nm}$  is computed using the formula given by (7.19), except  $k_{nz}$  is now replaced by  $k_{nmz}$ . To demonstrate the significance of different Bragg modes, the

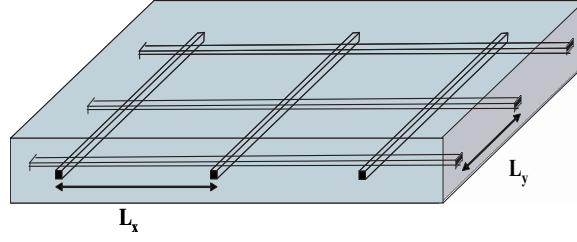


Figure 7.2: Geometry of a crossed-rebar concrete wall.

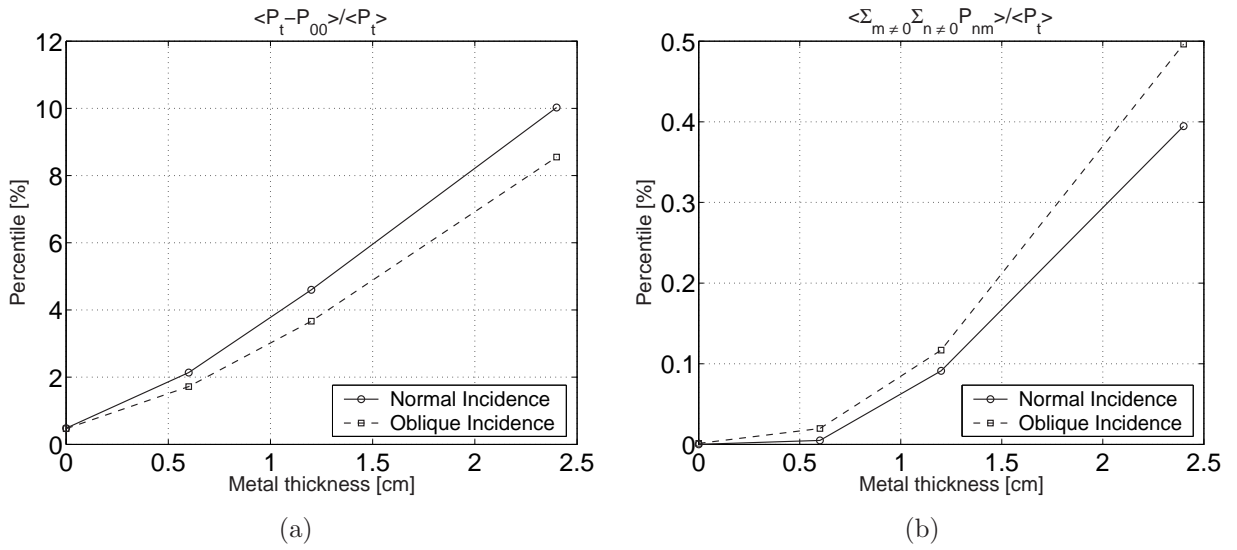


Figure 7.3: Relative average powers of Bragg modes, scattered from the crossed rebar concrete wall, due to a TE polarized incident field at oblique ( $\theta=150^\circ$ ,  $\phi=30^\circ$ ) and normal incident angles, computed with an FDTD numerical method for different metal thicknesses. (a) Relative average power carried by all Bragg modes except zeroth order mode (i.e.  $\langle P_t - P_{00} \rangle / \langle P_t \rangle$ ) and (b) relative average power carried by modes for which  $n \neq 0$  and  $m \neq 0$  (i.e.  $\langle \sum_{n \neq 0} \sum_{m \neq 0} P_{nm} \rangle / \langle P_t \rangle$ ).

average of normalized power ratio  $\langle P_{nm} \rangle$  over the frequency range of interest (0.5-2 GHz) is computed and compared to the average of total normalized power ratio  $\langle P_t \rangle = \sum_n \sum_m \langle P_{nm} \rangle$ . Figure 7.3(a) shows  $\langle P_t - P_{00} \rangle / \langle P_t \rangle$  as a function of metal thickness at normal and oblique incidence angles to confirm the significance of the zeroth order mode. Fig. 7.3(b) shows the ratio of average power carried by all coupled modes for which  $n \neq 0$  and  $m \neq 0$  to the averaged total power ( $\langle \sum_{n \neq 0} \sum_{m \neq 0} P_{nm} \rangle / \langle P_t \rangle$ ) for different metal thicknesses, at normal and oblique incidence angles. Here, the oblique incident wave vector is along  $\theta = 150^\circ$  and  $\phi = 30^\circ$ . As shown in Fig. 7.3(a), by increasing the metal thickness the

effect of higher order Bragg modes becomes more significant. However, for metal thickness smaller than 2.4 cm, more than 90% of the total power is carried by the zeroth order Bragg mode. Furthermore, as shown in Fig. 7.3(b) less than 0.5% of the total power is carried by the modes corresponding to  $(n, m)$  for which  $n \neq 0$  and  $m \neq 0$ . Hence, ignoring coupled modes in the formulation does not affect the accuracy significantly for metals thinner than 2.4 cm and frequencies below 2 GHz.

For  $n = 0$  or  $m = 0$  modes, the induced currents on the metallic rods along  $\hat{x}$  and  $\hat{y}$  have the progressive phases proportional to  $k_{xi}$  and  $k_{yi}$ , respectively. This simplifies the analysis of the crossed rebar walls significantly. Basically, the problem can be decomposed into two 1-D periodic structures. One structure is an array of  $\hat{x}$ -directed currents with periodicity of  $L_y$  and the other structure is an array of  $\hat{y}$ -directed currents with periodicity of  $L_x$ . First, the Green's function is derived for each case separately similar to what was described in Subsection 7.2.2. For the  $\hat{x}$ -directed currents the axial field components are  $E_x$  and  $H_x$ . Therefore, we consider  $E_x(x, y, z) = E_x(y, z)e^{ik_{xi}x}$ ,  $H_x(x, y, z) = H_x(y, z)e^{ik_{xi}x}$ , and expand the radiated fields  $E_x$  and  $H_x$  similar to  $E_y$  and  $H_y$ , given in (7.8) and (7.9), except  $\tilde{I}_y$  is replaced by  $\tilde{I}_x$  where  $\tilde{I}_x = -\frac{k_0 Z_0}{2L_y} I_x$  and  $k_{nx}(x - x')$  is replaced by  $k_{my}(y - y')$  where  $k_{1mz} = \sqrt{k_1^2 - k_{xi}^2 - k_{my}^2}$ , and  $k_{mz} = \sqrt{k_0^2 - k_{xi}^2 - k_{my}^2}$ . Similar to the procedure shown in Subsection 7.2.2, the appropriate boundary conditions are applied and the unknown coefficients in the fields' representations for the Green's function are derived.

Second, the scattering problem is solved by computing the induced currents on the metallic rods. It should be noted that the  $\hat{x}$ - and  $\hat{y}$ -directed currents on the orthogonal grid of wires are coupled and very much different from the currents on two isolated  $\hat{x}$ -directed and  $\hat{y}$ -directed metallic rods. By applying the boundary conditions coupled system of equations for the two unknown currents are obtained and solved. The approximate solution for Bragg modes of the crossed rebar wall, propagates either along  $\bar{k}_{n0} = (k_{xi} + \frac{2\pi n}{L_x})\hat{x} + k_{yi}\hat{y} \pm k_{nz}\hat{z}$  or along  $\bar{k}_{0m} = k_{xi}\hat{x} + (k_{yi} + \frac{2\pi m}{L_y})\hat{y} \pm k_{mz}\hat{z}$ .

As for the case of vertical rebar, filament current approximation for the induced currents on metallic bars within the concrete layer does not produce accurate results for thickness values larger than 1 cm. Like before, four filament currents at the corners of each metallic bar can be considered to improve the accuracy for thicker metallic bars. Formulations for

the computation of the reflection and transmission coefficients are similar to those given by (7.18). Here the vertical and horizontal unit vectors are defined for wave vectors  $\bar{k}_{n0}$  and  $\bar{k}_{0m}$  and the reflection and transmission coefficients due to each polarization configuration are computed. The normalized power ratio associated with each Bragg mode is also calculated using the formula given by (7.19).

## 7.4 Numerical Simulations

The approximate analytical formulations of scattering from reinforced concrete walls are validated using a full-wave FDTD numerical technique [67]. In the FDTD simulations of periodic structures, periodic boundary conditions are applied on the boundaries of a block. The periodic boundary planes in these simulations are xz- and yz-plane. Using proper time steps and time delays the scattered fields are transferred from the time domain into the frequency domain using the Fourier transform. For broadband simulations a differentiated Gaussian pulse with a proper bandwidth is used as the incident field. The spectrum of the computed scattered field is compensated for the non-uniform spectrum of the differentiated Gaussian pulse. In the following simulations, the phase center of scattered fields is chosen at the origin of the coordinate system, at the front surface of the wall. The co-polarized transmission and reflection coefficients due to a horizontal (TE) polarized incident field are calculated using the analytical formulations and compared with FDTD numerical results.

First, simulation of scattering from a vertical rebar in free space is considered. In this simulation, the thickness of the metallic rods is 1.2 cm and periodicity is 30.6 cm. The induced currents on the metallic rods are computed analytically using (7.7). Fig.7.4 shows comparisons between the analytical and FDTD numerical results where a very good agreement is shown both in reflection and transmission coefficients. Small discrepancies between the two methods in the higher order modes of transmission coefficient is due to the approximate nature of the solution and limited accuracy of FDTD.

Next, simulations of reflection and transmission coefficients for reinforced concrete walls are considered. In these simulations four filament currents are considered at four corners of each metallic rod. Two cases of vertical rebar walls are considered. Case A is a concrete wall

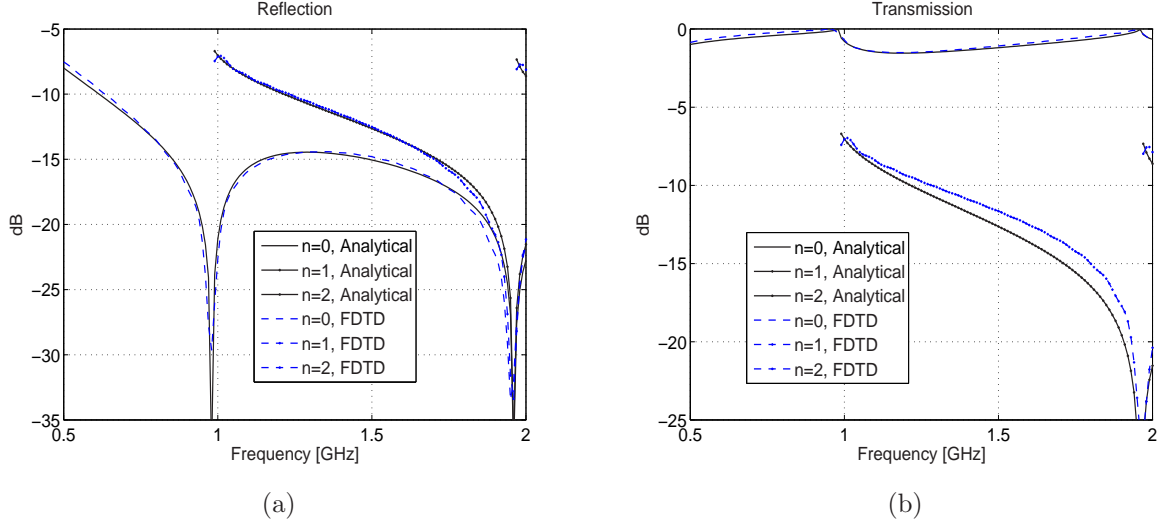


Figure 7.4: (a) Magnitude of co-polarized reflection coefficients, and (b) transmission coefficients of a vertical rebar in free space at normal incidence ( metal thickness = 1.2 cm). Polarization of incident field is horizontal/TE (i.e. parallel to the vertical rebar).

with the wall thickness of  $d = 20.4$  cm, metal thickness of  $2a = 1.2$  cm, and periodicity of  $L_x = 30.6$  cm. The relative dielectric constant of the concrete is  $\epsilon_r = 6$  and its conductivity is  $\sigma = 0.01$ . Position of metallic rods is at the middle of the dielectric (i.e.  $s' = -10.2$  cm). Case B is a reinforced concrete wall with the same parameters as those of case A, except for the metal thickness which is changed to 2.4 cm. For each case amplitude and phase of transmission and reflection coefficients are computed with analytical formulations and compared with FDTD results. Different incidence angles are chosen to validate the accuracy of the formulations.

Figures 7.5 and 7.6 show comparisons between analytical and FDTD simulations of the amplitude and phase of the zeroth order reflection and transmission coefficients of the vertical rebar concrete wall of case A, where excellent agreements are shown. Figure 7.7 shows the comparison between analytical and FDTD simulations of the amplitude of higher order reflected and transmitted Bragg modes. Figures 7.8 and 7.9 show the same comparisons for the zeroth order transmission and reflection coefficients of case B, where very good agreement is shown as well. The same comparisons are made for an oblique incidence angle. The direction of incident wave vector  $\bar{k}_i$  is along  $\theta = 150$  and  $\phi = 30$ . Figures 7.10 and 7.11 show comparisons between the amplitude and phase of the zeroth order co-polarized

transmission and reflection coefficients of vertical rebar wall case B. Very good agreement is shown between analytical and FDTD simulation results.

In addition, transmission and reflection coefficients of the crossed rebar concrete wall are simulated. The thickness of such wall is 10.2 cm. The metal thickness is 1.2 cm, and periodicities along  $\hat{x}$  and  $\hat{y}$  directions are  $L_x = L_y = 38.1$  cm. The relative dielectric constant of the concrete is  $\epsilon_r = 6$  and its conductivity is  $\sigma = 0.01$ . Position of the metallic rod is at the middle of the dielectric (i.e.  $s' = -5.1$  cm). Figures 7.12 and 7.13 show comparisons between the simulated zeroth order co-polarized transmission and reflection coefficients of crossed rebar wall for a horizontal polarization of incident field and for an oblique incidence angle (i.e.  $\theta = 150$  and  $\phi = 30$ ). As shown, very good agreement between the numerical FDTD and approximate analytical simulations is achieved. The small discrepancies between the two simulations are the results of approximate nature of both the analytical formulations and the FDTD technique.

To arrive at accurate results when using FDTD, sufficient time steps are needed in the simulations. For relatively low loss materials and at oblique incident angles the number of iterations must be increased. At certain frequencies where structure resonances occur the time-domain signal does not decay fast enough after a finite number of time steps. This is the reason for inclusion of loss in the material when using FDTD and the need for increasing the number of time steps for FDTD simulation of periodic structures. The law of conservation of power could not be verified for lossless materials using FDTD simulations. However, the analytical solution can easily be used to examine the law of conservation of power. Let us consider the vertical rebar wall of case B but using conductivity of  $\sigma = 0$ . All the propagating Bragg modes of the transmission and reflection coefficients at normal incident angle are plotted in Fig. 7.14 (a) and (b). In Fig. 7.14 (c), the amount of power which is carried by the zeroth order mode is compared with that carried by all the propagating modes. As shown, the power carried by all the propagating modes is exactly 1. The law of conservation of power is examined for different incidence angles, both for the rebar and crossed rebar concrete walls and it is observed that the results based on the approximate analytical solution verify this law.

## 7.5 Conclusions

The problem of EM scattering from reinforced concrete walls is considered and an approximate analytical solution is obtained. This is accomplished by invoking the thin wire approximation and assuming only axial induced currents on the metallic rebars, embedded in the concrete. This in conjunction with closed-form expressions for the Green's function of the problem leads to an analytical solution for the reflection and transmission coefficient of all Bragg modes of an arbitrary incident plane wave. The Green's function of the 2-D periodic structure of crossed rebar embedded in a concrete layer is approximated by the superposition of Green's function of two orthogonal 1-D periodic structures and a procedure similar to the vertical rebar structure is followed to arrive at a simple solution. For this problem, mixed modes of the 2-D periodic structure are ignored. This approximation is shown to be valid for thin orthogonal wires. Simulation results are verified using an independent formulation based on FDTD. Using the proposed approximate analytical formulations, the sensitivity of transmission and reflection coefficients to the wall parameters such as relative dielectric constant and conductivity of the concrete, metal thickness, and periodicity of metallic rods and frequency and polarization of incident field is easily possible.

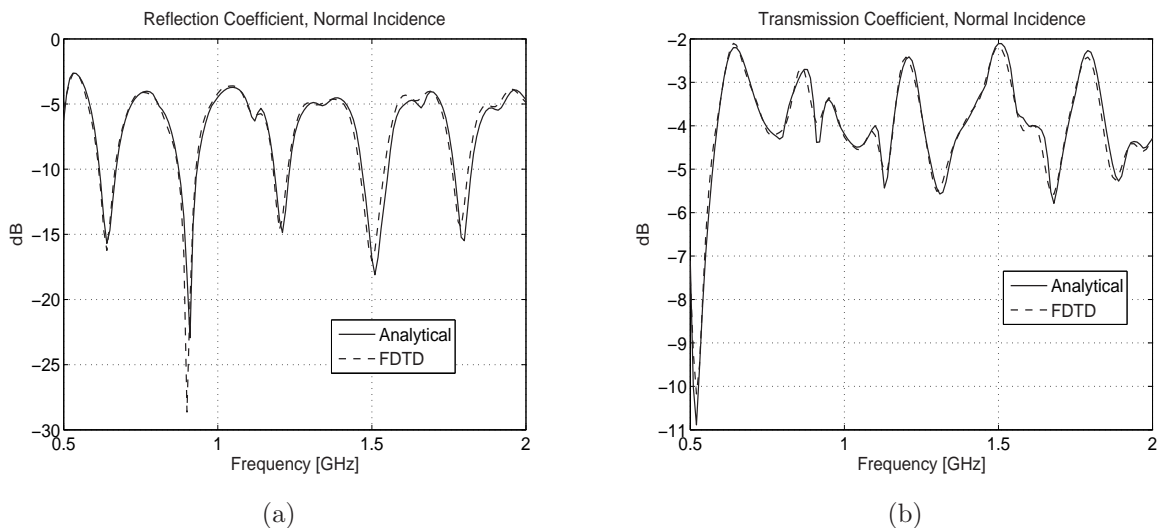
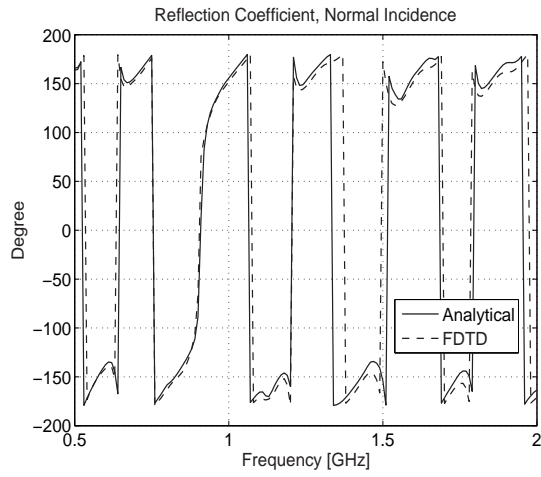
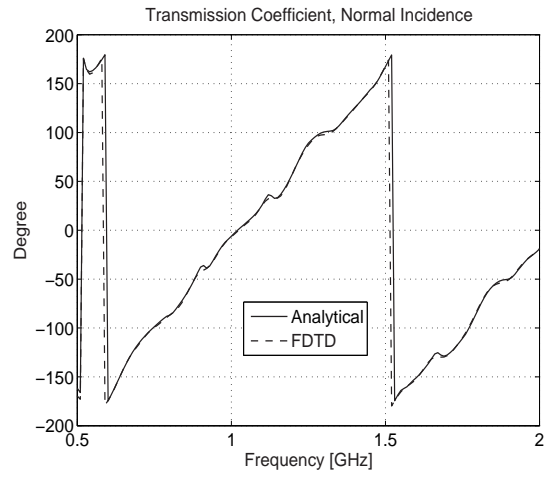


Figure 7.5: (a) Magnitude of co-polarized reflection coefficient and (b) transmission coefficient of the vertical rebar concrete wall of case A at normal incidence for horizontal polarization of incident field (wall thickness = 20.4 cm, metal thickness = 1.2 cm).

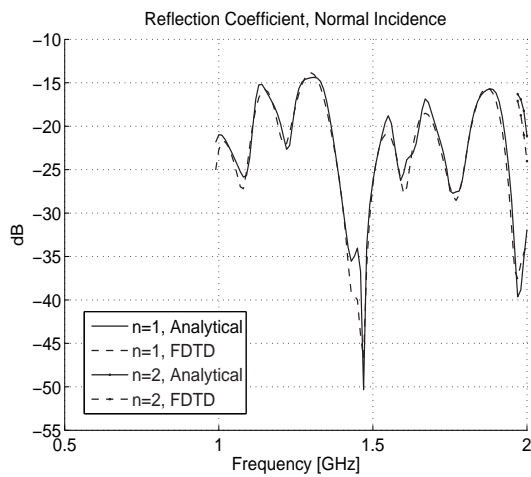


(a)

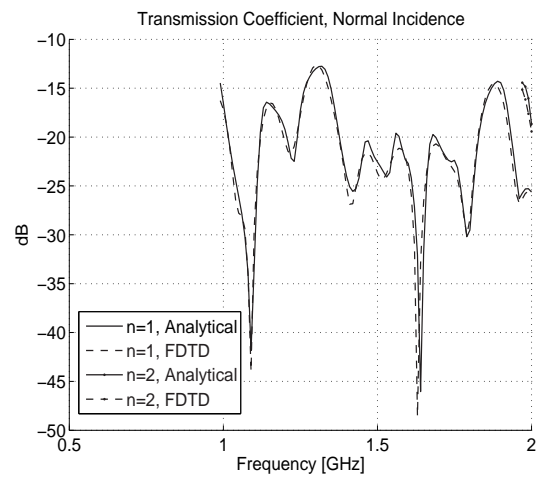


(b)

Figure 7.6: (a) Phase of co-polarized reflection coefficient and (b) transmission coefficient of the vertical rebar concrete wall of case A at normal incidence for horizontal polarization of incident field.

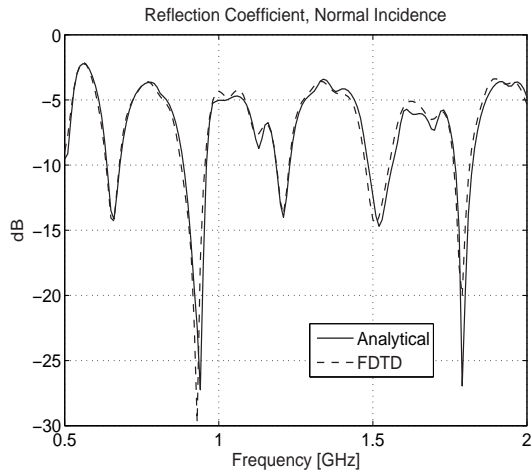


(a)

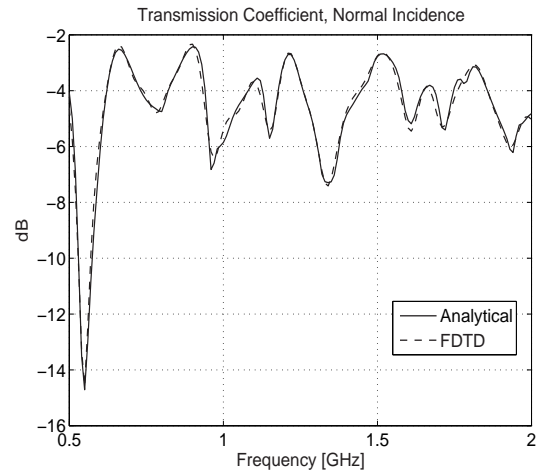


(b)

Figure 7.7: Co-polarized (a) reflected and (b) transmitted Bragg modes of the vertical rebar concrete wall of case A at normal incidence due to a horizontal (TE) polarization of incident field.

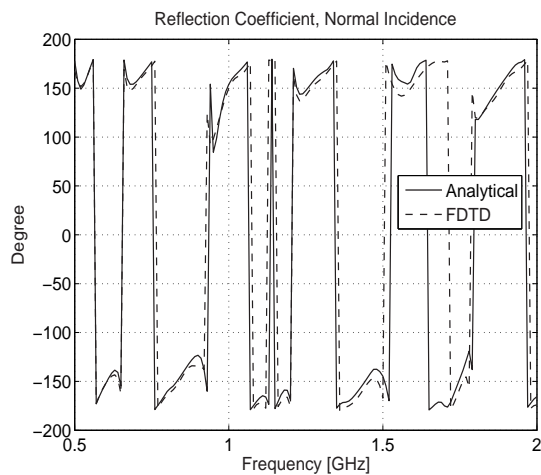


(a)

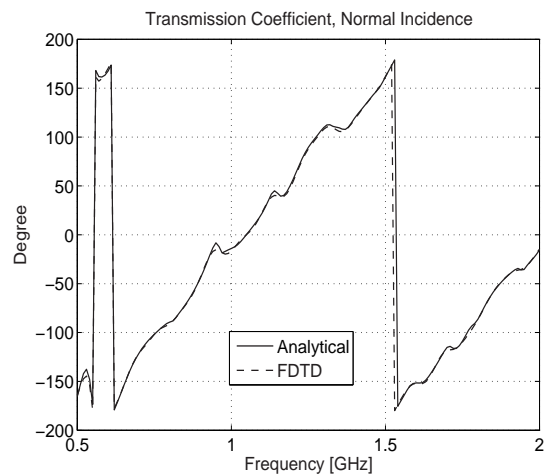


(b)

Figure 7.8: (a) Magnitude of co-polarized reflection coefficient and (b) transmission coefficient of the vertical rebar concrete wall of case B at normal incidence angle for horizontal polarization of incident field (wall thickness = 20.4 cm, metal thickness = 2.4 cm).



(a)



(b)

Figure 7.9: (a) Phase of co-polarized reflection coefficient and (b) transmission coefficient of the vertical rebar concrete wall of case B at normal incidence angle for horizontal polarization of incident field.

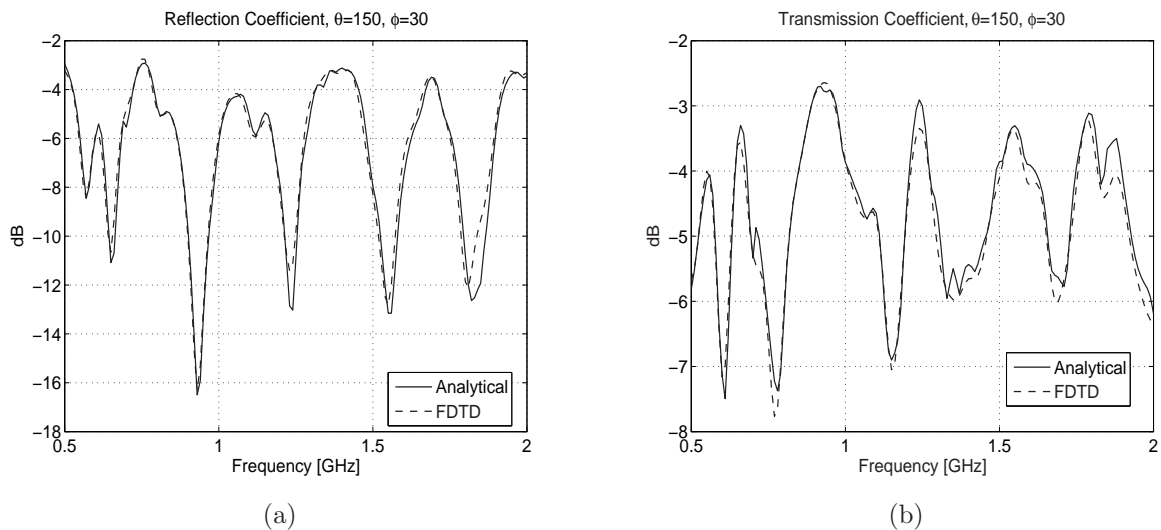


Figure 7.10: (a) Magnitude of co-polarized reflection coefficient, and (b) transmission coefficient of the vertical rebar concrete wall of case B at oblique incidence angle ( $\theta=150$ ,  $\phi=30$ ) for horizontal polarization of incident field.

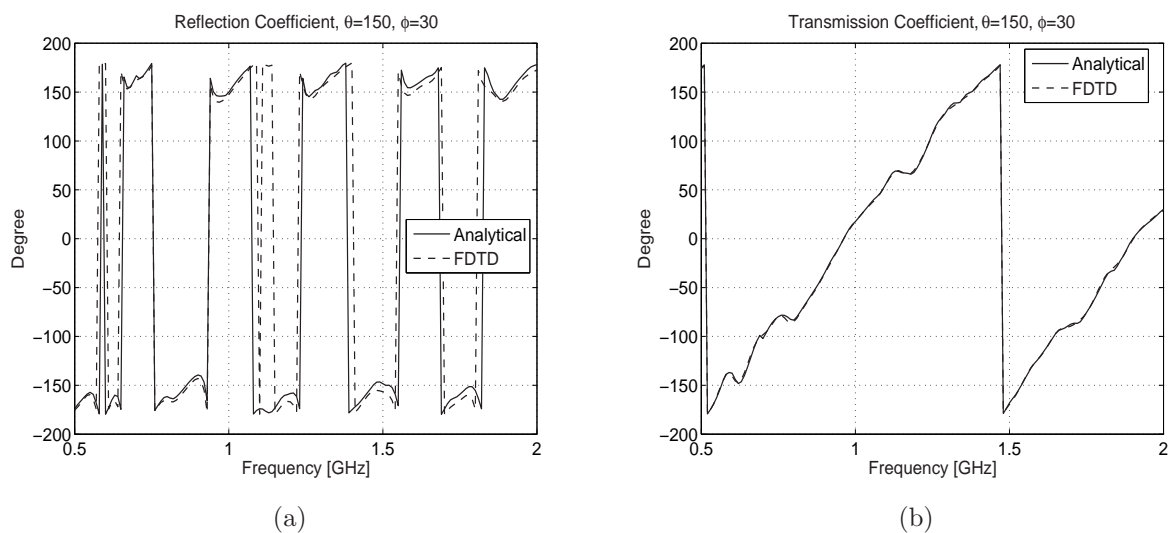


Figure 7.11: (a) Phase of co-polarized reflection coefficient and (b) transmission coefficient of the vertical rebar concrete wall of case B at oblique incidence angle ( $\theta=150$ ,  $\phi=30$ ) for horizontal polarization of incident field.

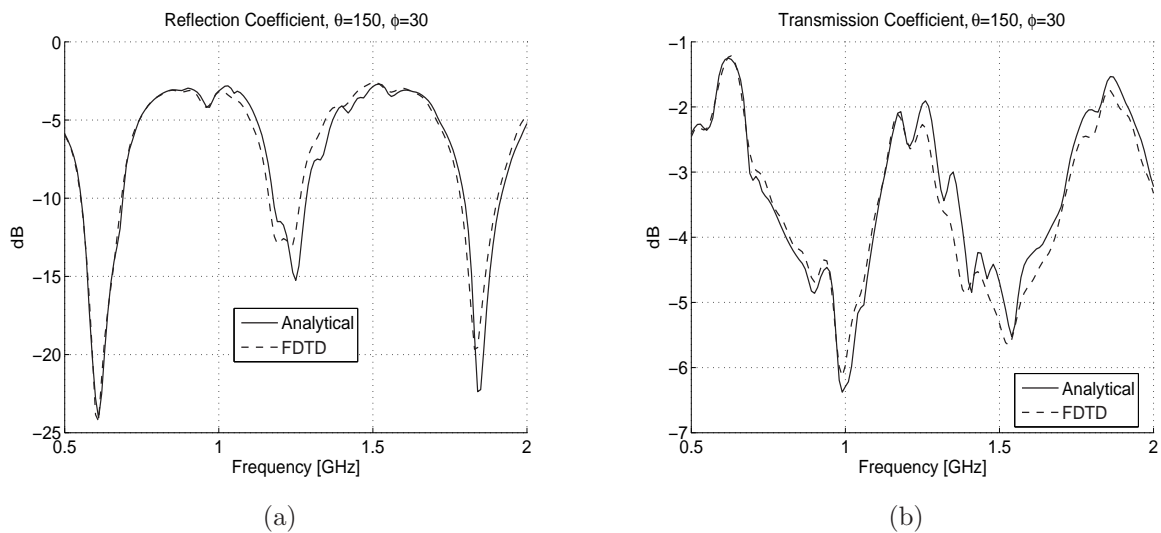


Figure 7.12: (a) Magnitude of co-polarized reflection coefficient and (b) transmission coefficient of the crossed rebar concrete wall at oblique incidence angle ( $\theta=150, \phi=30$ ) for horizontal (TE) polarization of incident field.

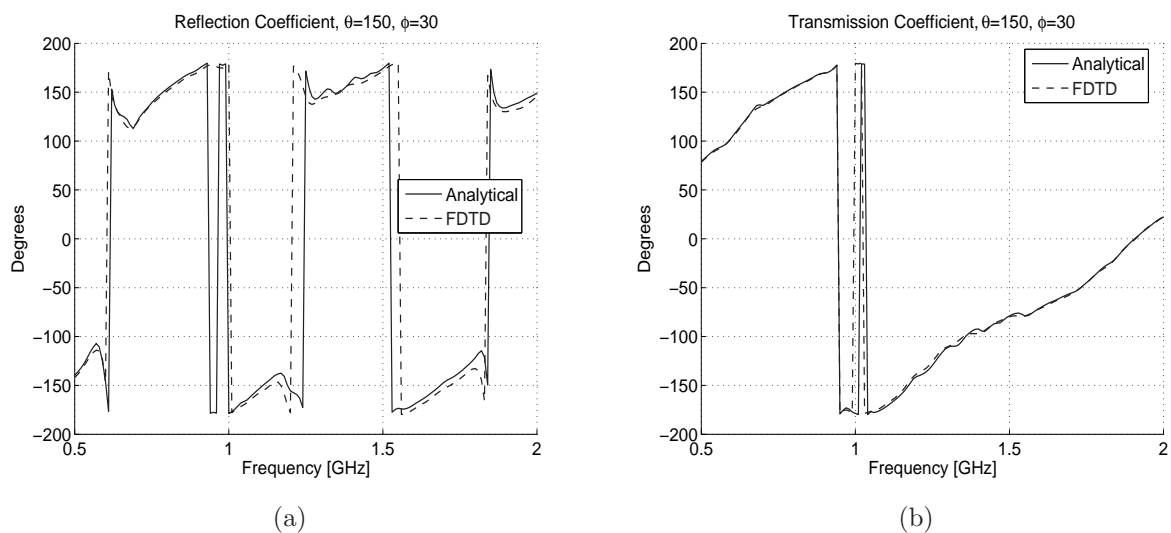


Figure 7.13: (a) Phase of reflection coefficient and (b) transmission coefficient of the crossed rebar concrete wall at oblique incidence angle ( $\theta=150, \phi=30$ ) for horizontal (TE) polarization of incident field.

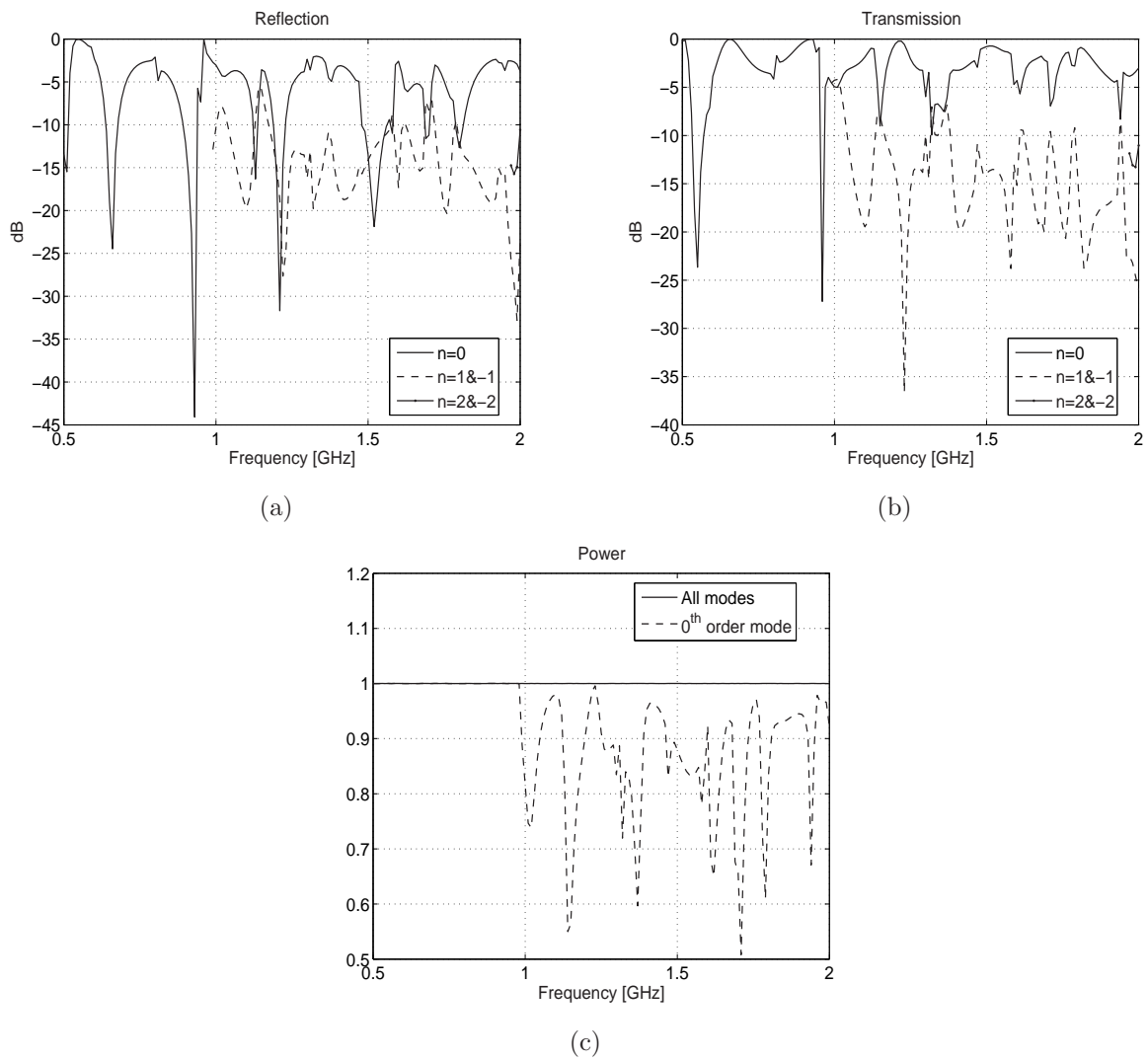


Figure 7.14: (a) Magnitude of co-polarized reflected and (b) transmitted Bragg mode scattered fields from a lossless vertical rebar concrete wall with metal thickness = 2.4 cm at normal incidence for horizontal (TE) polarization of incident field. (c) Power carried by the zeroth order mode is compared with the total power.

## CHAPTER 8

### Conclusions and Recommendations for Future Work

#### 8.1 Summary

The main objective of this thesis is providing applicable solutions to problems of electromagnetic scattering from targets that are embedded inside complex environments such as forest canopies and building structures. Since these problems require a significantly large computational domain if they are solved by full-wave numerical techniques, the scattering domains are divided into parts and hybrid methods are proposed. The challenges due to constructing such methods are 1) the development of physics-based wave penetration models for the environments and 2) computation of the scattering from the embedded targets, illuminated by myriads of the environment's constituent scatterers. In these thesis, hybrid solutions composed of numerical and analytical techniques are proposed that are computationally efficient and in practical interest.

Important applications of the proposed methods are in the area of remote sensing and wireless communications. In the area of remote sensing, first phenomenological studies are required to characterize the environment scatterers' effects on an intrinsic backscattering response of an embedded target and second a polarization analysis is needed to enhance the ability of radars in detection and identification of the target. On the other hand, in the area of wireless communication accurate channel characterization of such urban and indoor environments is of interest in both analyzing and designing the communication systems. This thesis is organized to address the above mentioned areas.

## 8.2 Contributions

The contributions are given in the following subsections.

### 8.2.1 Development of a comprehensive physics-based model for computation of scattering from complex targets camouflaged inside forest canopies

The problem of scattering from camouflaged targets was solved by dividing the problem into three parts: 1) modeling of propagation through and scattering from the forest, and 2) calculation of scattering from the hard targets, illuminated by an arbitrary field, and 3) computation of scattering interaction between the hard target and foliage around it.

The first part of the problem was solved by employing a single scattering foliage model, developed in the past. This is a coherent model that preserves the geometry of tree structures using a statistical Lindermyer system. Tree constituents are modeled by dielectric cylinders and disks whose scatterings are analytically derived using high- and low-frequency techniques which are valid in both the near-field and far-field regions of the foliage scatterers. The scattered field from all tree components and the attenuated incident field were used as the excitation for the hard target. The second part, computation of the scattered field from an isolated target, is solved using exact or approximate numerical methods. For relatively low frequencies, the FDTD technique is used to compute the scattered field from the hard target. For higher frequencies on the other hand the IPO approximation is employed. The connection between these two models, that accounts for the first order interaction between the foliage scatterers and the target and vice versa, is accomplished through the application of the reciprocity theorem.

Simulations of scattering from vehicles used as hard targets embedded inside a pine forest canopy, in VHF frequency band (20-200 MHz) and at 2 GHz (i.e. L-band), was carried out using proposed hybrid models. Based on simulation results, the significance of the scattering from tree components on the target response at the microwave frequencies was clearly indicated.

## 8.2.2 Polarization Discrimination for Improving Foliage-Camouflaged Target Detection

Many realizations of foliage around a hard target were obtained using the coherent scattering model in a Monte Carlo simulation. These realizations provide the statistical variations of foliage and target response. Based on fully polarimetric simulation results of a foliage camouflaged metallic target a polarization synthesis optimization method for improving signal to clutter was examined. A genetic algorithm was implemented for finding an optimal set of radar transmit and receive polarizations that maximizes target backscatter to clutter backscatter ratio.

## 8.2.3 Phenomenological Study of Through-Wall Imaging, Forward and Inverse Models

To detect and identify targets behind building walls SAR technique was used by employing ultra-wideband antennas and measured for wide incidence angles. In order to solve the forward model, walls are categorized into two groups: 1) homogeneous walls such as poured concrete, brick, and adobe walls and 2) inhomogeneous walls including drywalls, cinder block and reinforced concrete walls.

The Ray-tracing method was used for estimation of the transmissivity and reflectivity of the homogenous walls. This approach was validated by measuring the transmission and reflection coefficients of a poured concrete wall built inside the laboratory. The inhomogeneous walls on the other hand are analyzed differently. They are modeled by 1-D or 2-D periodic structures. Exact numerical or approximate analytical techniques were employed to simulate the scattering properties. At relatively low frequencies, the effective medium theory was used and accurate solutions to the problems were obtained. At higher frequencies where Bragg mode transmission and reflection coefficients are excited full-wave analysis are needed. The scattering from cinder block walls was computed using a hybrid ray-optics approximation and FDTD method and the scattering from reinforced concrete walls was calculated employing an approximate analytic approach.

Once the transmissivity and reflectivity of the walls were computed the simulation of through wall imaging was carried out. It was shown that the SAR image of a point target behind a homogenous wall can be significantly defocused. That is the cross-range resolution is significantly degraded and the target is imaged at different range from its actual position. Also, for the case where the point target is behind an inhomogeneous cinder block wall, it was shown that instead of one focused point, multiple points are generated along the range.

Refocusing techniques based on the idea of match filtering were proposed to remove the wall transmissivity effects and reconstruct the ideal point spread functions. To verify the methods, a controlled experiment using an ultra-wideband system operating over frequency band of 1-3 GHz within the laboratory environment was performed. Employing the experimental data, highly distorted images of two point targets in close proximity of each other behind a wall were resolved after refocusing. In addition, a dual-frequency synthetic method was presented to improve the cross-range resolution of the refocused images.

#### **8.2.4 Development of An Approximate Solution of Scattering from Reinforced Concrete Walls Using An Analytic 1-D Periodic Green's Function**

The problem of EM scattering from reinforced concrete walls was considered and accurate approximate analytical solutions were obtained, assuming the thin wire approximation. The closed-form expression of a 1-D periodic Green's function when the sources are inside a dielectric slab was derived first. Next, the induced currents on the metallic rebars were assumed axial and using the 1-D analytical periodic Green's functions the reflection and transmission coefficient of all Bragg modes of an arbitrary incident plane wave were computed. The Green's function of the 2-D periodic structure of crossed rebar concrete walls was approximated by the superposition of Green's function of two orthogonal 1-D periodic structures. This approximation was shown to be valid for thin orthogonal wires. Simulation results were verified using an independent formulation based on the FDTD technique.

## 8.3 Future Work

Possible research programs that can be investigated in conjunction with the material presented in this thesis are many. The following subsections address the most relevant areas.

### 8.3.1 Future researches on the EM scattering from foliage camouflaged targets

1) One of the researches pertained to the EM scattering from the foliage camouflaged targets is on performance analysis and comparison between the measured and the simulated data using the developed models. In fact, performing an actual experiment for validation of the deterministic formulation had been beyond the realm of our capability for the following reasons: 1) characterization of foliage (geometry, size, orientation, location, dielectric properties, etc.) of many trees around a target to within a fraction of wavelength is a monumental task. Same is true for positioning a well-characterized hard target in foliage. 2) Radars have to be on the far-field of the region occupied by the trees interacting with the target. For a proper validation a wideband radar in the far-field illuminating the scene at multiple incidence angles is needed .

However, provided the radars and measurement systems the statistical behavior of the backscattering from camouflaged targets can be analyzed and compared with the simulated results. To provide the simulated data, backscattering from targets for different incidence angles and frequency points must be computed. For efficient computation, methods in the parallel computing are needed.

2) The other future research program is investigation of applicability of novel detection and identification algorithms such as polarimetry and angular correlation function (ACF). In chapter 4, using GA an optimum polarization set for discrimination of a foliage camouflaged hard target is found for which the ratio of the RCS of the target to that of the clutter is maximized. It is of interest to see the performance of using the optimum polarization sets, using the measured data. Also application of other detection methods such as ACF can be examined. Since, the foliage is a random environment, its angular correlation function is very small away from the memory line. Therefore, it is expected that the ratio of the ACF of

scattered fields from a target inside the foliage is significantly larger than that of the foliage alone. Simulation results have shown that using ACF the target can be effectively detected. However, measurement data is needed for confirmation.

### 8.3.2 Future researches on the through-wall imaging

1) In this thesis, EM models for propagation through different walls, such as poured and reinforced concrete walls are studied and validated by either measurement or full-wave numerical methods. However, the scattering from cinder block walls have not been examined by measurement. It is of interest that the simulated data is validated by measurement. That is image of point targets behind cinder block walls are obtained using measured data first and next the images are refocused using the simulated reflectivity and transmissivity.

2) Investigation of polarization signatures of hidden targets and study on the possible techniques to detect hidden targets using radar polarimetry is a future research topic that needs further investigation. In other words, polarimetric simulations of different kinds of walls must be investigated for two main reasons 1) study of impact of walls on images of point targets illuminated by different polarization of incident fields to find optimum polarization(s) that has less effect on the target image and/or gives higher level of signal to noise ratio and 2) investigation of the applicability of polarization synthesis in identification of targets behind walls.

3) In chapter 5, it was shown that the effect of direct reflection from the concrete walls in the detection of targets behind the walls is significant. To reduce the effect of the walls, the time-domain signal was processed and the reflection from the walls were analytically computed and subtracted from the total received signals. To have further improvement, it is of interest to suppress the reflection using proper measurement setup. This can be accomplished for example by using the interferometric signals.

Let us suppose the measurement set up is consist of three antennas located along  $z$ , all receivers and one (i.e. the one in the middle) transmitter. A difference signal is computed by subtracting the signal of lower receiver from that of the upper receiver. Because of the symmetry in the problem, the contribution of the reflection from the wall in the difference

signal is suppressed. Primary studies are accomplished by using simulated data and excellent signal to clutter ratio was obtained. Furthermore, the setup can be extended and more than three antennas can be used in order to enhance the resolution along the height,  $z$  direction. That is the received signals of pair antennas symmetrically positioned with respect to the transmitting antennas are used to compute multiple difference signals.

4) While through-wall imaging was investigated using synthetic aperture method, a thorough examination on application of real apertures is needed. A real aperture radar has a narrow antenna beam. Therefore, using a real aperture radar the multi-path and clutter effects are significantly reduced in the target imaging. As mentioned in chapter 5, since the attenuation through poured concrete walls is significantly high at high frequencies, in order to have enough signal to noise ratio operation at low microwave frequencies (i.e. 1-2.5 GHz) is desired. This requires an antenna with extensively large aperture size, not in practical use. However, for walls that does not have significantly high attenuation at high frequencies such as drywalls the frequency of operation can be significantly increased and therefore the size of the antenna aperture can be extremely reduced.

## APPENDIX

## APPENDIX A

### Derivation of Transverse Fields' Components

Electric and magnetic field  $\hat{x}$ -directed components for all 3 regions are computed using (7.3), (7.8), and (7.9). For region II we have

$$\begin{aligned}
 E_x^{II} &= \frac{i}{k_1^2 - k_{yi}^2} \\
 &\sum_{n=-\infty}^{+\infty} \left[ \frac{ik_{nx}k_{yi}}{k_{1nz}} e^{ik_{nx}(x-x')} (\tilde{I}_y e^{ik_{1nz}|z-z'|} + \right. \\
 &\qquad\qquad\qquad A_n e^{ik_{1nz}z} + B_n e^{-ik_{1nz}z}) \\
 &\qquad\qquad\qquad \left. - ik_1 Z_1 e^{ik_{nx}(x-x')} (A'_n e^{ik_{1nz}z} - B'_n e^{-ik_{1nz}z}) \right] \\
 H_x^{II} &= \frac{i}{k_1^2 - k_{yi}^2} \\
 &\sum_{n=-\infty}^{+\infty} \left\{ \frac{ik_{nx}k_{yi}}{k_{1nz}} e^{ik_{nx}(x-x')} (A'_n e^{ik_{1nz}z} + B'_n e^{-ik_{1nz}z}) \right. \\
 &\qquad\qquad\qquad \left. + ik_1 Y_1 e^{ik_{nx}(x-x')} [\tilde{I}_y \operatorname{sgn}(z - z') e^{ik_{1nz}|z-z'|} + \right. \\
 &\qquad\qquad\qquad \left. A_n e^{ik_{1nz}z} - B_n e^{-ik_{1nz}z}] \right\} \tag{A.1}
 \end{aligned}$$

and for region I and III we have,

$$\begin{aligned}
E_x^I &= \frac{i}{k_0^2 - k_{yi}^2} \sum_{n=-\infty}^{+\infty} \left( \frac{ik_{nx}k_{yi}}{k_{nz}} \tilde{I}_y C_n e^{ik_{nx}(x-x')} e^{ik_{nz}(z-z')} \right. \\
&\quad \left. - ik_0 Z_0 D_n e^{ik_{nx}(x-x')} e^{ik_{nz}z} \right) \\
H_x^I &= \frac{i}{k_0^2 - k_{yi}^2} \sum_{n=-\infty}^{+\infty} \left( \frac{ik_{nx}k_{yi}}{k_{nz}} D_n e^{ik_{nx}(x-x')} e^{ik_{nz}z} \right. \\
&\quad \left. + ik_0 Y_0 \tilde{I}_y C_n e^{ik_{nx}(x-x')} e^{ik_{nz}(z-z')} \right) \\
E_x^{III} &= \frac{i}{k_0^2 - k_{yi}^2} \sum_{n=-\infty}^{+\infty} \left( \frac{ik_{nx}k_{yi}}{k_{nz}} \tilde{I}_y E_n e^{ik_{nx}(x-x')} e^{-ik_{nz}(z-z')} \right. \\
&\quad \left. + ik_0 Z_0 F_n e^{ik_{nx}(x-x')} e^{-ik_{nz}z} \right) \\
H_x^{III} &= \frac{i}{k_0^2 - k_{yi}^2} \sum_{n=-\infty}^{+\infty} \left( \frac{ik_{nx}k_{yi}}{k_{nz}} F_n e^{ik_{nx}(x-x')} e^{-ik_{nz}z} \right. \\
&\quad \left. - ik_0 Y_0 \tilde{I}_y E_n e^{ik_{nx}(x-x')} e^{-ik_{nz}(z-z')} \right). \tag{A.2}
\end{aligned}$$

The  $\hat{z}$ -directed component of electric field in region I and III is respectively

$$\begin{aligned}
E_z^I &= \frac{i}{k_0^2 - k_{yi}^2} \left( \sum_{n=-\infty}^{+\infty} ik_{yi} \tilde{I}_y C_n e^{ik_{nx}(x-x')} e^{ik_{nz}(z-z')} \right. \\
&\quad \left. + ik_0 Z_0 D_n \frac{k_{nx}}{k_{nz}} e^{ik_{nx}(x-x')} e^{ik_{nz}z} \right) \\
E_z^{III} &= \frac{i}{k_0^2 - k_{yi}^2} \left( \sum_{n=-\infty}^{+\infty} -ik_{yi} \tilde{I}_y E_n e^{ik_{nx}(x-x')} e^{-ik_{nz}(z-z')} \right. \\
&\quad \left. + ik_0 Z_0 F_n \frac{k_{nx}}{k_{nz}} e^{ik_{nx}(x-x')} e^{-ik_{nz}z} \right). \tag{A.3}
\end{aligned}$$

## BIBLIOGRAPHY

- [1] L. Carin, N. Geng, M. McClure, J. Sichina, and L. Nguyen, *Ultra-wideband synthetic-aperture radar for mine-field detection*, IEEE Antennas Propag. Mag., Vol. 41, No. 1, pp: 1833, Feb. 1999.
- [2] D.A. Hill, *Electromagnetic scattering by buried objects of low contrast*, IEEE Trans. on Geoscience and Remote Sensing, Vol. 26, No. 2, pp 195-203, March 1988.
- [3] B. T. Binder, M. F. Toups, S. Ayasli, and E. M. Adams, *SAR foliage penetration phenomenology of tropical rain forest and northern U.S. forest*, in Proc. IEEE Int. Radar Conf., May 811, pp: 158163, 1995.
- [4] B. Ferrell, *Ultrawideband foliage penetration measurements*, in Proc. IEEE National Radar Conf., pp: 8084, Mar. 1994, .
- [5] L.M. Frazier, *Surveillance through walls and other opaque materials*, Proc. SPIE Vol. 2497, pp. 115-119, 1995.
- [6] K. Sarabandi,  *$\Delta k$ -radar equivalent of interferometric SAR's: a theoretical study for determination of vegetation height* IEEE Trans. on Geoscience and Remote Sensing, Vol. 35, No. 5, pp: 1267 - 1276 Sept. 1997.
- [7] Ishimaru, A.; Tsz-King Chan; Kuga, Y., *An imaging technique using confocal circular synthetic aperture radar* IEEE Trans on Geoscience and Remote Sensing, Vol. 36, No. 5, Part 1, pp:1524 - 1530 Sept. 1998.
- [8] (2007) Canada Center for Remote Sensing website. [Online]. Available: [http://www.ccrs.nrcan.gc.ca/resource/tutor/polarim/index\\_e.php](http://www.ccrs.nrcan.gc.ca/resource/tutor/polarim/index_e.php)
- [9] S.R. Cloude and E. Pottier, *A review of target decomposition theorems in radar polarimetry*, IEEE Trans. on Geoscience and Remote Sensing, Vol. 34, No. 2, pp:498 - 518, March 1996.
- [10] Mehrdad Soumekh, *Synthetic Aperture Radar Signal Processing with Matlab Algorithms*, John Wiley & Sons, New York 1999.
- [11] (2006) The Sandia National Laboratory website. [Online]. Available: <http://www.sandia.gov/radar/sar.html>
- [12] G. A. Ioannidis and D. E. Hammers, *Optimum antenna polarizations for target discrimination in clutter* , IEEE Trans. Antennas and Propagation. , Vol. 27, No. 3, May 1979.
- [13] Zhang G., Tsang L., *Application of angular correlation function of clutter scattering and correlation imaging in target detection*, IEEE Trans. on Geoscience and remote sensing, Vol. 36, No. 5, September 98.
- [14] Tsz-King Chan, Kuga Y., Ishimaru A., *Experimental studies on circular SAR imaging in clutter using angular correlation function technique*, IEEE Trans. Geoscience and Remote Sensing, Vol. 37, No. 5, Sept. 1999.

- [15] Leung Tsang, Jin Au Kong, and R.T. Shin, *Theory of Microwave Remote Sensing*, Wiley series in Remote Sensing, John Wiley and Sons, NY, 1985.
- [16] Karam, M.A., Fung A.K., Lang R.H., Chauhan N.S., *A microwave scattering model for layered vegetation*, IEEE Trans. on Geoscience and Remote Sensing, Vol. 30, No. 4, July 1992.
- [17] Ulaby F. T., Sarabandi K., McDonald K., Whitt M., and Dobson M. C., *Michigan microwave canopy scattering model (MIMICS)*, The University of Michigan, Ann Arbor, Michigan, Tech. Rep. 022486-T-1, July 1988.
- [18] Yi-Cheng Lin and Kamal Sarabandi, *A Monte Carlo Coherent Scattering Model For Forest Canopies Using Fractal-Generated Trees*, IEEE Trans. Geosci. Remote Sensing, vol. 37, pp. 440-451, Jan. 1999.
- [19] Il-Suek Koh, and Kamal Sarabandi, *Polarimetric Channel Characterization of Foliage for Performance Assessment of GPS Receivers Under Tree Canopies*, IEEE Trans. Antennas Propagat., Vol. 50, No. 5, May 2002.
- [20] Nashashibi, A.Y., Ulaby, F.T., *foliage-obscured targets by polarimetric millimeter-wave Radar*, IEEE Trans. Geoscience and Remote Sensing, Vol. 43, No. 1, Jan. 2005.
- [21] Fleischman J.G., Ayasli S., Adams E.M., Gosselin D.R., *Foliage attenuation and backscatter analysis of SAR imagery*, IEEE Trans. on Aerospace and Electronic Systems, Vol. 32, No. 1, Jan. 1996.
- [22] C. D. Moss, F. L. Teixeira, Y. Eric Yang, and Jin Au Kong, *Finite-Difference Time-Domain Simulation of Scattering From Objects in Continuous Random Media*. IEEE Trans. Geoscience and Remote Sensing, Vol. 40, No. 1, Jan. 2002.
- [23] Hans Israelsson, Lars M. H. Ulander, Torleif Martin, and Jan I. H. Askne, *A Coherent Scattering Model to Determine Forest Backscattering in VHF-Band*, IEEE Trans. Geosci. and Remote Sensing, Vol. 38, No. 1, Jan. 2000.
- [24] Sarabandi, K., P.F. Polatin, *Electromagnetic Scattering From Two Adjacent Objects*, presented at PIERS'93, Pasadena, July 1993.
- [25] Kenneth Demarest, Zhubo Huang, and Richard Plumb, *An FDTD Near- to Far-Zone Transformation for Scatterers Buried in Stratified Ground* IEEE Trans. Antennas Propagat., Vol. 44, No. 8, Aug. 1996.
- [26] L.L. Foldy, *The multiple-scattering of Waves*, Phys. Rev., Vol. 67, pp:107-119, 1945.
- [27] Michael Kaye, P. Krishna Murthy, and Gary A. Thiele, *An Iterative Method for Solving Scattering Problems*, IEEE Trans. Antennas and Propagation. , Vol. 33, No. 11, Nov. 1985.
- [28] P. Krishna Murthy, K. C. Hill, and Gary A. Thiele, *A Hybrid-Iterative Method for scattering Problems*, IEEE Trans. Antennas and Propagation. , Vol. 34, No. 10, Oct. 1986. F.

- [29] Timothy Griesser, and C. A. Balanis, *Backscatter Analysis of Dihedral Corner Reflectors Using Physical Optics and Physical Theory of Diffraction*, IEEE Trans. Antennas and Propagation. , Vol. 35, No. 10, Oct. 1987.
- [30] Obelleiro, J. L. Rodriguez and R. J. Burkholder, *An Iterative Physical Optics Approach for Analyzing the Electromagnetic Scattering by Large Open-Ended Cavities*, IEEE Trans. on Antennas and Propagation, Vol. 43, No. 4, pp. 356-361, April 1995.
- [31] M. Dehmollaian, and K. Sarabandi, *Electromagnetic Scattering from Foliage Camouflaged Complex Targets*, IEEE Trans. on Geoscience and Remote Sensing, Vol. 44, No. 10, Oct. 2006.
- [32] K. Sarabandi, M. Dehmollaian, and H. Mosallaei, *Hybrid FDTD and single-scattering theory for simulation of scattering from hard targets camouflaged under forest canopy*, IEEE Trans. on Geoscience and Remote Sensing, Vol. 44, No. 8, pp 2072 - 2082, Aug. 2006.
- [33] James Tatoian, Giorgio Franceschetti, Heinz Lackner, and George Gibbs, *Through-the-wall impulse SAR experiments*. presented in the IEEE International Symposium on Antennas and Propagation and USNC/URSI National Radio Science Meeting, Washington D.C., 3-8 July 2005.
- [34] Fauzia Ahmad, Moeness Amin, and Saleem A. Kassam, *Synthetic Aperture Beamformer for Imaging Through a Dielectric Wall*, IEEE Trans. on Aerospace and Electronic Systems, Vol. 41, No. 1, pp. 271-283, Jan. 2005.
- [35] O. Landron, M.J. Feuerstein, T.S. Rappaport, *A comparison of theoretical and empirical reflection coefficients for typical exterior wall surfaces in a mobile radio environment*, IEEE Trans. on Antennas and Propagation, Vol. 44, No. 3, pp.341-351, March 1996.
- [36] Daniel Pena, Rodolfo Feick, Hristo D. Hristov, and Walter Grote, *Measurement and Modeling of Propagation Losses in Brick and Concrete Walls for the 900-MHz Band*, IEEE Trans. on Antennas and Propagation, Vol. 51, No. 1, pp:31-39, Jan. 2003.
- [37] Bernard De Backer, Henrik Borjeson, Daniel De Zutter, and Frank Olyslager, *Propagation Mechanisms for UHF Wave Transmission Through Walls and Windows*, IEEE Trans. on Vehicular Technology, Vol. 52, No. 5, pp:1297-1307, Sep. 2003.
- [38] Walter Honcharenko and Henry L. Bertoni, *Transmission and Reflection Characteristics at Concrete Block Walls in the UHF Bands Proposed for Future PCS*, IEEE Transaction on Antennas and Propagation, Vol. 42, No. 2, pp: 232-239, Feb. 1994
- [39] Ming Yang and Stavros Stavrou, *Rigorous Coupled-Wave Analysis of Radio Wave Propagation Through Periodic Building Structures*, IEEE Antennas and Wireless Propagation Letters, Vol. 3, pp:204-207, 2004.

- [40] Ying Wang, Safieddin Safavi-Naeini, and Sujeet K. Chaudhuri, *A Hybrid Technique Based on Combining Ray Tracing and FDTD Methods for Site-Specific Modeling of Indoor Radio Wave Propagation*, IEEE Trans. on Antennas and Propagation, Vol. 48, No. 5, pp:743-754, May 2000.
- [41] Ying Wang Sujeet K. Chaudhuri, and Safieddin Safavi-Naeini *An FDTD/Ray-Tracing Analysis Method for Wave Penetration Through Inhomogenous Walls*, IEEE Trans. on Antennas and Propagation, Vol. 50, No. 11, pp:1598-1604, Nov. 2002.
- [42] M. Dehmollaian and K. Sarabandi, *Hybrid FDTD and Ray Optics Approximation for Simulation of Through-Wall Microwave Imaging*, IEEE International Symposium on Antennas and Propagation July 9-14, 2006.
- [43] M. Dehmollaian and K. Sarabandi, *An Approximate Solution of Scattering from Reinforced Concrete Walls Using an Analytic 1-D Periodic Green's Function*, submitted to IEEE Trans. on Antennas and Propagation.
- [44] M. Dehmollaian and K. Sarabandi, *Refocusing through Building Walls, Using Synthetic Aperture Radar*, submitted to IEEE Trans. on Geoscience and Remote Sensing.
- [45] Imhoff M.L. , *A theoretical analysis of the effect of forest structure on SAR backscatter and the remote sensing of biomass*, IEEE Trans. on Geocience and Remote Sensing, Vol. 33, March 1995.
- [46] A. R. Von Hippel, *Dielectric materials and Applications*. New York, M.I.T. Press and Wiley, 1954.
- [47] Lawrence M. Frazier, *Radar Surveillance through Solid Materials*, proc. SPIE, Vol. 2938, pp. 139-146, Feb. 1997.
- [48] Nicholas C. Currie, David D. Ferris, Jr., Robert W. McMillan, and Michael C. Wicks, *New law enforcement applications of millimeter wave radar*, proc. on SPIE, Vol. 3066, pp. 2-10, June 1997.
- [49] David D. Ferris Jr. and Nicholas C. Currie, *Microwave and Millimeter-Wave Systems for Wall Penetration*, proc. SPIE, Vol. 3375, pp. 269-279, July. 1998.
- [50] David D. Ferris Jr. and Nicholas C. Currie, *A Survey of Current Technologies for Through-the-Wall Surveillance (TWS)*, proc. SPIE, Vol. 3577, pp. 62-72, Jan. 1999.
- [51] Genyuan Wang, Moeness Amin, and Yimin Zhang, *New Approach for Target Locations in the Presence of Wall Ambiguities*, IEEE Trans. on Aerospace and Electronic Systems, Vol. 42, No. 1, pp. 301-315, Jan. 2006.
- [52] Ulander Lars M., Froelind Per-Olov, Gustavsson Anders, Hellsten Hans, and Larsson Bjoern, *Detection of concealed ground targets in CARABAS SAR images using change detection*, Proceedings of Algorithms for Synthetic Aperture Radar Imagery VI, Orlando, FL, 5-9 April 1999, SPIE vol. 3721, pp. 243-252.

- [53] Ulander L.M.H., Blom M., Flood B., Follo P., Frolind P.-O., Gustavsson A., Jonsson T., Larsson B., Murdin D., Pettersson M., Raaf U., Stenstrom G., *Development of the ultra-wideband LORA SAR operating in the VHF/UHF-band*, Proceeding of IEEE International Geoscience and Remote Sensing 21-25 July 2003. Vol. 7, pp. 4268 - 4270.
- [54] Kamal Sarabandi, *Electromagnetic Scattering from Vegetation canopies*, Ph.D. dissertation, University of Michigan, Ann Arbor, MI, 1989.
- [55] Leung Tsang, Jin Au Kong, and Kung-Hau Ding, *Scattering of Electromagnetic Waves : Theories and Applications*, Wiely series in Remote Sensing, John Wiley and Sons, 2000.
- [56] Ling Li, Jiangqi He, Zhijun Liu, Dong X., and Carin L., *MLFMA analysis of scattering from multiple targets in the presence of a half-space*, IEEE Trans. on Antennas and propagation, Vol. 51, No. 4, April 2003.
- [57] Cloude S.R., Corr D.G., and Williams M.L., *Target detection beneath foliage using polarimetric synthetic aperture radar interferometry*, Waves Random Media, March 2004.
- [58] Dogaru, T.; Carin, L., *Time-domain sensing of targets buried under a rough air-ground interface*, IEEE Trans. on Antennas and Propagation, Vol. 46, No. 3, March 1998.
- [59] Yi-Cheng Lin, *A Fractal-Based Coherent Scattering and Propoagation Model for Forest Canopies*, Ph.D. dissertation, University of Michigan, Ann Arbor, MI, 1997.
- [60] Zimmermann M.H. and Brown C.L., *Tree Structures and Function*, Springer-Verlag, 1971.
- [61] Lindenmayer A., *Developmental Algorithms for Multicellular organisms: a survey of L-systems*, Journal of Theoretical Biology, Vol. 54, pp. 3-22, 1975.
- [62] Mandelbro B., *Fractal Geometry of Nature*, W. H. Freeman Company, 1983.
- [63] Prusinkiewicz P. and Lindenmayer A., *The Algorithmic Beauty of Plants*, Spring-Verla, 1990.
- [64] Sarabandi K. and Senior T.B.A, *Low-frequency scattering from cylindrical structures at oblique incidence*, IEEE Trans. on Geoscience and Remote Sensing, Vol. 28, No. 5, Sept. 1990.
- [65] A. Taflove, *Computational Electrodynamics: The Finite-Difference Time-Domain Method*, Artech House, MA, 1995.
- [66] A. Taflove, *Advances in Computational Electrodynamics: The Finite-Difference Time-Domain Method*, Artech House, MA, 1998.
- [67] H. Mosallaei and Y. Rahmat-Samii, *Broadband characterization of complex periodic EBG structures: An FDTD/Prony technique based on the split-field approach*, Electromag. J., vol. 23, no. 2, pp. 135-151, Feb.-Mar. 2003.

- [68] Sarabandi, K., and P.F. Polatin, *Electromagnetic Scattering from Two Adjacent Objects*, IEEE Trans. Antennas and Propagation, Vol. 42, No. 4, pp. 510-517, April 1994.
- [69] Roger F. Harrington, *Time-Harmonic Electromagnetic Fields*, John Wiley and Sons, NY, 2001.
- [70] Blejer D.J., Scarborough S.M., Frost C.E., Catalan H.R., McCoin K.H., Roman J., Mukai D.M., *Ultra-wideband polarimetric imaging of corner reflectors in foliage*, Proceeding of IEEE Antennas and Propagation, July 1992.
- [71] F.T.Ulaby, and C.Elachi, *Radar Polarimetry for Geoscience Applications*, Artech House, MA, 1990.
- [72] Nashashibi A.Y., Sarabandi K., Oveisgharan S., Dobson M.C., Walker W.S., Burke E., *Millimeter-wave measurements of foliage attenuation and ground reflectivity of tree stands at nadir incidence*, IEEE Trans. on Antennas and Propagation, Vol. 52, No. 5, May 2004.
- [73] R. J. Burkholder, *A Fast and Rapidly Convergent Iterative Physical Optics Algorithm for Computing the RCS of Open-Ended Cavities*, Applied Computational Electromagnetics Society Journal, Vol. 16, No. 1, pp. 53-60, March 2001.
- [74] Sarabandi K., and M. Park, *A radar cross-section model for power lines at millimeter-wave frequencies*, IEEE Transactions on Antennas and Propagation, Vol. 51, No.9, Sept. 2003.
- [75] Ulaby F.T., Whitt M.W., Dobson M.C., *Measuring the propagation properties of a forest canopy using a polarimetric scatterometer*, IEEE Trans. on Antennas and Propagation, Vol. 38, No. 2, Feb. 1990.
- [76] Mojtaba Dehmollaian and Kamal Sarabandi, *A Forward Scattering Model for Foliage Camouflaged Complex Targets*, Geoscience and Remote Sensing Symposium, 2004. IGARSS '04. Proceedings. 2004 IEEE International, 20-24 Sep 2004.
- [77] Kamal Sarabandi and Tsen-Chieh Chiu, *Optimum Corner Reflectors for Calibration of Imaging Radars*, IEEE Trans. Antennas and Propagation., Vol. 44, No. 10, Oct. 1996.
- [78] Casciato, M.D., and K. Sarabandi, *High Frequency Radio Wave Diffraction from Singly Curved Surfaces: A Heuristic Approach*, IEE Proceedings-Microwave, Antennas and Propagation, vol. 151, no. 1, Feb. 2004.
- [79] Adib Nashashibi, Kamal Sarabandi, and Fawwaz T. Ulaby, *A Calibration Technique for Polarimetric Coherent-on-Receive Radar System*, IEEE Trans. Antennas and Propagation., Vol. 43, No. 4, April 1995.
- [80] Anastassiou, H.T, *Radar cross section of a perfectly conducting, flat, polygonal plate over a dielectric, lossy half space: a closed form, physical optics expression*, International Conference on Mathematical Methods in Electromagnetic Theory, Vol.2, Page(s):505 - 507, Sept. 2002.

- [81] F. T. Ulaby and M. A. El-Rayes, *Microwave Dielectric Spectrum of Vegetation, Part II: Dual-dispersion Model*, IEEE Trans. Geosci. Remote Sensing, vol. GE-25, No. 5, Sep. 1987.
- [82] M.T.Hallikainen, F.T.Ulaby, M.C.Dobson, M.A.El-Rayes, and L.K.Wu, *Microwave Dielectric Behavior of Wet Soil, PartI: Emprical Models and Experimental Observations*, IEEE Trans. Geosci. Remote Sensing, vol. GE-23, Jan. 1985.
- [83] S. Kirkpatrick, C.D. Gelatt Jr., M.P. Vecchi, *Optimization by Simulated Annealing*, Sience, Vol. 220, May 1983.
- [84] Kamal Sarabandi, and Eric S. Li, *Characterization of Optimum Polarization for Multiple Target Discrimination Using Genetic Algorithms*, IEEE Trans. Antennas and Propagation. , Vol. 45, No. 12, December 1997.
- [85] Lin-Ping Song, Chun Yu, and Qing Huo Liu, *Through-wall imaging (TWI) by radar: 2-D tomographic results and analyses*, IEEE Trans. on Geoscience and Remote Sensing, Vol. 43, No. 12, pp. 2793 - 2798, Dec. 2005.
- [86] Francesco Soldovieri, Raffaele Solimene, Adriana Brancaccio, and Rocco Pierri, *Localization of the Interfaces of a Slab Hidden Behind a Wall*, IEEE Trans. on Geoscience and Remote Sensing, Vol. 45, No. 8, pp. 2471 - 2482, Aug. 2007.
- [87] G. Wang and M. Amin, *Imaging through unknown walls using different standoff distances*, IEEE Transactions on Signal Processing, Vol. 54, No. 10, pp. 4015-4025, Oct. 2006.
- [88] Jin Au Kong, *Electromagnetic Wave Theory*, EMW Publishing, Cambridge, Massachusetts, 2000.
- [89] A.H. Muqaibel, A.Safaai-Jazi, A. Bayram, A.M. Attiya and S.M. Riad, *Ultrawideband through-the-wall propagation*, IEE Proc.-Microw. Antennas Propag. Vol.152, No. 6, pp. 581-588, Dec. 2005.
- [90] D. Pena, R. Feick, H. D. Hristov and W. Grote, *Measurement and modeling of propagation losses in brick and concrete walls for the 900-MHz band*, IEEE Trans. on Antennas and Propagation, Vol. 51, No. 1, pp. 31-39, Jan. 2003.
- [91] Merrill I. Skolnik, *Introduction to Radar Systems*, Third Edition, New York, McGraw-Hill, 2001.
- [92] William C. Stone, *NIST Construction Automation Program Report No.3, Electromagnetic Signal Attenuation in Construction Materials*, Building and Fire Research Laboratory, National Institute of Standards and Technology, Gaithersburg, Maryland, Tech. Rep. NISTIR 6055, Oct. 1997.
- [93] F. J. Aurand, *Measurements of transient electromagnetic propagation through concrete and sand*, Sandia Nat. Labs., Livermore, CA, Sandia Rep. SAND96-2254 UC-706, Sept. 1996.

- [94] S. Laurens, J. P. Balayssac, J. Rhazi, G. Klysz, and G. Arliguie, *Non-destructive evaluation of concrete moisture by GPR: Experimental study and direct modeling*, Journal of Materials and Structures, Vol. 38, No. 9, pp. 827-832, Springer Netherlands, Nov. 2005.
- [95] A.H. Muqaibel and A.Safaai-Jazi, *A new formulation for characterization of materials based on measured insertion transfer function* IEEE Trans. on Microwave Theory and Techniques, Vol. 51, No. 8, pp. 1946-1951, Aug. 2003.
- [96] O. Buyukozturk, *Electromagnetic Properties of Concrete and Their Significance in Nondestructive Testing*, Transportation Research Record, No. 1574, pp. 10-17, 1997.
- [97] Jietao Zhang and Yi Huang, *Extraction of dielectric properties of building materials from free-space time-domain measurement*, High Frequency Postgraduate Student Colloquium, pp. 127 - 132, Sept. 1999.
- [98] D. M. Le Vine, R. Meneghini, R. H. Lang, and S . S. Seker, *High frequency scattering from arbitrarily oriented dielectric disks*, NASA TM-83910, June 1982 (available from NTIS No. 83N12306).
- [99] M.F. Iskander, Zhengqing Yun, *Propagation prediction models for wireless communication systems* , IEEE Trans. on Microwave Theory and Techniques, Vol. 50, No. 3, pp:662-673, March 2002.
- [100] R.A. Dalke, C.L. Holloway, P. McKenna, M. Johansson, A.S. Ali, *Effects of reinforced concrete structures on RF communications*, IEEE Trans. on Electromagnetic Compatibility, Vol. 42, No. 4, pp.486-496, Nov. 2000.
- [101] E. Richalot, M. Bonilla, Man-Fai Wong, V. Fouad-Hanna, H. Baudrand, and J. Wiart, *Electromagnetic propagation into reinforced-concrete walls*, IEEE Trans. on Microwave Theory and Techniques, Vol. 48, No. 3, pp. 357-366, March 2000.
- [102] Saverio Cristina and Antonio Orlandi, *An Equivalent Transmission Line Model for Electromagnetic Penetration through Reinforced Concrete Walls*, IEICE Trans. on Communications, Vol. E78-B, No. 2, pp. 218-229, Feb. 1995.
- [103] R. Mittra, C.H.Chan, and T.Cwik, *Techniques for Analyzing Frequency Selective Surfaces-A review*, Proc. IEEE, vol. 76, pp. 1593-1615, Dec. 1988.
- [104] Amir Aminian and Y. Rahmat-Samii, *Spectral FDTD: a novel technique for the analysis of oblique incident plane wave on periodic structures*, IEEE Trans on Antennas and Propagation, Vol. 54, No. 6, pp:1818-1825, June 2006.
- [105] J.R.Wait, *Theories of scattering from wire grids and mesh structures*, in Electromagnetic Scattering, Piergiorgio L. E. Uslenghi, New York, Academic Press, 1978, pp. 253-287.
- [106] Ben A. Munk, *Frequency Selective Surfaces, Theory and Design*, John Wiley and Sons, New York, NY, 2000.